SYNTHESIS AND PROPERTIES OF TELLURITE AND BISMUTHATE GLASSES CONTAINING TRANSITION METAL OXIDES

A thesis submitted for the degree of

DOCTOR OF PHILOSOPHY

by

SANDHYA RANI PELLURI

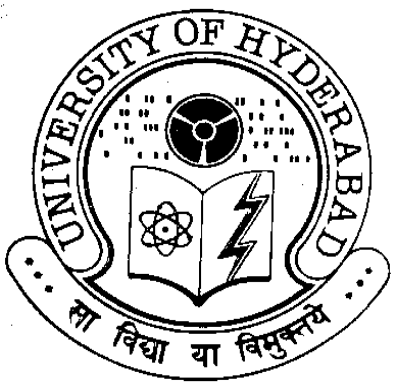

SCHOOL OF PHYSICS
UNIVERSITY OF HYDERABAD
HYDERABAD – 500046
INDIA

DECEMBER 2012

CONTENTS

Chapter 1

Introduction

One of the most frequently quoted definitions of the term "glass" is that proposed in 1945 by the American Society for Testing Materials: "Glass is an inorganic product of fusion which has cooled to a rigid condition without crystallising." This definition is satisfactory for those materials used to make windows, glass containers, camera lenses, glass ovenware, lamp envelopes, etc. This definition would exclude certain organic substances such as glucose or glycerol which can be supercooled to a rigid condition without crystallising and which in this form would possess many of the characteristics of glasses. Substances of quite diverse chemical composition have been obtained as glasses and it is becoming widely recognized that the property of glass-formation is not an atomic or molecular property but rather one of a state of aggregation.

Glasses are characterized by certain well-defined properties which are common to all of them and different from those of liquids and crystalline solids. X-ray and electron diffraction studies show that glasses lack long-range periodic order of the constituent atoms. That they resemble liquids and not crystalline solids in their atomic distribution is illustrated in Figure 1.1, in which the radial distribution function of a hypothetical material in the glassy state is compared with that of the gas, liquid and crystalline state of the same composition.

Unlike crystals, glasses do not have a sharp melting point and do not cleave in preferred directions. Like crystalline solids they show elasticity – a glass fibre can be bent almost double in the hand and, when released, springs back to its original shape: like liquids, they flow under a shear stress but only if it is very high. The glassy form of matter combines the 'short-time' rigidity characteristic of the crystalline state with a little of the 'long-time' fluidity of the liquid state. Glasses, like liquids, are isotropic, a property which is of immense value in their use for a variety of purposes.

A glass is generally obtained by cooling a liquid below its freezing point. The classical explanation for the formation of a glass is that, when a liquid is cooled, its fluidity (reciprocal viscosity) decreases and at a certain temperature below the freezing point, becomes nearly zero. Our liquid becomes 'rigid'.

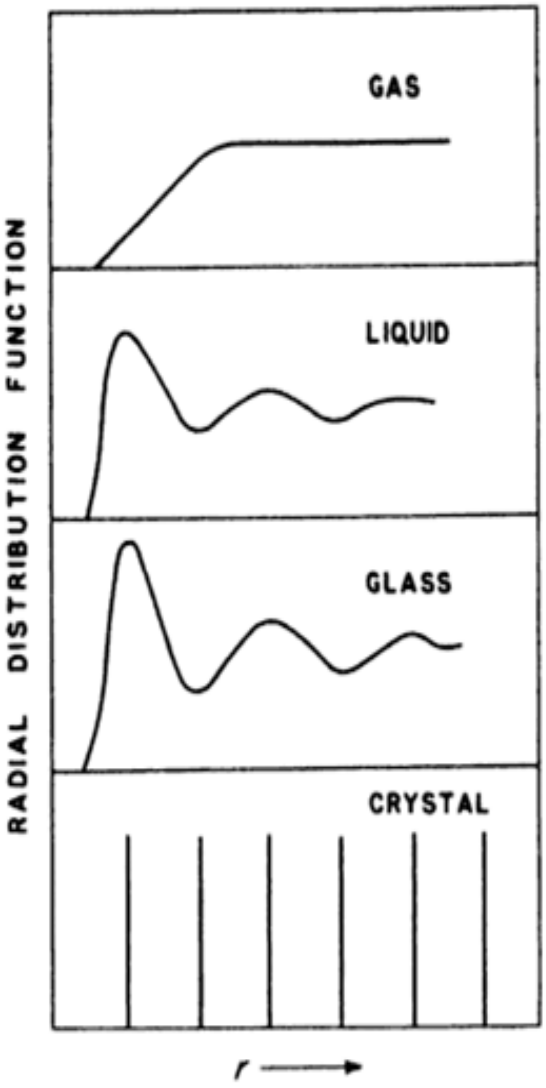

Fig 1.1 Comparison of the radial distribution function of a glass with that of the gaseous, liquid and crystalline states.

1.1 The glass transformation range:

The relation between crystal, liquid and glass can easily be explained by means of a volume-temperature diagram as shown in Figure 1.2. On cooling a liquid from the initial state A, the volume will decrease steadily along AB. If the rate of cooling is slow, and

nuclei are present, crystallization will take place at the freezing temperature T_f. The volume will decrease sharply from B to C; thereafter, the solid will contract with falling temperature along CD.

If the rate of cooling is sufficiently rapid, crystallization does not take place at T_f; the volume of the supercooled liquid decreases along BE, which is a smooth continuation of AB. At a certain temperature T_g, the volume-temperature graph undergoes a significant change in slope and continues almost parallel to the contraction graph CD of the crystallization form. T_g is called the transformation or glass transition temperature. Only below T_g is the material a glass. The location of E, the point corresponding to T_g, varies with the rate of cooling - and thus it is appropriate to call it a transformation *range* rather than a fixed point. At T_g the viscosity of the material is very high – about 10^{13} poise.

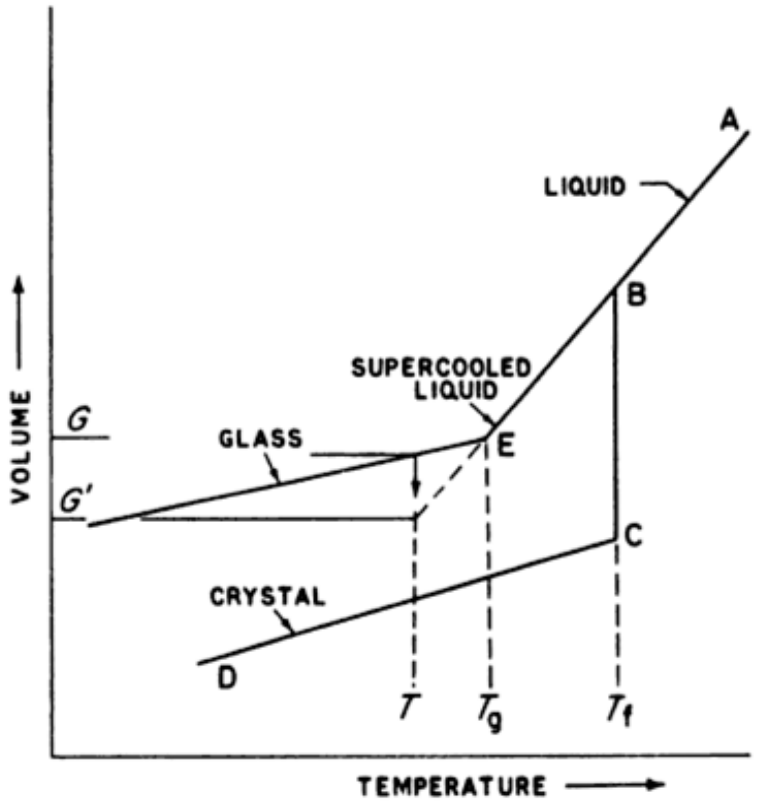

Fig 1.2 Relationship between the glassy, liquid and solid states

If the temperature of the glass is held constant at T, which is a little below T_g, the volume G will continue to decrease slowly. Eventually it reaches the level G^1 on the dotted line, which is a smooth continuation of the contraction graph BE of the

supercooled liquid (undercooled is perhaps a more appropriate word). Other properties of the glass also change with time in the vicinity of T_g. This process by which the glass reaches a more stable condition is known as stabilization. Above T_g no such time-dependence of properties is observed. As a result of the existence of the stabilization effects, the properties of a glass depend to a certain extent on the rate at which it has been cooled, particularly through the transformation range.

Liquids can also be transformed into the glassy state by the application of pressure. A glass is a state of matter which maintains the energy, volume and atomic arrangement of a liquid, but for which the changes in energy and volume with temperature and pressure are similar in magnitude to those of a crystalline solid. These considerations indicate that the glass transition has more or less the characteristics specified for a second-order thermodynamic transition. Whether or not it is a true thermodynamic transition is a question that has not yet been satisfactorily answered.

1.2 Glass formers

The ability of a substance to form a glass does not depend upon any particular chemical or physical property. It is now generally agreed that almost any substance, if cooled sufficiently fast, could be obtained in the glassy state - although in practice crystallization intervenes in many substances.

Glass-forming elements:

Of all the elements in the Periodic Table, only a few in Groups V and VI can form a glass on their own:

Phosphorus: White phosphorus when heated at 250^{o}C under a pressure of more than 7kbar produces a glass. The same material can also be prepared by heating white phosphorus with mercury (catalyst) in an evacuated seated tube at 380^{o}C.

Oxygen: Oxygen has been claimed to be prepared in the glassy form by cooling liquid oxygen, but this is controversial, since the material may be the cubic γ–phase of crystalline oxygen.

Sulphur and selenium: Sulphur and selenium form glasses easily with different ring and chain equilibria.

Tellurium: On the basis of irregular volume changes when molten tellurium solidifies, it has been suggested that tellurium may form a glass, and was proved that with ultra fast cooling, it is possible to prepare glass from pure TeO_2.

Glass-forming oxides:

B_2O_3, SiO_2, GeO_2 and P_2O_5 readily form glasses on their own and are commonly known as 'glass-formers' for they provide the backbone in other mixed-oxide glasses. As_2O_3 and Sb_2O_3 also produce glass when cooled very rapidly. TeO_2, SeO_2, MoO_3, WO_3, Bi_2O_3, Al_2O_3, Ga_2O_3 and V_2O_5 will not form glass on their own, but each will do so when melted with a suitable quantity of a second oxide. Figure 1.3 shows a section of the periodic table, the ringed elements having simple glass-forming oxides and the boxed elements having the second type of oxides, 'conditional glass-formers' according to Rawson[1]. An extensive coverage of the binary, ternary and quaternary glass forming systems has been made by Volf [2]. Ranges of glass formation in some simple binary systems containing B_2O_3, SiO_2, GeO_2 or P_2O_5 and any of the alkali metal oxides are given by Imaoka [3].

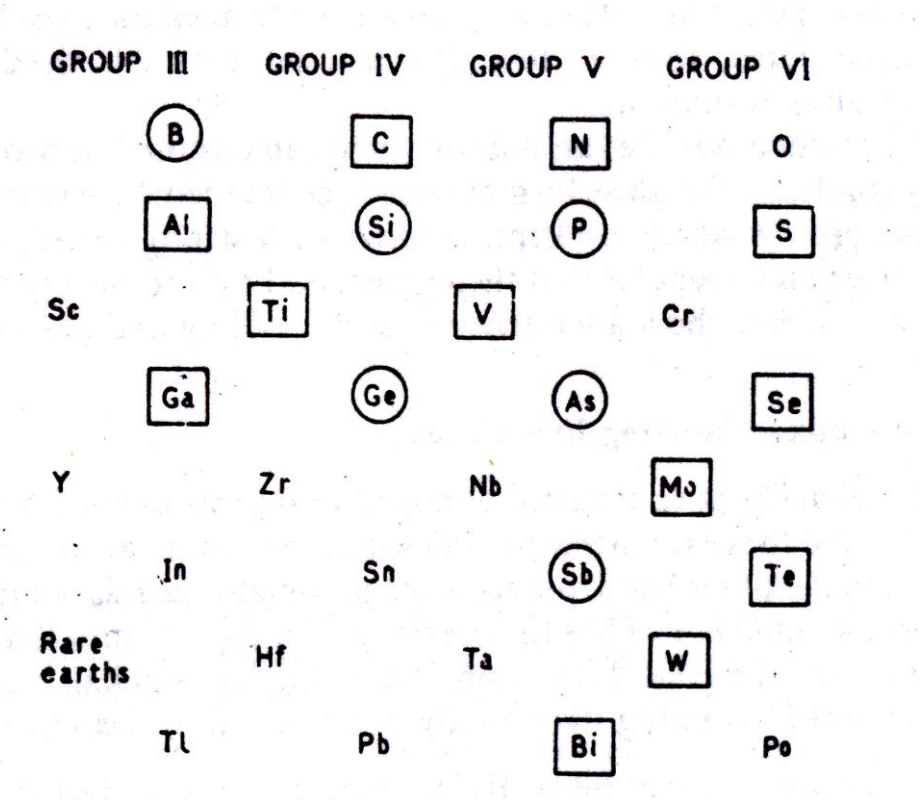

Fig 1.3 Elements, the oxides of which are either glass-formers or conditional glass-formers

1.3 Atomistic hypotheses of glass formation

Glass formation is a kinetic phenomenon; any liquid, in principle, can be transformed into glass if cooled sufficiently quickly and brought below the transformation range. A good glass-forming material is then one for which the rate of crystallization is very slow in relation to the rate of cooling. With conventional rates of cooling, some melts produce glass more easily than others. These facts lead many workers to postulate different atomistic hypotheses correlating the nature of the chemical bond and the geometrical shape of the groups involved, with the ease of glass formation.

1.3.1 Goldschmidt's radius ratio criterion for glass formation

According to Goldschmidt [4] for a simple oxide of the general formula A_mO_n, there is a correlation between the ability to form glass and the relative sizes of the oxygen and A atoms. Glass-forming oxides are those for which the ratio of ionic radii R_A/R_O lies in the range 0.2 to 0.4. For ionic compounds the coordination number is often dictated by the radius ratio rule. From simple geometrical considerations of the maximum number of spherical anions packed around a cation maintaining anion-cation contact, the results set out in Table 1.1 can be calculated. Thus according to Goldschmidt, a tetrahedral configuration of the oxide is a prerequisite of glass formation. However, it should be pointed out that in glass-forming oxides the anion-cation bonding is far from purely ionic. Besides, in the case of $9TeO_2$: PbO the coordination number of Te is six and not four. BeO with R_{Be}/R_O~ 0.0221 does not form glass.

Table 1.1: Limiting radius ratios for various coordination polyhedral

Polyhedron ratio	Coordination number	Minimum radius
Equilateral triangle	3	0.155
Tetrahedron	4	0.225
Trigonal bipyramid	5	0.414
Square pyramid	5	0.414
Octahedron	6	0.414
Cube	8	0.732

1.3.2 Zachariasen's random network hypothesis

Since the mechanical properties and density of an oxide glass are similar to those of the corresponding crystal, the interatomic distances and interatomic forces must also be similar. Zachariasen [5] postulated that, as in crystals, the atoms in glass must form extended three-dimensional networks. But the diffuseness of the X-ray diffraction patterns shows that the network in glass is not symmetrical and periodic as in crystals. For example, in the case of SiO_2 the only difference between the crystalline and glassy forms is that in vitreous silica the relative orientation of adjacent silicon-oxygen tetrahedral is variable whereas in the crystalline form it is constant throughout the structure. Such a difference is shown pictorially in figure 1.4 for an imaginary two-dimensional oxide (A_2O_3) in both crystalline (a) and vitreous (b) forms.

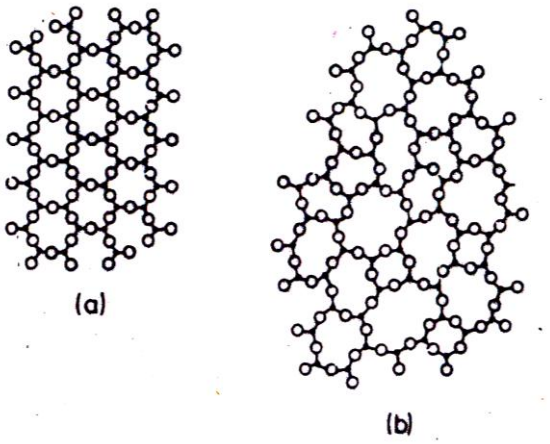

Fig.1.4. Schematic two-dimensional representation of the structure of (a) a hypothetical crystalline compound A_2O_3 and (b) the glassy form of the same compound

Zachariasen proposed a set of empirical rules which an oxide must satisfy if it is to be a glass-former:

(1) No oxygen atom may be linked to more than two atoms of A.

(2) The number of oxygen atoms surrounding A must be small (probably 3 or 4).

(3) The oxygen polyhedra share corners with each other, not edges or faces.

If it is further required that the network be three-dimensional, a fourth rule must be added:

(4) At least three corners of each polyhedron must be shared.

Zachariasen's hypothesis has been more or less universally accepted; however, the following limitations are pertinent and should be pointed out here.

(1) Although in most of the oxide glasses the coordination number of oxygen is two, Bray [6] has reported that in binary Tl_2O-B_2O_3 glasses with low Tl_2O content, the coordination number of oxygen may be three.
(2) The coordination numbers of silicon, phosphorus and boron in glass are 4, 4 and 3 or 4 respectively. However, as described earlier, the coordination number of tellurium in PbO-TeO_2 glasses is 6 with respect to oxygen. Alkali-phosphate glasses containing more than 50mol% alkali oxide contain two-dimensional chains of various sizes, thus a three-dimensional network need not be a prerequisite for glass formation.
(3) Hagg [7] pointed out that an infinite three-dimensional network may not be a necessary condition for glass formation. He concluded: 'it seems as if a melt contains atomic groups which are kept together with strong forces and if these groups are so large and irregular that their direct addition to the crystal lattice is difficult, such a melt will show a tendency to supercooling and glass formation'.

1.3.3 Smekal's mixed bonding hypothesis

According to Smekal [8] pure covalent bonds have sharply defined bond-lengths and bond-angles and these are incompatible with the random arrangement of the atoms in glass. On the other hand, purely ionic or metallic bonds completely lack any directional characteristics. Thus the presence of 'mixed' chemical bonding in a material is necessary for glass formation. According to Smekal, glass-forming substances with mixed bonding may be divided into three classes as follows:

(a) Inorganic compounds, e.g. SiO_2, B_2O_3, where the A-O bonds are partly covalent and partly ionic.
(b) Elements, e.g. S, Se having chain structures with covalent bonds within the chain and Van der Waals' forces between the chains.
(c) Organic compounds containing large molecules with covalent bonds within the molecule and Van der Waals' forces between them.

1.3.4 Sun's bond-strength criterion for glass formation

Since the process of atomic rearrangement which takes place during the crystallization of a material may involve the breaking and reforming of interatomic bonds, it may be reasonable to expect a correlation between the strength of these bonds and the ability of the materials to form a glass. The stronger the bonds, the more sluggish will be the rearrangement process and hence the more readily will a glass be formed. This suggestion was first put forward by Sun [9], who showed that the bond strengths in glass-forming oxides are in fact particularly high. From Sun's calculations, the glass-forming oxides have single bond strengths greater than 90kcal mol^{-1} and the modifiers have bond strengths less than 60kcal mol^{-1}.Sun himself pointed out that, although the bond strengths V-O, As-O and Sb-O are relatively high, the oxides are not good glass-formers. In fact V_2O_5 will not form a glass when melted alone. Sun suggested that 'small ring formation' may occur in the melts of these materials, which would result in easy crystallization.

A few other hypotheses, like winter's p-electron criterion [10], Rawson's modification of Sun's hypothesis [11] etc., have been put forward from time to time. But none of these hypotheses are really capable of explaining glass formation to a more satisfactory extent than already described.

1.4. Devitrification:

Most glass-forming melts show some sign of crystallization (devitrification) if heated just below the liquidus temperature for a period of time ranging from minutes to hours. The liquidus temperature is the temperature below which a single liquid phase is no longer thermodynamically stable. If a melt consisting of two or more components is cooled to a temperature just below the liquidus, it does not, in general, crystallize as a whole. When equilibrium is reached, it usually consists of a mixture of a solid crystalline phase and a liquid. The liquidus temperature varies with temperature in a complicated way.

1.4.1Nucleation and Crystal Growth:

The process by which optically visible crystals form in a melt below the liquidus temperature requires the existence of nuclei which act as centres from which larger

crystals can grow. These nuclei are crystalline regions, often of sub-microscopic size. They may form spontaneously in the melt if its temperature is sufficiently below the liquidus temperature, in which case we speak of homogeneous nucleation. These being materials which readily precipitate from the melt when it is cooled and form a very high density of nuclei. The crystals which grow from the melt then have a composition which differs radically from that of the nuclei. Finally, there are situations in which crystals grow from foreign material inadvertently present in the melt; such as fragments of refractory, particles of incompletely melted material, or particles of dust on the melt surface. In these situations, where the nuclei are not formed spontaneously from the major constituents of the melt but can be regarded as foreign material, we speak of heterogeneous nucleation.

Crystallization [12] is a process by which the regular lattice of the crystal is generated from the less well-ordered liquid structure. The crystallization does not occur simultaneously throughout the mother phase. It proceeds from distinct centres and crystal growth takes place by deposition of material upon the first tiny crystals or nuclei. Two parts of crystallization process are therefore distinguished: Nucleation and Crystal growth. Nucleation involves the formation of regions of longer-range atomic order than are normally present. These unstable intermediate states are known as embryos and embryos having a critical minimum size, which are capable of developing spontaneously into gross particles of the stable phase, are known as nuclei.

During the crystallization most of the properties of the glasses degrade. Therefore, a study of these properties as a function of temperature can reveal details of crystallization processes involved and provide information on the thermal stability of the system. As the thermal stability against crystallization determines their effective working limits for these glasses the crystallization studies can therefore be of immense value in controlling crystallization process. Hence for technological application, knowledge of process that governs the thermal stability of these materials is of considerable importance. The theoretical as well as experimental studies on phase transformation in glasses from glassy to crystalline state have been done using techniques like DSC, DTA, Electron Microscopy, Mosssabour effects and EDAX etc.

1.5 Types of Amorphous materials:

Chalcogenide glasses: Glasses based on the elements S, Se and Te in combination with other elements, especially As, Sb, Ge and Si have been intensively studied in recent years on account of their interesting electrical and optical properties. This group is referred to as the chalcogenide glasses.

Oxide glasses: There are number of interesting glass forming systems based on the oxides GeO_2, P_2O_5, TeO_2, V_2O_5 and a few others. These glasses are called oxide glasses. Transition metal (TM) oxides when heated with GeO_2, P_2O_5 and TeO_2 etc., form glasses on quenching the melt. These glasses show interesting semiconducting properties. Most commercially important glasses are oxide glasses and silica is almost always a major component.

Metallic glasses: One of the most exciting discoveries of recent years in glass technology is that many metallic alloys can be produced in glassy form. To prevent the melts from crystallizing it is necessary to cool them much more rapidly than the silicate glass-forming melts. Consequently, in order to obtain a high rate of heat extraction throughout the thickness of the material, metallic glasses can be made only as thin ribbons or foils. Their properties vary over a very wide range. Some have an extremely high tensile strength combined with remarkably high ductility. Others have a high corrosion resistance. Others have interesting magnetic properties. They are magnetically very "soft" i.e., they may be magnetized very easily by the application of small magnetic fields. All these materials, like their crystalline counterparts, are excellent conductors of heat and electricity.

1.6 Oxide glasses:

Oxide glasses containing TM oxides are very important for many of their technological applications like switching and memory devices, cathode ray tube materials, ferrites and fast photonic switching etc. With recently discovered Bi-based nonconventional glasses, it is found advantageous to make wires, tapes or thick films from glass matrix and then convert them to high-T_c superconductors by annealing them at high temperatures.

The present work concerns the studies on tellurium oxide and bismuth oxide glasses containing TM elements. We present here the previous work done on the tellurite and bismuthate glasses with TM ions and the objective of the present work.

1.6.1 Tellurite glasses:

Tellurium oxide-based glasses are the subject of intense current research because of the interesting electrical and optical properties. Main features include extended infrared transmittance [13], high linear and non-linear optical indices [14], low fusion temperature and good chemical resistance. The tellurite glasses are technologically important since they are known to have low melting temperature, high chemical stability, high homogeneity, high refractive index, high dielectric constant, and high transmittance from ultraviolet to near infrared. The TeO2-based glasses have been widely studied due to their possible applications in infrared and optoelectronic devices [15-18]. The addition of TM ions to these glasses shows semi conducting properties and finds applications in switching and memory devices [19,20]. The origin of these properties has been strongly correlated to the local order around tellurium atoms. The structure of tellurite systems has been investigated by several authors by means of X-ray diffraction (XRD), Raman spectroscopy or neutron diffraction [21-23]. These glasses have been considered as promising materials for fibre-optic amplifiers and fibre lasers. In comparison with silicate and borate glasses that are in use commercially; tellurite glasses have also more advantages as frequency up conversion laser hosts due to their physical properties such as low melting temperature, high dielectric constant, high refractive index, large third-order nonlinear susceptibility, better infrared transmissivity, low phonon energies, and therefore, glass have small multi-phonon decay rates for the excited states when they are doped with the rare earth ions[24-26]. In addition, tellurite glasses are resistant to atmospheric moisture and capable of incorporating large concentrations of rare earth ions such as Tm^{3+} into the matrix and this absence of hygroscopic nature which limit applications of phosphate and borate glasses. The refractive index, n, and density, ρ, for many oxide glasses can be varied by changing the glass composition, sample temperature, pressure, and transformation range history such as reannealing[26,27].

TeO_2 by itself can be transformed to a glassy state only by employing ultrafast quenching techniques, or by introducing a network modifier as a second component.

Thus, TeO_2 is known to be a conditional glass former. Further, TeO_2 readily forms glasses [28, 29] with transition metal oxides (TMO) such as V_2O_5 and Fe_2O_3 in which TM ions exist in different valence states. The electrical conductivities of these materials are several orders of magnitude higher than silicate, borate and phosphate glasses containing the same amount of TMOs.

TeO_2 glass is known to consist of TeO_4 trigonal bipyramids (tbp) , in which one of the equatorial sites is occupied by a lone pair of electrons, and that most of the tellurium atoms are connected at vertices by Te-$_{eq}O_{ax}$-Te linkage. The TeO_2 glass has an unique structure as a consequence of the structural unit and its connecting style differs from the conventional glass formers, such as B_2O_3, SiO_2, GeO_2 and P_2O_5. So far, several investigations have been made to determine the structure of alkali tellurite glasses [30-35]. Mochida et al[30] showed that the primary structural unit of tellurite glasses having high TeO_2 content is a distorted TeO_4 tbp and that the fraction of TeO_3 trigonal pyramids (tp's)increases with increasing mono- or di-valent cation content. Figure 1.5 describes the structure of TeO_4 tbp and the transformation of TeO_4 tbp to TeO_3 tp through an intermediate polyhedra TeO_{3+1}.the TeO_4 tbp group has two axial and two equatorial oxygen atoms, in which the third equatorial position of the sp3d hybrid orbital is occupied by an electronic pair. The presence of this electronic pair exhibits a key role in the structure building and manifestation of the non-linear optical properties of the tellurite glasses [31]. It is proposed that the transition between the TeO_4 and TeO_3 structures is made by the shortening of one of the axial bond while one equatorial bond gets longer (TeO_{3+1} polyhedra), when the modifier content increases [31, 36].

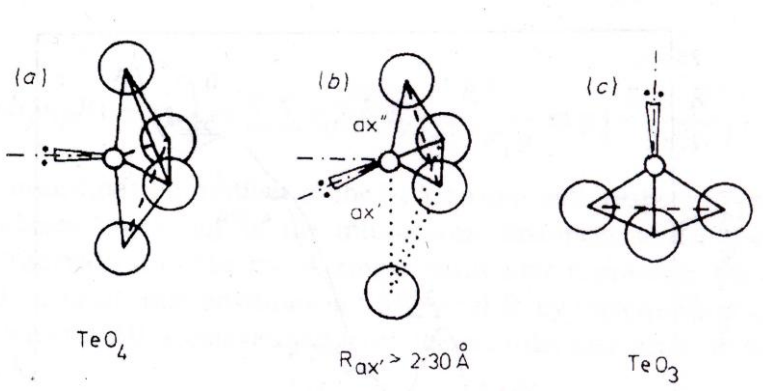

Fig.1.5. types of 'open' structure with coordination numbers (a) 4 (b) 3+1 (c) 3 respectively

1.6.3 Bismuthate glasses:

The physical properties of oxide glasses containing heavy metal oxide like bismuth combined with other classical vitreous network formers like SiO_2, B_2O_3, P_2O_5 or GeO_2 are characterized by high refractive index, excellent infrared transmission, high nonlinear optical susceptibility and high polarizability [37-41]. Their physical properties imply interesting applications as thermal and mechanical sensors [38,41], waveguides in nonlinear optics [42], scintillator detectors in high-energy physics [42-44] as well as starting materials for high-temperature superconductors [38, 45, 46]. These reasons determined intense investigations of disordered bismuthate materials.

As reported Bi_2O_3 alone cannot easily form the vitreous state [39, 40]. On the other hand there are few studies regarding the binary glass systems based on Bi_2O_3 as unique network former [38-41]. In the glass systems the bismuth ions may appear as network formers in $[BiO_3]$ pyramidal and $[BiO_6]$ octahedral units [39-47].

Multi component non-conventional glasses based on Bi_2O_3 are of great interest because they form amorphous materials without any conventional network formers like B_2O_3, P_2O_5, etc. Bismuth based glasses are used to produce glass ceramic superconductors (high T_c) with controllable microstructure [45, 46, 48-51]. Although Bi_2O_3 is not in itself a glass former, because of its highly polarisable nature the coordination number of Bi^{3+} ion may decrease and cations may exist in the glass network in $[BiO_3]$ pyramids in the presence of conventional glass forming cations. Non-conventional glasses using Bi_2O_3 as the basis of glass network of multi-component systems have been reported (52-53). Bismuth based glasses are also used in the fabrication of switching and memory devices. Many glass systems based on Bi_2O_3 have been reported by several authors. Several investigators reported that oxide glasses containing a large amount of magnetic ions show magnetic transitions as observed in spin glasses or superparamagnets [54-56]. In our present case the multicomponent Bi_2O_3 glasses containing ZnO, PbO and Fe_2O_3, we could observe spin dynamics at temperatures just below the room temperature.

1.7 Properties and literature survey of Tellurite and Bismuthate glasses:

Structural, electronic, optical, magnetic and mechanical properties of these glasses depend upon the relative ratio of the different valence states of the TM ions present [57-60]. In order to account for the effect of the valence states on the structure and properties of these glasses, it is important to control and measure the ratios of the TM ion concentration in the different valence states of these oxide glasses. Semi conducting properties of some tellurite and bismuthate glasses containing transition metal oxides have been reported by several groups[61-66]. In the present work, we concentrated on four different kinds of studies to understand thermal, structural and magnetic properties.

A. DSC studies:

Differential Scanning Calorimetric (DSC) is a thermo analytical technique used in understanding crystallization kinetics of glasses which is associated with the study of parameters like glass transition temperature (T_g), crystallization onset (T_o) and crystallization temperature (T_p) and the activation energy of crystallization (E_c). This technique is simple, informative and useful for identifying glass compositions with high thermal stability and synthesizing glass ceramics with controlled heat treatment. The crystallization studies of glasses were carried out by using DSC instrument. The heat evolved is recorded as a function of temperature. Heat changes either exothermic or endothermic are caused by phase transitions, such as fusion, boiling, sublimation, dehydration, crystallization etc. In general, oxide glasses may have more than one crystallization temperature. In DSC thermograms each peak is characterized by a peak temperature T_p. $\Delta T=T_o-T_p$, resistance to crystallization or thermal stability, is a measure of the strength of the glass. Knowledge of crystallization process is important for identifying glass compositions with high resistance towards devitrification and for fabricating glass ceramics through controlled crystallization.

There are some reports in the literature on the DSC studies of tellurite glasses containing 3d transition metal (TM) ions [58-60, 67-72]. Here, we present the systematic crystallization studies on various compositions of tellurite and bismuthate glasses. The crystallization kinetics is studied for some of the synthesized glasses and data is analyzed in view of Kissinger [73-74] and Matusita & Sakka models[75-76]. The activation

energy for crystallization and dimension of crystallization were calculated for some of the glass samples.

B. IR studies:

The infrared (IR) spectroscopy is very useful in determining the structure of the glass. The absorption spectra of glasses in the IR region are largely determined by interactions between the material and the radiation which excite atomic vibrations. These may involve oscillatory changes in interatomic distances (bond stretching) or in bond angles (bond bending). It is a more difficult problem to predict theoretically the modes of vibration and the frequencies of atomic vibration of solids which have an infinite three dimensional structure, unless the structure is a simple crystalline one. In amorphous material lattice absorption processes are retained to a degree which depends on the material. The fine structure present in the spectra of corresponding crystalline materials is lost. Much of the work which has been done in an attempt to interpret the IR spectra of oxide glasses has simply involved comparisons between the spectra of the glasses with those of crystalline compounds of known structure. IR absorption spectra have been used previously in an attempt to ascertain whether any kind of local order characteristic of the constituent oxides is maintained in the glass.

There is a vast literature on IR-spectroscopy studies on oxide glasses. A brief summary of studies on V_2O_5, TeO_2 and Bi_2O_3 based glasses is given in the following paragraphs.

The IR spectroscopy has also been useful to construct the structural models of the R_nO_m-TeO_2 glass system. The binary tellurite systems have been investigated for their structure. These systems are TeO_2 with V_2O_5[77], Li_2O[78], P_2O_5[79], B_2O_3[80], WO_3[81], MoO_3[82], ZnO[83] and the ternary system TeO_2-B_2O_3-K_2O[84]. The IR studies show that the structural units in tellurite glasses are similar to that of the crystals. The tellurite glasses consist of the polyhedral: TeO_4 – trigonal bipyramids, deformed TeO_4 groups, TeO_3 trigonal pyramids or combination of these polyhedral. The introduction of the modifier MoO_3 or ZnO in the binary glasses leads to a $TeO_4 \rightarrow TeO_{3+1} \rightarrow TeO_3$ transition. Dimitriev et. al[85] reported extensive IR-spectral studies of tellurite vitreous systems. They studied the effect of addition of transition metal oxide on the structure of vitreous TeO_2.

There are a number of studies on the structure of Bismuth glasses [86-90]. The systematic studies presenting different ideas as to its role in glass structure on Bi_2O_3-K_2O, Bi_2O_3-B_2O_3 and ternary Bi_2O_3-B_2O_3-R_2O systems by Bishay and Maghrabi [90] indicate that Bi_2O_3 may affect the structure in three different ways. They are

(1) it gives part of its oxygen to the boron to create four coordinated sites
(2) it participates in the structure by forming Bi_2O_3 groups; and
(3) it introduces some non-bridging oxygens in the structure.

C. ESR studies:

All forms of spectroscopy are based on the determination of energy levels of molecules, atoms and nuclei. These energy levels are created by interactions which can take place between matter and radiation. ESR is restricted to the study of magnetic dipoles of electronic origin and is usually studied at microwave frequencies (10^9 to 10^{11} Hz). ESR essentially consists of observing transitions between the Zeeman levels of the unpaired electron in an external magnetic field. Observing the magnetic field at which resonance occurs may allow one to determine the magnetic dipole moment, the local environment of paramagnetic species and any other non magnetic splitting (like zero field splitting).

The ESR spectra of TM ions in glasses were first investigated by Sands [91]. Griscon [92] has reviewed various types of ESR studies which have been performed on glasses. Various studies (67-69, 93-101) have been carried out on glasses containing TM oxides to understand the magnetic interactions. Some of these studies also include magnetic susceptibility measurements [67,68,97,100]. Ardelean et. al have recently reported ESR and magnetic susceptibility studies on TeO_2-B_2O_3-PbO glasses containing Cu (Ref.102), Fe(Ref.103) or Mn (Ref.104) ions.

D. Magnetization studies:

Magnetic susceptibility measurements are very useful for determining structural distribution in the glass matrix, the valence states of transition metal ions and the type of interactions involving them over a varied composition range, depending on the glass network structure. Few studies on magnetic interactions between iron ions have been reported in borate [105,106], phosphate [107,108], tellurite [67,68,109], lead-bismuthate

[110,111] and silicate [112,113] oxide glasses. Oxide glasses containing large amount of magnetic ions are a prototype of a solid in which magnetic moments are randomly distributed. Several investigators reported that oxide glasses containing a large amount of magnetic ions show magnetic transitions as observed in spin glasses or superparamagnets [106, 114-116]. Below spin glass transition temperature, magnetic moments are frozen in such a manner that the direction of each of the magnetic moments is randomly oriented, but it takes an infinite time to reach a thermodynamic equilibrium state. Measurements of the temperature and field dependences of the dc magnetization can provide information about the magnetic characteristics of the glass samples. Also the results of these measurements can provide quantitative information including determinations of the Curie temperature, Curie constant, effective magnetic moment for the samples.

1.8 Objective of the present work:

The objective of the present work is to carry out systematic DSC, IR, ESR and magnetization measurements on some tellurite and bismuthate glass systems containing transition metal oxides (CuO and Fe_2O_3). The variation in composition gives rise to structural changes which can alter the properties of the glass. Thus a correlation between the structure and the properties of the glass can be established.

The magnetic properties in the glass is affected by several factors like the nature and concentration of the TM ions, the concentration of TM ion in reduced valence state, the preparation conditions and the microscopic or macroscopic structure of the glass. The studies reported in the literature are on a single system containing a specific TM ion. As a result the range of parameters obtained by changing the glass composition and the preparation conditions is limited which makes it difficult to assess the effect of parameters which may be correlated.

To understand the thermal and structural properties, DSC and IR studies were done. The variation of the parameters with the composition variation of glasses was highlighted. Activation energy for crystallization and dimensionality of crystallization were calculated for some of the series

In the present work the properties of various glasses (binary, ternary and quaternary) containing different TM ions (Cu and Fe) are compared to arrive at some common

conclusions on the thermal, structural and magnetic nature of the glasses. The glass systems included in the present work are as follows:

1. (100-x)TeO_2 – xCuO, where x = 10, 20, 30, 40 and 50.
2. (20-x) ZnO - 80TeO_2 – xFe_2O_3, where x = 0, 5, 10,15 and 20.
3. 20ZnO- (80-x) TeO_2- xFe_2O_3, where x = 0, 1, 3, 5 and 7.
4. 10Fe_2O_3 – (90-x) TeO_2 –x Bi_2O_3, where x = 0, 5, 10, 15 and 20.
5. 20Fe_2O_3 - (80-x)TeO_2 –x Bi_2O_3, where x = 0, 5, 10, 15, 20 and 25.
6. (100-x) (70Bi_2O_3 20ZnO 10 PbO) – xFe_2O_3, where x = 0, 5, 10, 15, 20 and 25.

The DSC, IR, ESR and magnetization measurements can help in correlating the short range magnetic interactions and their correlation with the structure of the glass.

Thesis consists of five chapters.

Chapter 1 reviews the relevant literature and the objectives of the present work.

Chapter 2 describes the synthesis and preparation of glass samples and the experimental techniques used to understand the physical properties of the glasses.

Chapter 3 describes the x ray diffraction (XRD), Differential Scanning Calorimeter (DSC) and Infrared spectroscopic (IR) studies of the synthesised glasses.

Chapter 4 includes the Electron Spin Resonance (ESR) studies of various the glass samples.

Chapter 5 includes the magnetization studies of the glasses. Various magnetic parameters i.e. Curie temperature, molar curie constant, effective magnetic moment etc. are estimated from the magnetization data.

The summary and Conclusions section summarises the work presented in the thesis.

References:

[1] H. Rawson, *Properties and Applications of Glass*, Glass science and Technology volume Elsevier, New York (1980).

[2] H. Volf, *Chemical Approach to Glass, Academic Press*, London (1981).

[3] M. Imaoka, *Advances in Glass technology, Part 1, Plenum Press*, New York p 149.

[4] V.M. Goldschmidt,Skrifter Norske Videnskaps Akad (Oslo), I. Math-Naturwiss. Kl. **8**, p.7.

[5] W. H. Zachariasen, *J. Am. Chem. Soc*., **54**, 3841 (1932).

[6] J.F. Baugher and P. J. Bray, *Phys. Chem. Glasses*, **10**, 77(1969).

[7] G. Hagg, *J. Chem. Phys*., **3**, 42 (1935).

[8] A. Smekal, *J. Soc. Glass Technol*., **35**, 411 (1951).

[9] K.H. Sun, *J. Am. Ceram. Soc*., **30**, 277 (1947).

[10] A. Winter, Verres Refract., **9**, 147 (1955).

[11] H. Rawson, in Proc. IV Internat. Congr. On Glass, Imprimerie Chaix, Paris (1956).

[12] P.W. McMillan, *Glass Ceramics, Academic Press*, London, New York, Sanfransisco).

[13] M.J. Waber, J.D. Meyers, D.H. Blackburn, *J. Appl. Phys*. **52 (4)** 2944 (1981).

[14] K. Shioya, T. Kmatsu, H.G. Kim, R. Sato, K. Matusita, *J. Non-Cryst. Solids* **189** 16 (1995).

[15] N. Ovcharenko, A. Yakhkind *Opt Mech Prom* **3** :47 (1968)

[16] M. E. Lines *J Appl Phys* **69** : 6876 (1991)

[17] S. H. Kim, T. Yoko, S. Sakka *J Am Ceram Soc* **76** : 2486 (1993)

[18] J. S. Wang, E. M. Vogel, E. Snitzer *Opt Mater* **3** : 187 (1994)

[19] E. Gateff and Y. Dimitriev *Philos Mag* **40** : 233 (1979)

[20] C. Chung and J. Mackenzie *J Non-Cryst Solids* **42** : 357 (1980)

[21] T. Sekiya, N. Mochida, A. Ohtsuka, *J. Non-Cryst. Solids* **168** 106-114 (1994).

[22] C. Dewan, A.J. Edwards, G.R. Jones, I.M. Young, J.C.S. Dalton 1528 (1978).

[23] S. Neov, V. Kozhukharov, C. Trapalis, P. Chieux, *Phys. Chem. Glasses* **36 (2)** 89-94 (1995).

[24] B. V. R. Chowdari and P. P. Kumari *Solid State Ionics*, **113-115**, 665-675 (1998).

[25] J. E. Stanworth Nature, **169** 581-582 (1952).

[26] S. Xu, G. Wang, J. Zhang, S. Dai, L. Hu and Z. Jiang *J. Non-Cryst. Solids*, **336** 230-233 (2004).

[27] A. Sennaroglu, I. Kabalci, A. Kurt, U. Demirbas and G. Ozen *J. Lumin*., **116** 79-86 (2005).

[28] V.K. Dhawan, A. Mansingh and M. Sayer, *J. Non-Cryst. Solids* **51** 87 (1982).

[29] H. Binczycka, O. Gzowski, L. Murawski and J. Sawichi, *Phys. Status Solidi (a)* **70** 51 (1982).

[30] N. Mochida, K. Takahashi, K. Nakata and S. Shibusawa, Yogyo-Kyokai-Shi **86** (1978) 316.

[31] S. Noev, V. Kozhukharov, I. Geraimova, K. Krezhov and B. Sidzhimov, *J. Phys. C. Solid State Phys.* 12 2475 (1979).

[32] T. Nishida, S. Saruwatari and Y. Takashima, *Bull. Chem. Soc. Jpn*. **61** 4093 (1988).

[33] T. Yoko, K. Kamiya, H. Yamada and K. Tanaka, *J. Am. Ceram. Soc*. **71** C70 (1988).

[34] K. Tanaka, T. Yoko, H. Yamada, and K, Kamiya, *J. Non-Cryst. Solids* **103** 250 (1988).

[35] T. Yoko, K. Kamiya, K. Tanaka, H. Yamada and S. Sakka, *J. Ceram. Soc. Jpn.* **97** 289 (1989).

[36] T. Sekiya, M. Mochida, A. Ohtsuka, M. Tonokawa, *J. Non-Cryst. Solids* **144** 128 (1992).

[37] W.H. Dumbaugh and J. C. Lapp, *J. Am. Ceram*. Soc. **75**, 2315 (1992).

[38] L. Baia, D. Maniu, T. Iliescu, S. Simon, S. Schlucker and W. Kieffer, *Asian J. Phys*. **9**, 51 (2000).

[39] S. Hazra and A. Ghosh, *Phys. Rev. B* **51**, 851.

[40] Y. Dimitriev and V. T. Mihailova, *J. Sci. Lett.* **9**, 1251 (1990).

[41] S. Hazra and A. Ghosh, *Phys. Rev. B* **56**, 13 (1997).

[42] C. Stehle, C. Vira, D. Hogan, S. Feller and M. Affatigato, *Phys. Chem. Glasses* **39**, 836 (1998).

[43] S. E. Van Kirk, S.W. Martin, *J. Am. Ceram. Soc*. **75**, 2315 (1992).

[44] N. Ford and D. Holland, *Glass Technol*. **28**, 106 (1987).

[45] T. Komatsu, R.sato, K. Imai, K. Matusita and T. Yamashita, *J. Appl Phys*. **27 L** 550 (1998)

[46] T. Minami, Y.Y.Akamatsu, M. Tatsumisago Tohge and Y. Kowada, *J. Appl. Phys*. **27L**, 777 (1998).

[47] H. Zheng, R. Xu and J.D. Mackenzie, *J. Mat. Res*. **4**, 911 (1989).

[48] H. Zheng and J.D. Mackenzie, *Phys. Rev.* B **38** 7166 (1988).

[49] M. Tatsumisago, S. Tsuboi, N. Toghe and T. Minami *J. Non-Cryst. Solids* **124** 167 (1990).

[50] M. Onisi, M. Kyoto and M. Watanabe *Jpn J. Appl. Phys.* **30** L988 (1991).

[51] L. R. Yuan, K. Kurosawa, Y. Takigawa, M. Okuda, H. Naito, K. Nakahigashi, S. Nakanishi and T. Matsushita *Jpn J Appl. Phys.* **30** L1545 (1991).

[52] W. H. Dumbaugh *Phys. Chem. Glasses* **19** 121 (1978).

[53] W. H. Dumbaugh *Phys. Chem. Glasses* **27** 119 (1986).

[54] K. Tanaka, H. Akamatsu, S. Nakashima and K.fujita, *J. Non-Crys. Solids* **354**, 1346 (2008).

[55] Joanna L. Shaw, Ardian C Wright, Roger N. Sinclair, G. Kanishka Marasinghe, Diane Holland, Martin R. Lees, Charlie R. Scales, *J. Non-Crys. Solids* **345 & 346**, 245 (2004).

[56] R. A. Verhelst, R.W. Kline, A.M. de Graaf, H. O. Hooper, *Phys.Rev. B* 11 4427 (1975).

[57] E. E. Shaisha, A. A. Bahgat and A. I. Sabry *Jr of Mat. Sci. Lett.* **5** 687-689 (1986).

[58] R. Singh *J. Phys.D.* **20** 548-551 (1987).

[59] A. A. Bahgat, I. I. Shaltout and A. M. Abu-Elazm *Jr. of Non-Cryst. Solids* **150** 179-184 (1992).

[60] B. V. R. Chowdari, K. L. Tan and Fang Ling 1998 *Solid State Ionics* **113-115** 711-721.

[61] M.R. Tripathy, R. Joshi, N.C. Mehra, S. Kumar, and R. P. Tandon, *Materials Letters*, **61(2),** 585 (2007).

[62] M. A. Hassan and C. A. Hogarth *Jr. of Mater.Science*. **23** 2500-2504 (1988).

[63] Aswini Ghosh *J. Phys: Condens. Matter* **1** 7819-7828 (1989).

[64] R. Singh and K. Sethupathi *J. Phys. Appl. Phys*. **22** and references therein L 709 (1989).

[65] R. Singh, J.S. Chakravarthi, *Phy Rev B* **55** 5550 (1997).

[66] R. Singh and J. S. Chakravarthi (1995) *Phys Rev B* **51** 16396.

[67] P. Sandhya Rani and R. Singh *J. Mater. Sci*. **45** 2868 (2010).

[68] P. Sandhya Rani and R. Singh *J Phys & Chem Solids* **74** 338-343 (2013).

[69] P. Sandhya Rani and R. Singh, *Solid State Phys (India)* **49** 356 (2004).

[70] P. Sandhya Rani and R. Singh, *Solid State Phys (India)* **51** 379 (2006).

[71] P. Sandhya Rani and R. Singh, *Solid State Phys (India)* **52** 469 (2007).

[72] P. Sandhya Rani and R. Singh, *Solid State Phys (India)* **53** 641 (2008).

[73] H. E. Kissinger: *J. Res. Nat. Bur. Stand*. **57**, 217-221 (1956).

[74] H. E. Kissinger: *Anal. Chem*. **29**, 1702 (1957).

[75] K. Matusita, Sumio Sakka: *Jr. of Non-Cryst. Solids* **38 & 39,** 741 (1980).

[76] K. Matusita, T. Komatsu, Ryosuse Yokota: *J. Mater.Sci*. **19**, 291 (1984).

[77] Y. Dimitriev, M. Arnaudov and V. Dimitrov, *Mh. Chem*. **107,** 1335 (1976).

[78] S. Noev, V. Kozhukharov, I. Geraimova, K. Krezhov and B. Sidzhimov, *J. Phys. C. Solid State Phys*. **12** 2475 (1979).

[79] S. Neov, I. Gerasimova, V. Kozhukharov and M. Marinov, *J. Mater. Sci*. **15**, 1453 (1980).

[80] H. Burger, W. Vogel, V. Kozhukharov and M. Marinov, *J. Mater. Sci*. **19**, 403 (1984).

[81] V. Kozhukharov, S. Neov, I. Gerasimova and P. Mikula, *J. Mater. Sci*. **21**, 1707 (1986).

[82] Y. Dimitriev, V. Dimitrov and M. Arnaudov, *J. Mater. Sci*. **18**, 1353 (1983).

[83] H. Burger, K. Kneipp, H. Hobert, W. Vogel, V. Kozhukharov and S. Neov, *J. Non Cryst. Solids* **151**, 134 (1992).

[84] K. Kneipp, H. Burger, D. Fassler and W. Vogel, *J. Non-Cryst. Solids*, **65** 223 (1984).

[85] Y. Dimitriev, v. Dimitrov, M. Arnaudov and D. Topalov, *J. Non-Cryst. Solids* **57** 147 (1983).

[86] J. T. Randall and H. P. Rooksby, *J. soc. Glass Technol.* **30** 287 (1933).

[87] M.S.R. Heynes and H. Rawson, *J. Soc. Glass Technol.* **41** 347 (1957).

[88] Bh. V. Janakirama rao, *J. Am. Ceram. Soc.* **45** (11) 555 (1962).

[89] C. Hirayama and C. Subbarao, *Physics Chem glasses* **3(4)**, 111 (1962).

[90] A. Bishay and C. Maghrabi, *Physics Chem Glasses* 10 (1), 1 (1969).

[91] R.H. Sands, *Phys. Rev.* **99** 1222 (1955).

[92] D. Griscom, and references therein *J. Non-Cryst. Solids*, **40** 211 (1980).

[93] R. Singh and references therein ***esr***. *J. Phys. D* **17** L57 (1984)

[94] L.D. Bogomolova, M.P. glassova, O.E. Dubtovko, S.I. Reiman and S.N. Spasibkina, *J. Non-Cryst. Solids*, **58**, 71 (1983).

[95] A. K. Bandyopadhyay and J.O.Isard, *J. Phys. D* **10** L99 (1977).

[96] L.D. Bogomolova, M.P. glassova, V.M. Kalygina, S.I. Reiman, S.N. Spasibkina and I.V. Filatova, *J. Non-Cryst. Solids*, **85** 170 (1986).

[97] I. Ardelean, O. Cozar and Ch. Ilonca, *J. Non-Cryst. Solids*, **68** 33 (1984).

[98] R. Singh *J Phys D:Appl. Phys.*,**17**, L163-L167 (1984)

[99] P. Sandhya Rani and R. Singh, *Solid State Phys (India)* **54**, 493 (2009).

[100] P. Sandhya Rani and R. Singh, *AIP Conf. Proc.* **1447**, 553 (2012).

[101] Dhanya R. Kurup and R. Singh, *Solid State Phys (India)* **49,** 380 (2004).

[102] I. Ardelean, M. Peteanu, E. Burzo and F. Ciorcas, *Solid State Comm.* **98**, 351(1996).

[103] I. Ardelean, M. Peteanu, S. Filip, V. Simon and g. Gyorffy, *Solid State Comm.* **102** 341 (1997).

[104] I. Ardelean, M. Peteanu, S. Filip and D. Alexandru, *J. Mag. Magnetic Mat.* **157/158**, 239 (1996).

[105] Rene Berger, Janis Klaiva, El-Mostapha Yahiaoui, Jean-Claude Bissey, Paul K. Zinsou and Pierre Beziade, *J. Non-Crys. Solids* **180**,151-163 (1995).

[106] Shiv Prakash Singh, R.P.S. Chakradhar, J.L. Rao and Basudeb Karmakar, *J. Alloys Compd* **493**, 256-262 (2010).

[107] B. Kumar and C.H. Chen, *J. appl. Phys*. **75**, 6760 (1994).

[108] Joanna L. Shaw, Ardian C Wright, Roger N. Sinclair, G. Kanishka Marasinghe, Diane Holland, Martin R. Lees, Charlie R. Scales, *J. Non-Crys. Solids* **345 & 346**, 245 (2004).

[109] A. Mekki, G.D. Khattak and L.E. Wenger, *J. Non-Crys. Solids* **352**, 3326-3331(2006).

[110] I. Ardelean, Gh.Ilonca, O.Cozar, V. Simon and S. Filip, *Mat. Lett.* **21**, 321 (1994).

[111] S. Simon, R. Pop, V.Simon and M.Coldea, *J. Non-Crys. Solids* **331**,1-10 (2003)

[112] Atsuko Ito, Eiko Torikai, Hiroshi Yamauchi and Yasuhiko Syono, *J. Phys. C: Solid State Phys.* **15,** 2759-2765 (1982).

[113] Rajendra Kumar Singh, G.P. Kothiyal and A. Srinivasan, *J. Non-Crys. Solids* **354**, 3166-3170 (2008).

[114] Katsuhisa Tanaka, Hirofumi Akamatsu, Seisuke Nakashima and Koji fujita, *J. Non-Crys. Solids* **354**, 1346 (2008).

[115] I.S. Edelman, T.V. Zarubina, S.A. Stepanov and T.A. Kim, *J. Mag. Mag. Mat.* **110,** 99 102 (1992).

[116] Rene Berger, Jean-Claude Bissey, Janis Klaiva and Benoit Soulard, *J. Mag. Mag. Mat.* **167,** 129-135 (1997).

Chapter 2

Experimental Techniques

The details of the material synthesis method and characterization techniques are presented in this chapter.

2.1 Preparation of the glass samples:

All the studied six series of glass samples are prepared by conventional melt quenching technique. The appropriate amounts of high purity (99.99) of oxides were initially taken into agate mortar and were properly grinned for two hours. Thoroughly grinned composition then annealed up to 400^0C for one hour and then grinned for four to six hours. The properly grinned powder was taken into a platinum crucible and kept for melting in the furnace in air up to 900^0C.

The melt was agitated, for homogenization, by gently shaking the crucible. After 30 minutes in the molten state, the crucible was removed and the contents quickly transferred on to a copper plate at room temperature and pressed by another copper plate. We obtain thin, smooth, black reflecting glass samples. The loss of tellurium oxide during melting was compensated by adding 10% extra tellurium oxide at the initial mixing stage.

2.1.1 Composition of the synthesized glasses

The prepared glass series are shown below:

1. $(100\text{-}x)TeO_2 - xCuO$, where x = 10, 20, 30, 40 and 50.
2. $(20\text{-}x)\ ZnO - 80TeO_2 - xFe_2O_3$, where x = 0, 5, 10, 15 and 20.
3. $20ZnO - (80\text{-}x)\ TeO_2 - xFe_2O_3$, where x = 0, 1, 3, 5 and 7.
4. $10Fe_2O_3 - (90\text{-}x)\ TeO_2 - x\ Bi_2O_3$, where x = 0, 5, 10, 15 and 20.
5. $20Fe_2O_3 - (80\text{-}x)TeO_2 - x\ Bi_2O_3$, where x = 0, 5, 10, 15 and 20.
6. $(100\text{-}x)\ (70Bi_2O_3\ 20ZnO\ 10\ PbO) - xFe_2O_3$, where x = 0, 5, 10, 15, 20 and 25.

All the glass samples are coded as listed in the table 2.1.

Table 2.1. Composition and codes for the series of glass samples

Composition	***x mol% (Code)***				
(100-x)TeO_2 xCuO	10 (T9C1)	20 (T8C2)	30 (T7C3)	40 (T6C4)	50 (T5C5)
(20-x) ZnO 80TeO_2 xFe_2O_3	0 (20Z80T)	5 (15Z80T5F)	10 (10Z80T10F)	15 (5Z80T15F)	20 (80T20F)
20ZnO (80-x) TeO_2 xFe_2O_3	0 (20Z79T)	1 (20Z79T1F)	3 (20Z77T3F)	5 (20Z75T5F)	7 (20Z73T7F)
10Fe_2O_3 (90-x) TeO_2 x Bi_2O_3	0 (10F90T)	5 (10F85T5B)	10 (10F80T10B)	15 (10F75T15B)	20 (10F70T20B)
20Fe_2O_3 (80-x)TeO_2 x Bi_2O_3	0 (20F80T)	5 (20F75T5B)	10 (20F70T10B)	15 (20F65T15B)	20 (20F60T20B)
(100-x) (70Bi_2O_3 20ZnO 10 PbO) xFe_2O_3	0 (BZPF0)	5 (BZPF5)	10 (BZPF10)	15 (BZPF15)	20 (BZPF20)	25 (BZPF25)

2.2 Characterization Techniques and Material Properties Measurements

The synthesized samples are characterized by X-ray Diffraction (XRD) and Fourier transform Infrared spectroscopy (FTIR). Differential Scanning Calorimeter (DSC), Electron Spin Resonance (ESR) and Vibrating Sample Magnetometer (VSM) are also used to study the properties of the samples. For structural analysis, XRD and IR studies were done. To understand the thermal properties of the amorphous samples, DSC studies were done. To understand the magnetic nature and local structure of the samples ESR and VSM studies were done. The following sections describe the working principle of the experimental techniques.

2.2.1 X-ray Diffractometer (XRD)

X-rays are electromagnetic radiation with typical photon energies in the range of 100 eV - 100 keV. X-rays of short wavelength in the range of a few angstroms to 0.1 angstrom (1 keV - 120 keV), also called hard x-rays, and are used for diffraction studies. A diffraction pattern is observed only when Bragg's law is satisfied. The Bragg equation for diffraction that works for basic calculations is given by:

$$2d\sin\theta = n\lambda \tag{2.1}$$

where *n* is an integer, λ is the wavelength of the X-ray, *d* is the interplanar spacing in the crystalline material and θ is the angle between the incident beam and lattice plane diffracted angle. The maximum intensity of 2θ, which is called the Bragg angle, is the angle between incident and scattered beam. A schematic diagram is shown in figure 2.1.

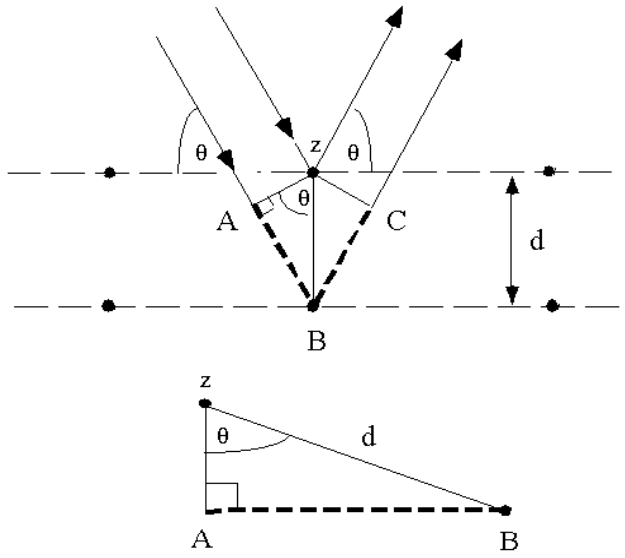

Fig 2.1. Schematic diagram of the Bragg's Law.

Consider two parallel waves of the incident beam which are always in phase. The first beam strikes the top layer at atom z. The second beam continues to the next layer and gets scattered by atom B. The second beam must travel the extra distance AB + BC. The diffracted beam will be observed in the direction for which this extra distance is an integer (n) multiple of the wavelength λ i.e. $n\lambda = AB + BC$, which satisfies the condition of constructive interference. From the triangle $AB = d\sin\theta$ and as AB = BC, $n\lambda = 2AB = 2d\sin\theta$, which is the Braggs law.

The XRD patterns of the samples were recorded using a PHILIPS X–ray diffractometer. Cu K_α X-radiation is used as the X-ray source which has a characteristic wavelength of 1.5418A^o and which operates at 40kV and 30mA. X – rays filters, monochromators, detectors like lithium drifted silicon etc. can be used to obtain monochromatic high intensity x-rays. A Ni filter is used to filter the CuK_α radiation.

During diffraction the intensity of undesirable components are also eliminated through filters [1]. The XRD patterns are recorded in the range 10-80^o, with the step size of 0.02^o, and at the rate of 1^o per minute. The data is collected using a counter proportional detector.

The amorphous nature of the materials synthesized is confirmed if there are no sharp peaks in xrd spectra. For glasses, XRD spectra are poor in intensity and broad peaks are obtained.

2.2.2. FT-IR studies:

Infrared spectroscopy is the spectroscopy that deals with the infrared region of the electromagnetic spectrum, which is light with a longer wavelength and lower frequency than visible light. It covers a range of techniques, mostly based on absorption spectroscopy. As with all spectroscopic techniques, it can be used to identify and study chemicals. A common laboratory instrument that uses this technique is a Fourier transform infrared (FTIR) spectrometer.

The infrared portion of the electromagnetic spectrum is usually divided into three regions. The near-, mid- and far-infrared, named for their relation to the visible spectrum. The higher-energy near-IR, approximately 14000-4000cm^{-1} (0.8-2.5μm wavelength) can excite overtone or harmonic vibrations. The mid-infrared, approximately 4000-400cm^{-1} (2.5-25μm) may be used to study the fundamental vibrations and associated rotational-vibrational structure. The far-infrared, approximately 400-10cm^{-1} (25-1000μm), lying adjacent to the microwave region, has low energy and may be used for rotational spectroscopy.

The infrared spectrum of a sample is recorded by passing a beam of infrared light through the sample. When the frequency of the IR is the same as the vibrational frequency of a bond, absorption occurs. Examination of the transmitted light reveals how much energy was absorbed at each frequency (or wavelength). This can be achieved by scanning the wavelength range using a monochromater. Alternatively, the whole wavelength range is measured at once using a Fourier transform instrument and then a transmittance or absorbance spectrum is generated using a dedicated procedure. Analysis of the position, shape and intensity of peaks in this spectrum reveals details about the

molecular structure of the sample. This technique works almost exclusively on samples with covalent bonds. Simple spectra are obtained from samples with few IR active bonds and high levels of purity. More complex molecular structure leads to more absorption bands and more complex spectra.

The essential components of an IR spectrometer are the source of IR radiation, a detector and a recorder. When the energy of the radiation transmitted by a reference and the sample is the same, the detector does not produce any signal. When the sample absorbs radiation and results in an inequality in the transmitted beams, a resultant pulsating signal is produced with frequency equal to the frequency of the IR radiation. The recorder records such signals as the whole spectrum is scanned.

The JASCO FTIR-5300 spectrometer was used for the present studies as the Fourier transform method enables a large sampling and a better resolution. This is a transmission spectrometer and scans the IR region between 4000 to 400cm^{-1}.

2.2.3 Differential Scanning Calorimetry (DSC):

Differential Scanning Calorimetry is the technique of measuring the heat effects associated with physical or chemical changes that take place as a substance is heated at a uniform rate. Heat changes either exothermic or endothermic are caused by phase transitions, such as fusion, boiling, sublimation, dehydration, crystallization etc. The term DSC was apparently first used by Watson et al [2]. DSC is a technique to study the thermal transition or phase transition involving nucleation, growth of micro-crystallites and the study of crystallization kinetics [3-9]. It also provides information about the change in enthalpy as a function of temperature [7-9]. This technique provides a rapid and precise determination of a crystallization process and an associated kinetic parameter. It allows a continuous record of thermal evolution of the system as a function of time or temperature. Crystallization kinetics can be studied both non-isothermally as well as isothermally.

In non-isothermal case the sample is scanned with temperature at constant heating rate and in isothermal case the sample is kept at fixed temperature and the change in its enthalpy is observed as a function of time. Isothermal method is more definite and rigorous, while non-isothermal method is more convenient [8]. Non-isothermal method

can be performed over a wider temperature range and many phase transitions occur rapidly in this method [8]. This technique is highly sensitive, accurate and versatile in measuring the heat effect associated with physical and chemical changes that take place when the substance is heated at a uniform rate.

Non-isothermal DSC technique:

In this technique we measure the difference in input energies of a sample material and reference material, which is controlled by the temperature electronic program. In the non-isothermal DSC technique the sample and the reference material are kept isothermally as they are heated or cooled. Heat changes either exothermic or endothermic are recorded as heat flow (dH/dt) in W/g(mcal/g) as a function of temperature under non-isothermal conditions whereas, in isothermal conditions, the sample and reference are kept at a constant temperature and DSC thermogram is recorded as a function of time.

A non-isothermal thermogram is shown in figure 2.2

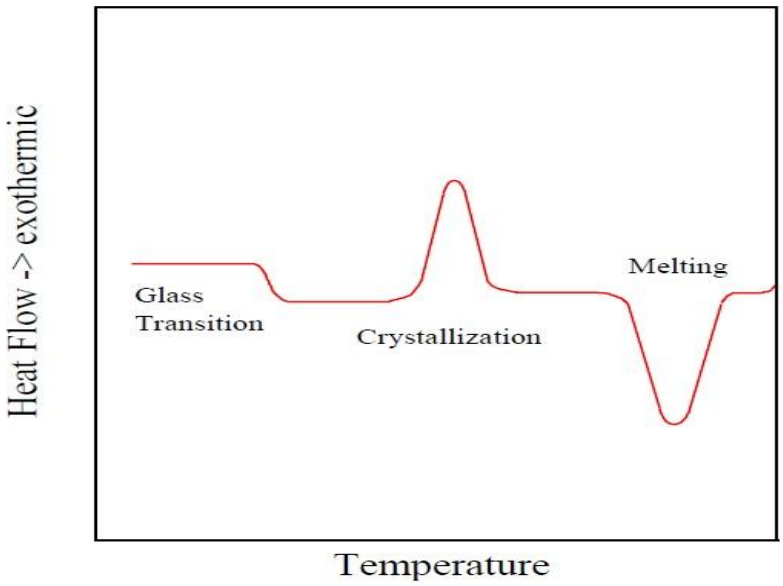

Fig 2.2Schematic diagram of a non-isothermal thermogram

When we start heating the two pans, initially there comes a straight line called the baseline due to the difference in heat output of the two heaters against temperature. So, when certain amount of heat is given to the sample, its temperature goes up by some amount, and the amount of heat it takes to get a certain temperature increase is called the

heat capacity or C_p. We get the heat capacity by dividing the heat supplied by the resulting temperature increase.

As we heat further, after certain temperature, the plot will shift upward suddenly increasing the heat flow resulting in the increase in heat capacity. At this temperature T_g called glass transition temperature the phase transition starts. The glass is no more glass after T_g. The glass transition temperature does not occur suddenly but takes place over a temperature range.

Above the glass transition, the glass has a lot of mobility as it has gained enough energy and at an appropriate temperature, it will gain enough energy to move in very ordered arrangement, which we call 'crystal'. When glass falls into these crystalline arrangements, it gives off heat. The drop in the heat flow is shown as a big dip. The area under the curve measures the latent heat of crystallization. The temperature at the lowest point of the dip is called crystallization temperature T_c. This dip tells us that glass can crystallize after heating. As the glass gives off heat when it crystallizes, we call crystallization, an exothermic transition.

If we still keep heating we reach another thermal transition called melting. The ordered arrangements become disordered and begin to move around freely. When the glass crystal melts, they must absorb heat. This is first order transition. This means that when the melting temperature is reached, the crystal temperature won't rise until the crystals have melted. The latent heat of melting is measured by measuring area of the peak.

Description of the setup:

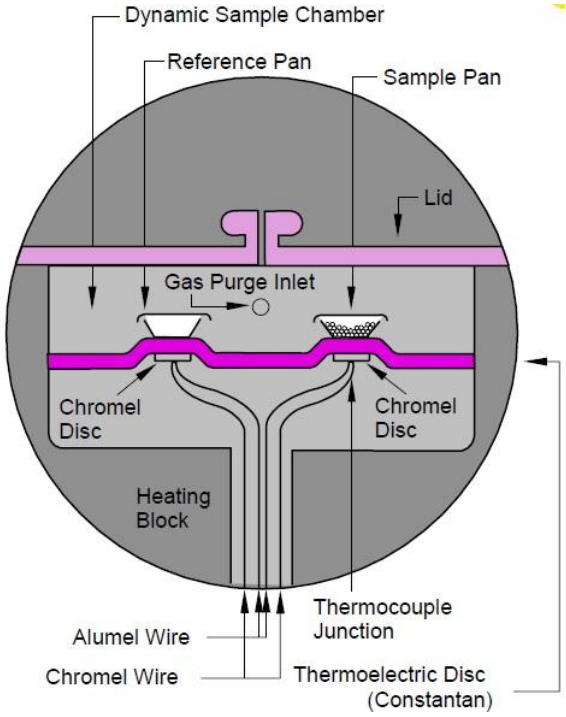

Fig 2.3 schematic diagram of the DSC cell

Differential Scanning Calorimetry measurements have been done using TA instrument DSC 2010. The schematic diagram of the DSC cell is shown in fig.2.3. The DSC cell uses a constantan (thermoelectric) disc as a primary heat transfer element. A silver-heating block, capped with a vented silver lid encloses the constantan disc. The selected sample and an inert reference are placed in generally aluminum/copper pans that sit on raised portion of the disc. Heat is transferred through the constantan disc to both the sample and the reference pan. Differential heat flow to the sample and reference are monitored by the chromel constantan area thermocouples formed at the junctions of the constantan disc and chromel wafers weld to the underside of the two raised portions of the disc. Chromel and alumel wires are connected to the chromel wafers at the thermocouple junctions to measure sample temperature. The alumel wire welded to the reference wafer is for thermal balance. Purge gas is preheated to heating block temperature by circulation within the block before entering the sample chamber through the purge gas inlet. Gas exits through the vent hole in the silver lid.

Vacuum and a cooling port in the 2010 instrument leads to openings in the cell but not directly to the sample chamber. A bell jar placed over the cell and sealed with an o-ring, protects the operator from evolved gases and permits cell evacuation.

Constant calorimetric sensitivity is maintained by electronic linearization of the cell calibration coefficient. Minor complications arise mostly because the sample holders may not be strictly identical and a temperature gradient may develop across the finite thermal resistance between the sample and sample holder etc.

We also used another DSC instrument Model METTLER DSC for recording non-isothermal thermograms of the glass samples.

Experimental procedure of DSC:

The crystallization studies of glasses were carried out by using DSC instrument. In the DSC measurements about 4-6 mg of sample is placed in an aluminum cup and weighed using digital microbalance. The sample is then covered by an aluminum cup and standard crimper is used to crimp the cover on to the sample. The calorimeter is already calibrated by a pure indium as a standard material under non-isothermal condition. Now the sample is kept on the holder and samples are continuously heated from room temperature (RT) to the required high temperature, by non-isothermal method. The temperature range was RT to 550^0C. The scanning rates ranging from 5^0c/min. to 15^0c/min. were used. The data is analyzed using Kissinger's model of crystallization.

The heat evolved is recorded as a function of temperature. In general, oxide glasses may have more than one crystallization temperature. In DSC thermograms each peak is characterized by a peak temperature T_p. The glass transition, onset and peak temperature of crystallization are obtained using the software "standard data analysis". $\Delta T=T_0-T_p$, resistance to crystallization or thermal stability was calculated for all samples.

2.2.4 Electron Spin Resonance (ESR):

Electron spin resonance (ESR) spectroscopy deals with the interaction of electromagnetic radiation with the intrinsic magnetic moment of electrons arising from their spin. A material which does not have a net magnetic moment may acquire one when placed in an external magnetic field. This results in an internal magnetic field in the

material, which is different from the external applied magnetic field. Because an electron has an intrinsic spin and magnetic moment, it may be used as a probe of local magnetic fields on an atomic scale, which forms the basis of ESR. Important information about the physics of the material may be obtained by probing the internal field.

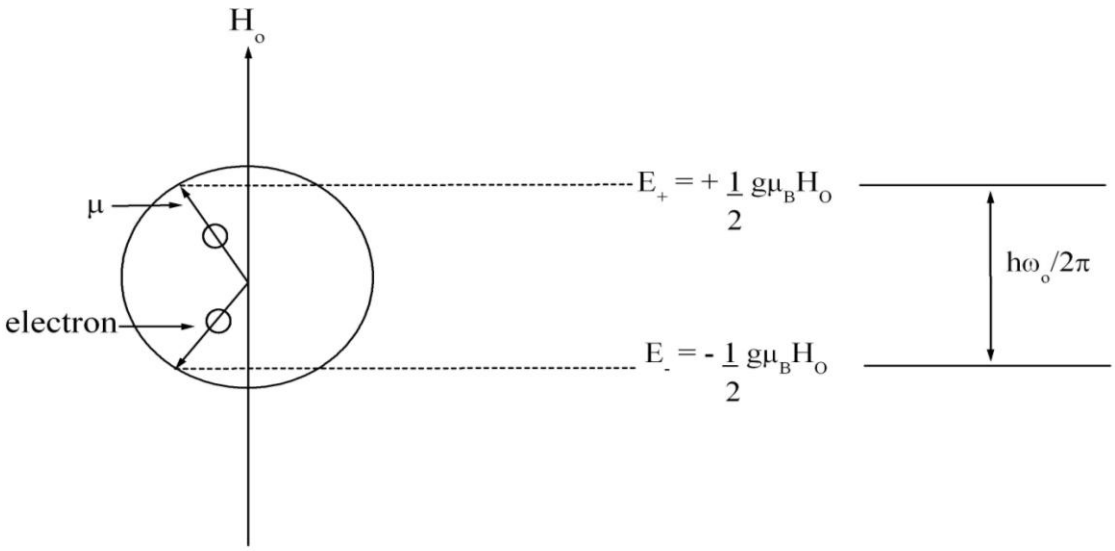

Fig 2.4 Schematic representation of a single electron spin in a steady magnetic field H_o

According to quantum theory an electron has a spin which is understood as an angular momentum. This leads to a magnetic moment. Consequently, the negative charge that the electron carries is also spinning and constitutes a circulating electric current. The circulating current induces a magnetic moment μ_s. If the electron is subjected to a steady magnetic field $H_o \| z$, the magnetic moment μ_s causes the electron to experience a torque tending to align the magnetic moment with the field. The relation between the magnetic moment and the spin vector is

$$\mu_S = \frac{2\pi g \mu_B}{h} S \qquad (2.2)$$

where μ_B is the Bohr magneton and g is the Lande factor. The value of μ_B is given as $\mu_B = \frac{eh}{2\pi m}$ and has a value of 9.274 x 10^{-24}JT^{-1} and the value of g for a free electron is 2.0023. The g-factor gives information about a paramagnetic centre's electronic structure. The energy of the system is determined by the projection of the spin vector along the applied field H_o which is along the z-axis. According to the quantum theory only two

values are permitted for an electron namely $S_z = \pm -\frac{h}{4\pi}$. The magnetic moment of the electron can hence assume only two projections onto the applied magnetic field. The degeneracy of the electron placed in a magnetic field is lifted as shown in the figure 2.4.

Hence the two values of energy are given as:

$$E_{\pm} = \pm \tfrac{1}{2} g\mu_B H_O \qquad (2.3)$$

when the applied electromagnetic radiation is at a frequency that corresponds to the separation between the permitted energies levels, the difference in energy levels is equal to

$$\Delta E = E_{+} - E_{-} = g\mu_B H_o = \frac{h\omega_o}{2\pi} = h\nu \qquad (2.4)$$

When the equation 2.4 is obeyed energy is absorbed which leads to resonance. This is the basic theory of ESR [10, 11].

Figure 2.5 gives a pictorial idea of the ESR. The test sample which is placed in a uniform magnetic field is wrapped within a coil which is connected to an RF oscillator. The smaller magnetic field induced in the coil by the oscillations of the oscillator is at right angles to the uniform magnetic field. Consider a single electron within the test sample. It will have a magnetic dipole moment (μ_s) that is related to its intrinsic angular momentum, or spin, by the vector equation

$$\mu_S = \frac{2\pi g_S \mu_B S}{h} \qquad (2.5)$$

where g_s is the electron spin factor and *S* is the magnitude of the spin angular momentum of the electron. Associated with the electron there are other magnetic moments coming from the orbital angular momentum given by the equation

$$\mu_L = \frac{2\pi g_L \mu_B L}{h} \qquad (2.6)$$

where μ_L is the total magnetic moment resulting from the orbital angular momentum of an electron, L is the magnitude of its orbital angular momentum and total angular momentum is obtained from the equation

$$\mu = \frac{2\pi g_J \mu_B J}{h} \tag{2.7}$$

where $\boldsymbol{\mu}$ is the total magnetic moment resulting from both spin and orbital angular momentum of an electron, $\boldsymbol{J} = \boldsymbol{L}+\boldsymbol{S}$ is its total angular momentum. The magnetic dipole moment of the electron and the uniform magnetic field interact with each other. Due to its quantum nature, the electron can orient itself in one of only two ways, with the value of energy as given in equation 2.3. When the RF oscillator is tuned to a frequency ν and the

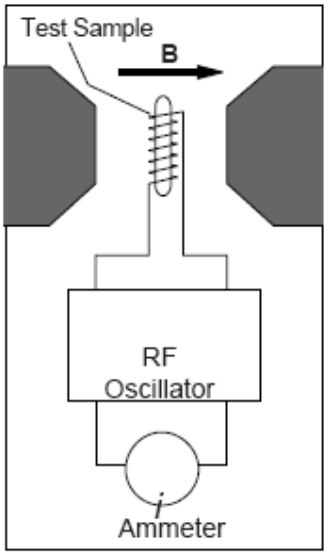

Fig 2.5 Depiction of the mounted samples in an ESR Spectrometer

energy of the irradiated photons, hν, is equal to the difference between the two possible energy states of the electron, resonance occurs. The absorption of energy affects the permeability of the test sample, which affects the inductance of the coil and thereby the oscillations of the RF oscillator. The result is an observable change in the current flowing through the oscillator. The condition for resonance, therefore, is that the energy of the

photons emitted by the oscillator match the energy difference between the spin states of the electrons in the test sample which is mathematically stated in equation 2.4.

The temperature dependent ESR spectra of the samples were recorded on a JEOL JES-FA SERIES X-Band ESR spectrometer. A compressor is used to supply a continuous column of hot air through a hot heat blast pipe attached to the dewar adapter through which the gas flows, for the high temperature measurements in the temperature range 330K – 473K (±0.5 K). A continuous gas-flow cryostat for liquid nitrogen is used for the low temperature measurements in the temperature range 100K – 330K (±0.5 K). The electromagnet used has a low impedance, water cooled main coil which gives a magnetic field homogeneity of ± 5μT

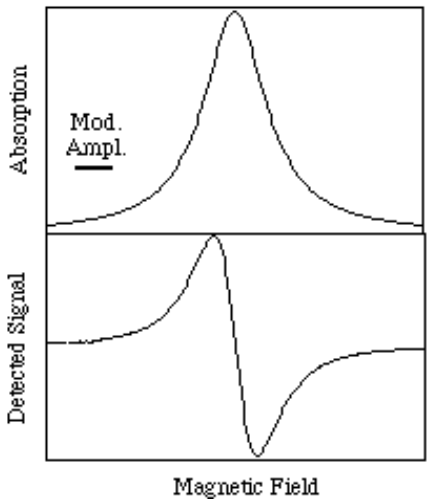

Fig 2.6 Absorption curve (above) and corresponding first derivative detected signal (below)

Taking first-derivative spectra has a much better apparent resolution than the absorption spectra. Indeed, second-derivative spectra are even better resolved (though the signal-to-noise ratio decreases on further differentiation). The instrument is operated at a frequency of ~ 9GHz. The cavity resonator is used in the TE mode. Small shining edge bulk glass pieces weighing a few milligrams are mounted in quartz tubes of diameter 5mm and length 270mm under optimized conditions of modulation amplitude, receiver gain, time- constant and scan time. The instrument is interfaced with a computer and data was obtained for more detailed analysis. The dc magnetic field is ramped to 800mT and the ESR spectra for the samples are recorded.

The ESR spectrum recorded is the first derivative of spectral trace as shown in figure 2.6, as it has advantages over recording the direct signal. It indicates the centre of the broad resonance peak more precisely than the direct signal and the width of the peak (taken as half width) is often more accurately measured from the derivative curve [12].

2.2.5 Magnetization Measurements:

The magnetization studies on the materials were performed using a vibrating sample magnetometer (VSM). The M-H and M-T plots give information about the magnetic properties of the materials.

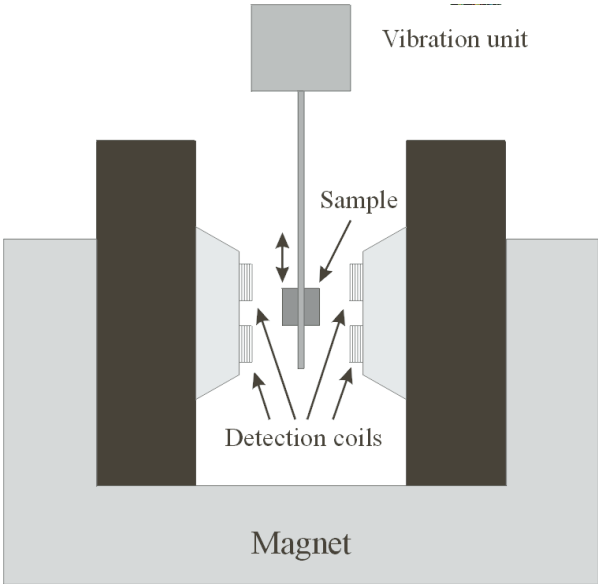

Fig 2.7. A Schematic diagram of a VSM

Apart from this basic measurement performed to obtain the hysteresis loops, the M-H curves or measuring the magnetic moment of materials, variation of magnetization with temperature gives more information. Modern day VSMs have the versatility to be used for different magnetic studies like the temperature dependent magnetization studies, magnetoresistance measurements of bulk as well as thin film samples as a function of temperature, field and angle measurements of magnetization in the X and Y directions simultaneously using vector measurements. Using an add-on facility of a torque system the VSM can be used as a torque magnetometer to measure magnetic anisotropies, rotational hysteresis, and anisotropy field distributions.

The Vibrating Sample Magnetometer (figure 2.7) works on the basic principle of Faraday's Law of magnetic induction. When a sample is placed in a uniform magnetic field, a dipole moment proportional to the product of the sample susceptibility and the applied field is induced in the sample. The sample holder placed at the tip of a long slender vertical rod, is connected to a vibration unit. This is a transducer assembly which is placed above the magnet. This is the vibration unit, which vibrates the sample centered in between the pole pieces. The sample undergoing sinusoidal motion as well as induces an electric signal in suitably located stationary pick-up coils. This signal, which is at the vibration frequency, is proportional to the magnetic moment, vibration amplitude and the vibration frequency.

A vibrating capacitor is located below the transducer. This generates an AC control signal which varies with the vibration amplitude and frequency. The signal is fed back to the oscillator where it is compared with the drive signal to maintain constant output drive signal. It is also phase adjusted and routed to a signal demodulator where it functions as the reference drive signal. A signal from the sample is developed in the pickup coils, buffered, amplified and applied to the demodulator where it is synchronously demodulated with respect to the reference signal derived from the moving capacitor assembly. The resulting DC output is an analog of the moment magnitude alone, uninfluenced by the vibration amplitude changes and frequency drift.

The room temperature magnetization experiment was carried out on a Lakeshore 7400 series VSM, Model 7407. The sensitivity of the instrument is high enough to measure magnetic moments ranging from 5μemu to 10^3emu. The gauss meter is used in the transverse probe mode. The water cooled electromagnet has maximum field strength of ±10kG in a 2 inch air gap with a 6-inch pole face or ±21kG in a 0.9-inch air gap with a 3-inch pole face, having a field accuracy of 1%.

PPMS (Physical Properties Measurement System) also used to understand the magnetic behavior of the sample at low temperatures.

References

[1] B.D. Culity, *Elements of X-ray Diffraction, (Addison- Wesley Publishing Company Inc*. (1978).

[2] Watson. *Anal. Chemistry*, **36**, 1233 (1964).

[3] T. Komatsu, R. Sato, K. Imai, K. Matusita & T. Yamashita, *Jpn. Jr. Appl. Phys*. **27**, 550 (1988).

[4] E.M. Gyorgr, Metallic glasses edited by J.J. Gilman and H.J. Leans, *American Society of Metals, USA*.

[5] R. Singh, *Jr. Physics D: Appl.Phys*, **20** 548 (1987).

[6] Kazumasa Matusita & Sumio Sakka, *Jr. of Non-Cryst. Solids*, **38 & 39** (1980).

[7] Kazumasa Matusita, Takayuki Komatsu, Ryosuse Yokota, *Jr. of Mater. Science*, **19**, 291 (1984).

[8] Haixing Zheng & J.D. Mackenzie, *Phy. Rev. B*, **43**, 3048 (1991).

[9] Milenko & Mileno V. Susicj, *Mater. Sci. Letters*, **5**, 1251 (1986).

[10] John E. Wertz, James R. Bolton, *Mc Graw Hill Co. ESR Elementary Theory and Applications* (1972).

[11] A. Abragam and B. Bleaney *Electron Paramagnetic Resonance of Transition Ions, (Clarendon Press, Oxford)* (1970).

[12] Colin N. Banwell and Elaine M. Mc cash, *Fundamentals of Molecular Spectroscopy, (Tata Mc Graw - Hills Publishing Company Limited)* (1997).

Chapter 3

XRD, IR and DSC Studies

This chapter describes X-Ray Diffraction (XRD), Infrared Spectroscopic (IR) and Differential Scanning Calorimetric (DSC) studies carried out on various synthesized series of glass samples as mentioned in chapter 2.

3.1. XRD STUDIES

To confirm the amorphous nature of the glass samples, XRD studies were carried out on the synthesised samples using PHILLIPS XRD diffractometer, with Cu-Kα radiation with λ=1.5418A^0. The XRD plots for various samples are shown in figures 3.1.1 to 3.1.6.

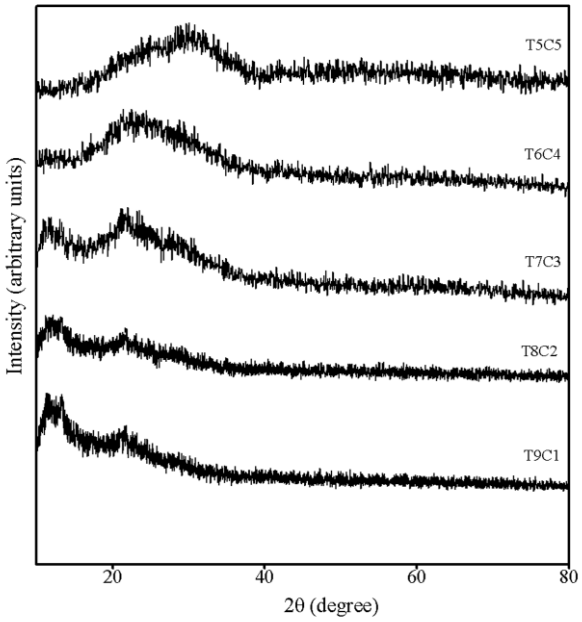

Fig 3.1.1. XRD pattern for the glass system (100-x)TeO_2 – xCuO, where x = 10, 20, 30, 40 and 50

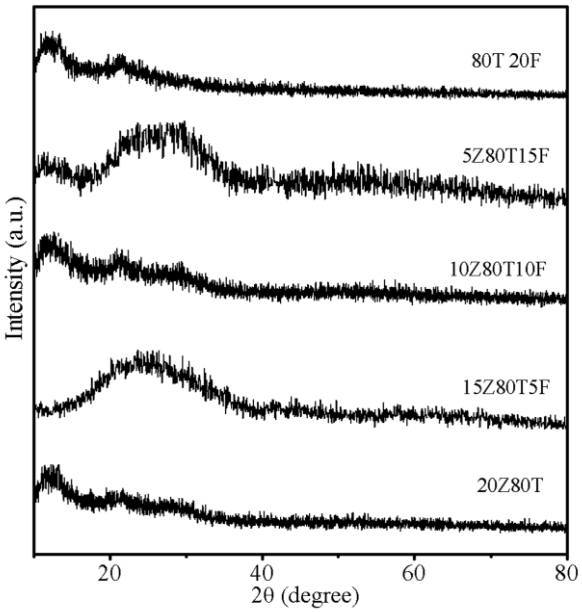

Fig 3.1.2. XRD pattern for the glass system (20-x) ZnO - 80TeO_2 – xFe_2O_3, where x = 0, 5, 10, 15 and 20

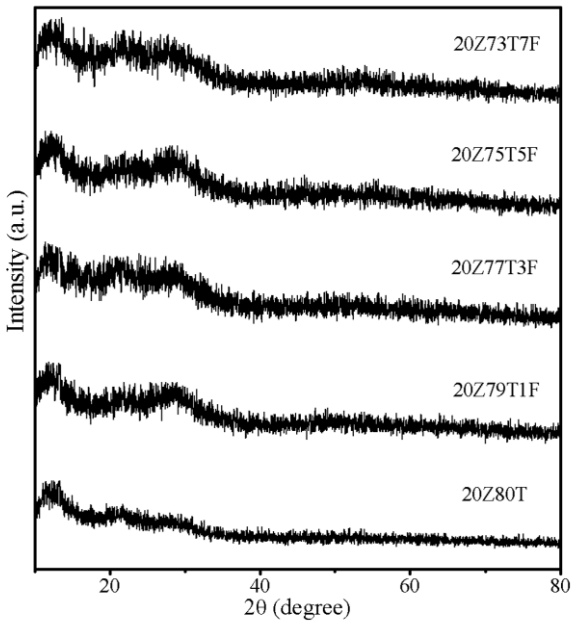

Fig 3.1.3. XRD pattern for the glass system 20ZnO- (80-x) TeO_2- xFe_2O_3, where x = 0, 1, 3,5and7

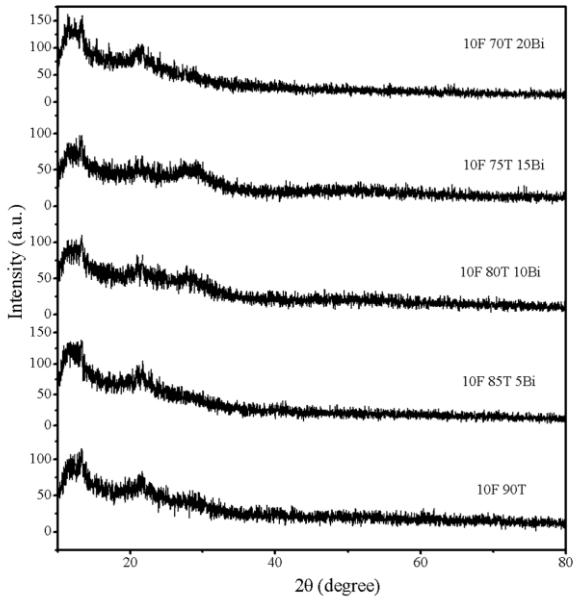

Fig 3.1.4. XRD pattern for the glass system $10Fe_2O_3$ – (90-x) TeO_2 –x Bi_2O_3, where x = 0, 5, 10, 15 and 20

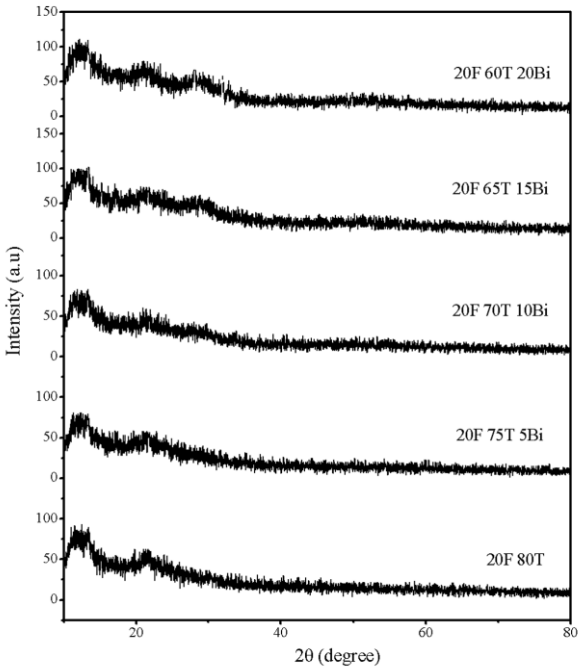

Fig 3.1.5. XRD pattern for the glass system $20Fe_2O_3$ - (80-x)TeO_2 –x Bi_2O_3, where x = 0, 5, 10, 15, 20 and 25

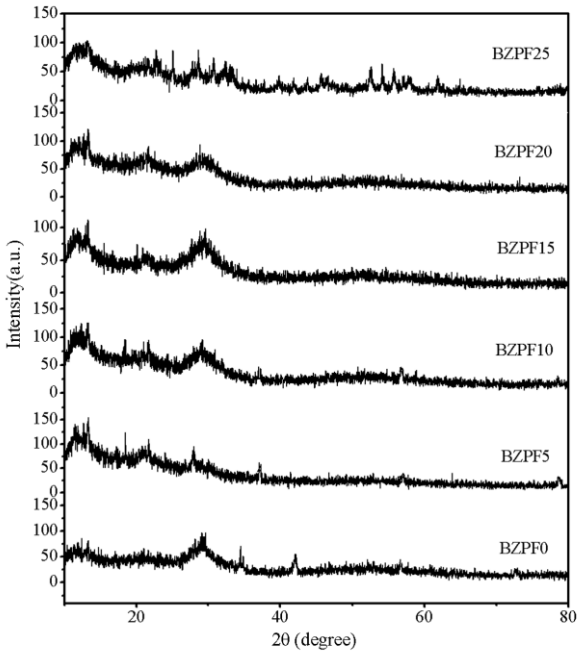

Fig 3.1.6. XRD pattern for the glass system (100-x) (70Bi_2O_3 20ZnO 10 PbO) – xFe_2O_3, where x = 0, 5, 10, 15, 20 and 25

All the glass samples except some samples in BZPF series show no sharp peaks in the xrd patterns confirming amorphous nature of these samples. The peaks observed in xrd plots of some samples of BZPF series may be due to some crystalline phase formed in these samples, namely: Bismuth ferrite ($BiFeO_3$) with rhombohedral phase [JCPDF card no: 86-1518] in BZPF5, BZPF10 and BZPF25 samples, a minor crystalline phase of bismuth zinc oxide [JCPDF card no: 78-2374] in BZPF0, BZPF5 and BZPF10 samples.
In conclusion, the XRD patterns of the synthesized glass samples show no sharp peaks but only broad bands characteristic of amorphous nature of the synthesised samples.

3.2. IR STUDIES:

To understand the change in structure as a function of composition, the IR studies of the synthesized glasses were undertaken. The infrared transmittance spectra of the glasses were recorded using standard KBr pellets method on a JASCO FT/IR-5300 spectrometer in the 400-1000 cm^{-1} wavelength range.

According to an assumption in vibrational spectroscopy of the solid-state [1, 2], the vibrations of a specific group of atoms in a lattice may be regarded as relatively independent of motions of the rest of the atoms.

The extensive IR studies on various tellurite glass systems have been reported [3-11].

The observed absorption bands and shoulders are assigned as follows:

1. The structural units in tellurite containing glasses are TeO_4 trigonal bipyramids (tbp) and TeO_3 trigonal pyramids (tp). The bands at 600-640cm^{-1} and 680-700cm^{-1} are for TeO_4 tbp and TeO_3 tp respectively. The shoulder at 765cm^{-1} and the broad bands at 655cm^{-1} are due to the distribution of the TeO_4 tetrahedra. The maximum at 640 to 635 cm^{-1} and a shoulder at about 670 to 660 cm^{-1} are characteristic of deformed TeO_4 groups.
2. The presence of an intense maximum at 670 to 665cm^{-1} and a shoulder at 625 to 620 cm^{-1} is due to elementary structurally symmetrical TeO_4 polyhedron.
3. Symmetrical TeO_3 groups are characterized by an intense band in 680 to 665 cm^{-1} range. With the introduction of other oxides in the tellurite glass, the new structural arrangement on the back side of the four coordinated tellurium ions favours the stronger polarizability of the free electron pair in certain directions.

   As a result, part of the TeO_4 groups are transformed into TeO_3 groups.

Following table summarises the results of the previous IR studies and the assignment of functional group in tellurite glasses.

Table 3.2.1. The assignment of IR absorption bands observed in tellurite glasses

Wavenumber (cm^{-1})	Assignment
830	Stretching vibrational mode of TeO_3 tp with NBO
770	Vibration of continuous TeO_3 tp
690	Stretching vibrational mode of TeO_3 tp with bridgning oxygen
660	TeO_4 groups are preserved together with TeO_3 groups
620	Stretching vibrational mode of TeO_4 tp with bridgning oxygen

700-670	Symmetrical TeO_3 groups
Shoulder in the range 640-630 cm^{-1}	Decrease in symmetry of the TeO_3 groups
Maximum at 670cm^{-1} and a shoulder at 635 cm^{-1}	Symmetric TeO_4 goups
Maximum at 640-635 cm^{-1} and a shoulder at about 670cm^{-1}	Deformed TeO_4 groups
565	Te-O bond vibrations with oxygen as non-bridging (NBO)
470	Te-O-M stretching vibrations (here M is transition metal)
Bands in the range 300-500 cm^{-1}	Belong to deformations.
Shoulder at 765 cm^{-1} and the broad bands at 655cm^{-1}	Distribution of TeO_4 tetrahedra
Bands at 790, 720, 660 and 600 cm^{-1}	TeO_2 groups

3.2.1. (100-x)TeO_2 – xCuO glass system:

Figure 3.2.1 shows the IR absorption spectra of xCuO-(1-x)TeO_2 glasses. The glasses exhibit broad bands within the range of 550 to 850cm^{-1}. The main absorption bands are assigned to stretching vibrations of the Te-O bonds. The positions of absorption bands observed are 765, 720, 670, 640, 610, 520, 480 and 440 cm^{-1}. The shoulder at 765cm^{-1} is due to the distribution of the TeO_4 tetrahedra. The band at 720 represents the presence of TeO_2 groups. The band at 670, is assigned to symmetrical TeO_3 units. Whereas bands at 640 and 610 cm^{-1} correspond to symmetrical TeO_4 and TeO_3 units. The copper ions are likely to form covalent Te-O-Cu bonds which appear at 470cm^{-1}.

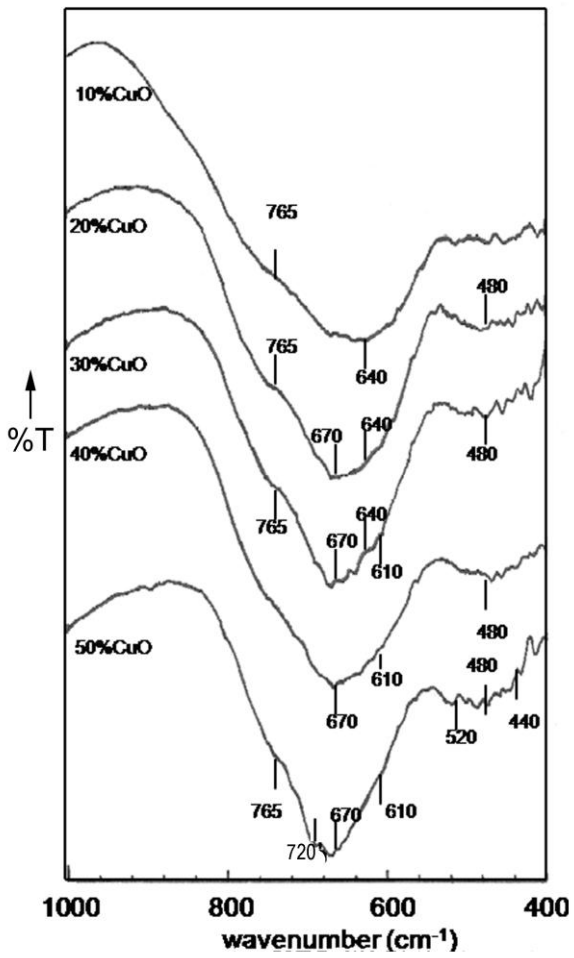

Fig 3.2.1 IR absorption spectra of xCuo-(1-x)TeO_2

The IR vibration bands of tellurite units are found to shift to higher wave number with partial replacement of TeO_2 by CuO. When TeO_2 content is high, the glass structure has relatively large number of TeO_4 units and very few number of TeO_3 units. As TeO_2 is replaced by CuO content, the bands are broadening and reduction in intensity proving increase in the disorder. The disorder in the glass network increases with the increase in CuO content. TeO_2-rich glasses are characterized by TeO_4 building units. Both Te-O_{ax} axial bonds in theTeO_4 polyhedra are strongly dynamic and easily attacked by the modifier. When a modifier oxide is introduced in the glass matrix, one of the Te-O_{ax} bonds in TeO_4 polyhedra undergoes elongation. The introduction of a modifier in the binary glass leads to a $TeO_4 \rightarrow TeO_{3+1}$ transition. The number of TeO_{3+1} units is limited by modifier addition. With increase in modifier content the TeO_{3+1} units transform into TeO_3 and TeO_2 units.

3.2.2. (20-x)ZnO-80TeO$_2$-xFe$_2$O$_3$ glass system:

The positions of absorption bands observed are 795, 771, 667, 640, 610, 560, 474 and 440 cm^{-1}. The positions of the bands and the assignments of the groups were as mentioned in the table 3.2.1. The shoulder at 470cm^{-1} is due to the formation of Te-O-Fe stretching vibrations. There is a fraction of the Fe cat ions which have partial covalent bonding and are incorporated in the network of these glasses. The shoulder at 565cm^{-1} is due to the Te-O-Fe bond vibrations, Fe is characterized by intermediate polarizing power. This groups has an intermediate amount of non-bridging oxygen (NBO)[3]. The broad absorption bands between 500 and 700cm^{-1} with a shoulder at 770-800cm^{-1} could be explained by states frozen in at a higher temperature with a large disorder, where a broad distribution of bond lengths occurs.

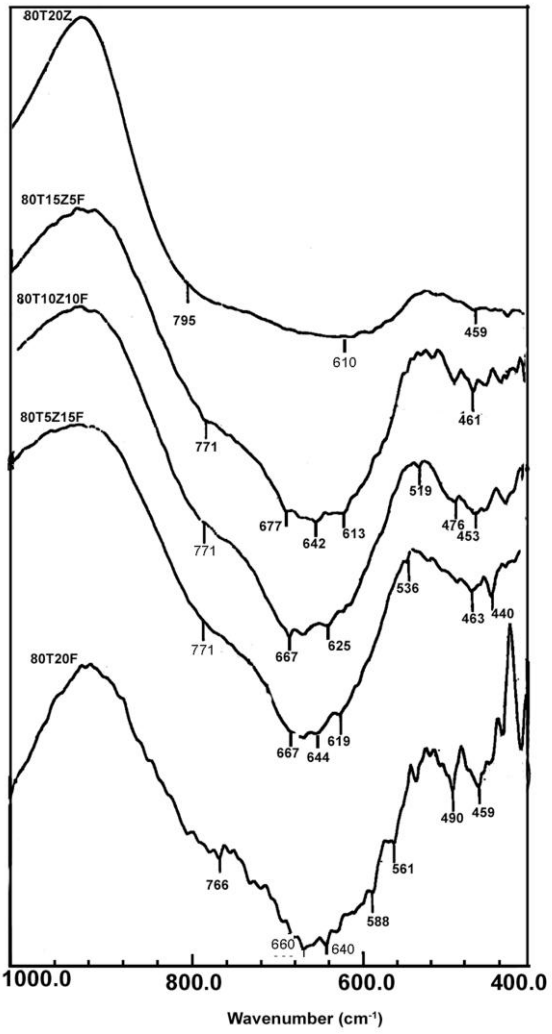

Fig 3.2.2 IR absorption spectra of (20-x)ZnO-80TeO$_2$-xFe$_2$O$_3$

TeO_2-rich glasses are characterized by TeO_4 building units in analogy to α-TeO_2. The influence of TeO_{3+1} structural groups increases with increasing ZnO. This leads to a typical deformation vibration in the region from 450-550cm^{-1} in the IR spectra [11]. The band in the range 550-580cm^{-1} is due to the vibration of the $Fe^{3+}O_6$ octahedral groups and the bands in the range 625-660cm^{-1} are due to the vibration of the $Fe^{3+}O_4$ complexes. With the increase in Fe_2O_3 content the bands at around 625cm^{-1} are shifted to higher wave number side (from 625 to 660cm^{-1}) and along with this shift its intensity is decreased. The band maximum at 580cm^{-1} is simultaneously shifted to lower wave number (i.e., from 580 to 550cm^{-1}) and its intensity increases. These changes of the IR spectra are probably caused by the transformation of part of the [FeO_4] tetrahedral into [FeO_6] groups [12]. The introduction of Fe_2O_3 in place of ZnO, the chain like structure TeO_{3+1} and TeO_4 groups will be disturbed and the ternary glasses lead to a $TeO_4 \rightarrow TeO_3$ transition. The disorder in the glass network increases with the increase of Fe_2O_3 content.

3.2.3. 20ZnO-(80-x)TeO_2-xFe_2O_3 glass system:

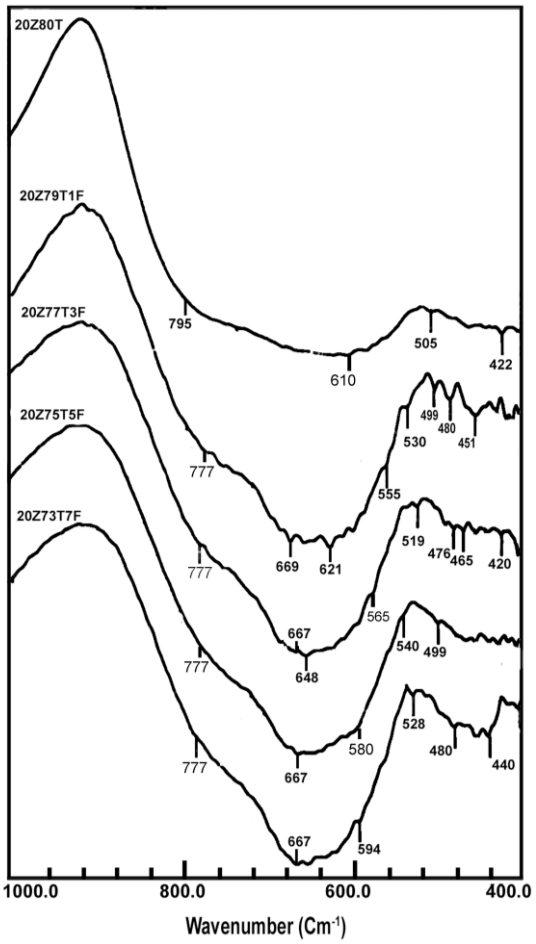

Fig 3.2.3 IR absorption spectra of 20ZnO-(80-x)TeO_2-xFe_2O_3

The observed absorption bands are at the positions 795, 777, 667, 621, 594, 540, 480 and 440 cm^{-1}. The positions of the bands and the assignments of the groups were as mentioned in the table 3.2.1. The absorption bands corresponding to iron group of atoms and the phenomenon of broadening of the bands are similar to that of earlier section.

3.2.4. $10Fe_2O_3 – (90\text{-}x)\ TeO_2 – x\ Bi_2O_3$ glass system:

The absorption bands are observed at the positions 777, 740, 670, 640, 470 and 440 cm^{-1}. The positions of the bands and the assignments of the groups were as mentioned in the table 3.2.1.

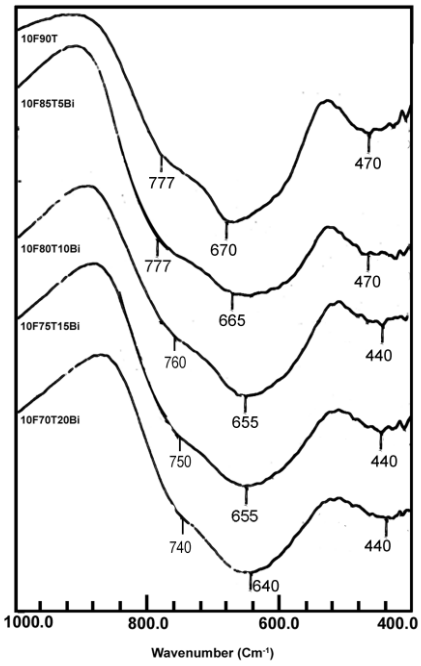

Fig 3.2.4 IR absorption spectra of $10Fe_2O_3 – (90\text{-}x)\ TeO_2 – x\ Bi_2O_3$

The shoulder at 470cm^{-1} is due to the formation of Te-O-Fe stretching vibrations. There is a fraction of the Fe cat ions which have partial covalent bonding and are incorporated in the network of these glasses. The broad absorption bands between 500 and 700cm^{-1} with a shoulder at 770-800cm^{-1} could be explained by states frozen in at a higher temperature with a large disorder, where a broad distribution of bond lengths occurs. The bands in the range 625-660cm^{-1} are due to the vibration of the $Fe^{3+}O_4$ complexes. Since iron mol% is not changing and with the increase of the Bi_2O_3 content

the intensity of these bands become too weak to detect. The bands at 448 cm^{-1} is due to the vibrations of Bi-O bonds in BiO_6 octahedral units [13-15].

The introduction of Bi_2O_3 in these glasses leads to give shoulder at 670 cm^{-1} with maximuk at 640 cm-1 represents the deformed TeO_4 groups. The disorder in the structure is increasing with the increase of Bi_2O_3 content. The IR vibration bands of tellurite units are found to shift to lower wave number with partial replacement of TeO_2 by Bi_2O_3. With the increase in the content of bismuth oxide, the formation of TeO_{3+1} groups are stimulated [5]. A similar tendency is evident in the present tellurite glasses. This change arises from the presence of accumulated TeO_3 groups and a decrease in the number of TeO_4 groups in the glass. So, the broad absorption peak at the wavenumber 670cm^{-1} corresponds to the stretching vibrational mode of isolated TeO_3 units. The wavenumber 767 cm^{-1} corresponds to the vibration of continuous TeO_3 tp [4].

3.2.5. $20Fe_2O_3$ - $(80-x)TeO_2$ –x Bi_2O_3 glass system:

The IR spectra obtained for this series is more similar to that of above series, i.e., for $10Fe_2O_3$ - (90-x)TeO_2 –x Bi_2O_3 glass system. Since the variation of Bi_2O_3 in this system is same as in the case of above series, the position of bands and the appearance of peaks is similar to the above series. So, the discussion is as mentioned above.

3.2.6. (100-x)(70Bi_2O_3 20ZnO 10 PbO) – xFe_2O_3 glass system:

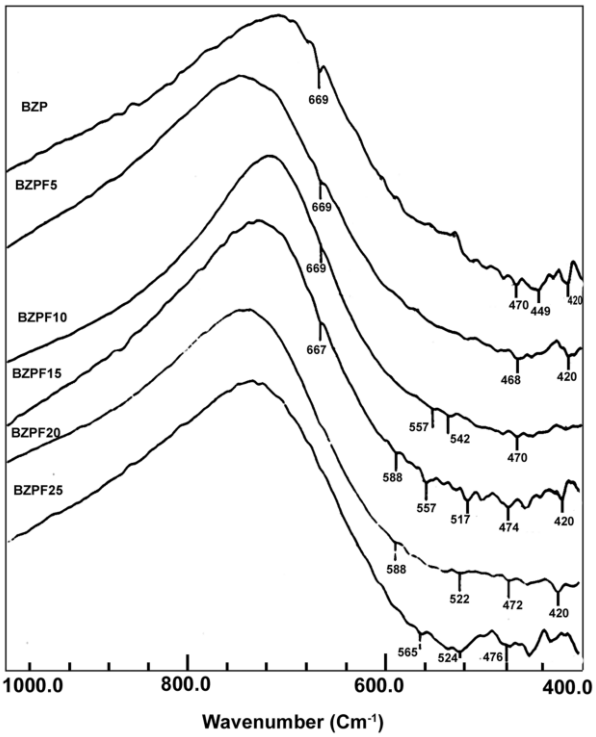

Fig 3.2.6 IR absorption spectra of (100-x)(70Bi_2O_3 20ZnO 10 PbO) – xFe_2O_3

The IR spectra of the investigated vitreous samples are highly broadened and poorly resolved. The absorption bands are observed at the positions 667, 588, 557, 500, 470, 448 and 420 cm^{-1}. The bands (550-580 cm^{-1}) are assigned to the vibration of the [$Fe^{3+}O_6$] octahedral groups. By increasing the Fe_2O_3 content these bands maximum is shifting to lower wave number (i.e., from 580 cm^{-1} to 550 cm^{-1}) and its intensity increases. This could be the presence of [FeO_6] octahedral groups. The minor absorption peak at 667 cm^{-1} could be because of either α-Bi_2O_3 or FeO_4 groups in ferrite compounds. The bands at 448cm^{-1} and 548cm^{-1} are due to the vibrations of Bi-O bonds in BiO_6 octahedral units [13-15]. With the addition of Fe_2O_3 to the glass system, the absorption bonds at 448 and 548 $cm^{-1}$for Bi-O bonds in BiO_6 octahedral units become weak. This observation indicates the structural changes occurred between Bi-O bonds and Fe-O bonds. The IR bands in the range 515-550 cm^{-1} are due to FeO_6 octahedra[9]. An increase of the broadline, near the 500 cm^{-1} band with increasing concentration of Fe_2O_3 is due to incorporation of the modifier into the network of glass former. The broadening of the lines and reduction of their intensity is more pronounced at higher 'disorder' in the structure. The higher covalency degree of the bonds leads to both broadening of the bands and to reducing of their intensity. The shoulder at 470 cm^{-1} is due to the formation

of O-Fe stretching vibration, i.e., there is a fraction of Fe cat ions which have partial covalent bonding and are incorporated in the network of these glasses. The peak at 470cm^{-1} is related to symmetric bending of vibration of Pb-O in PbO_4 tetragonal pyramid (PbO covalent bond) and Bi-O bond bending of strongly distorted BiO_6 octahedral units formed when Pb and Bi act as network former in a glass matrix [16]. The absorption peak around 420 cm^{-1} suggests the ZnO bond formation[17, 18]. It suggests that the peak characteristics of Pb-O and Zn-O vibrations remain in the region below 600 cm^{-1}, but the intensity of the peaks is becoming weak with the addition of Fe_2O_3 and the peaks are too weak to be detected in the amorphous (100-x) (70Bi2O3 20ZnO 10 PbO) – xFe_2O_3 glass system.

In conclusion, The observed IR spectra for the glass system (100-x)TeO_2 – xCuO suggest the presence of Te-O bonds. Symmetrical TeO_3 groups dominate in the range from 710 to 670cm^{-1} and the shoulder in the range 640-630 cm^{-1} is due to the decrease in the symmetry of the TeO_3 groups. Symmetric TeO_4 groups are characterized by a maximum at 670cm^{-1} and a shoulder at 635 cm^{-1}. Deformed TeO_4 groups have intense bands in the range of about 640-635cm^{-1} and a shoulder at about 670cm^{-1}. The IR vibration bands of tellurite units are found to shift to higher wave number with partial replacement of TeO_2 by CuO. The disorder in the structure increases with the increase in modifier content for all the glass systems. We observe bands characteristic of TeO_3 and TeO_4 for the glass systems (20-x)ZnO-80TeO_2-xFe_2O_3, 20ZnO-(80-x)TeO_2-xFe_2O_3, 10Fe_2O_3 – (90-x) TeO_2 –x Bi_2O_3 and 20Fe_2O_3 – (80-x) TeO_2 –x Bi_2O_3 . The band at 420cm^{-1} is due to the presence of ZnO in the spectra of both zinc tellurite glasses doped with iron oxide, but the band intensity decreases with the addition of Fe_2O_3. The shoulder at 470cm^{-1} is due to the formation of Te-O-Fe stretching vibrations. The shoulder at 565cm^{-1} is due to the Te-O-Fe bond vibrations, Fe is characterized by intermediate polarizing power. This group has an intermediate amount of non-bridging oxygen (NBO). The bands at 448 cm^{-1} and 548 cm^{-1} are due to the vibrations of Bi-O bonds in BiO_6 octahedral units. The introduction of modifier in the glass leads to a $TeO_4 \rightarrow TeO_{3+1} \rightarrow TeO_3$ transition. The number of TeO_{3+1} units is limited by modifier addition. With increase in modifier content the TeO_{3+1} units transform into TeO_3 and TeO_2 units.

In the glass system (100-x) (70Bi_2O_3 20ZnO 10 PbO) – xFe_2O_3, with the addition of Fe_2O_3 , the absorption bands at 448 and 548 cm^{-1}for Bi-O bonds in BiO_6 octahedral

units become weak. This indicates the replacement of Bi-O bonds by Fe-O bonds. The shoulder at 470 cm^{-1} is due to the formation of O-Fe stretching vibration, i.e., there is a fraction of Fe cations which have partial covalent bonding and are incorporated in the network of these glasses.

3.3. DSC STUDIES

Differential Scanning Calorimetric (DSC) is a thermo analytical technique used in understanding crystallization kinetics of glasses which is associated with the study of thermal parameters. This technique is simple, informative and useful for identifying glass compositions with high thermal stability and synthesizing glass ceramics with controlled heat treatment. There are some reports in the literature on the DSC studies of tellurite glasses containing 3d transition metal (TM) ions [3-4, 19-27]. Almost all the studies show the variation of thermal parameters with glass composition. Basically to estimate and calculate thermal parameters like glass transition temperature (T_g), onset crystallization temperature (T_O), crystallization peak temperature (T_p), thermal stability of the glass(ΔT), enthalpy of crystallization(ΔH), activation energy of crystallization(E_c) and dimension of crystallization(m), we used DSC technique. Along with the variation of thermal parameters with composition, we high light the crystallization kinetics of the glasses also in our work.

The thermal behavior was studied using Differential Scanning Calorimeter (DSC), TA Model DSC 2010 for copper tellurite glasses and iron tellurite glasses containing bismuth oxide [series 1, 4 and 5]. We used the model METLER DSC for zinc tellurite glasses containing iron oxide and multicomponent rich bismuthate glasses [seires 2, 3 and 6]. In order to investigate the crystallization kinetics, the non isothermal DSC studies were carried out on the glass samples. The small bulk pieces of different glass samples weighting 4- 6 mg were used to avoid the effect of grain size. The non-isothermal DSC thermograms were recorded for all the samples with heating rates of 5, 7.5, 10 and 12.5 ^{0}C /min in the temperature range 50 -550^{0}C.

3.3.1. (100-x)TeO_2 – xCuO glass system:

The DSC thermograms for various samples recorded at heating rate of 10^0C/min are shown in figure 3.3.1.1. Most of the samples show a well-defined sharp DSC crystallization peak indicating a uniform amorphous phase in the samples. Two characteristic temperature regions are evident in the DSC thermograms. The first one corresponds to the glass transition region (endothermic reaction) and the other to the crystallization region (exothermic reaction). The glass transition temperature T_g has been defined as the temperature, which corresponds to the intersection of the two linear portions adjoining the transition elbow of the DSC trace in the endothermic direction. Table 3.3.1.1 represents the various crystallization parameters T_g , T_o, T_p and ($\Delta T = T_o - T_g$) of various glass compositions. Variation of these thermal parameters with the composition of CuO is shown in figure 3.3.1.2. In the present system, T_g decreases by ~ 20 ^{0}C with very small increase in ΔT as CuO content increases from10 to 20%. With further increase in CuO content , T_g shows small decreasing trend whereas ΔT shows a sudden jump at x = 30 followed by marginal increase for higher values of CuO content. The T_o and T_p are minimum for glass with CuO content of 20 mol%. In the case of samples T7C3, T6C4 and T5C5 the glass transition characterized by the temperature, T_g, is followed by more than one exothermic peak corresponding to several crystallization temperatures, T_p. This shows different stages of crystallization. The samples show more than one exothermic peaks indicating multi crystallization. Multi crystallization is indicative of phase separation occurring in the crystallized samples.

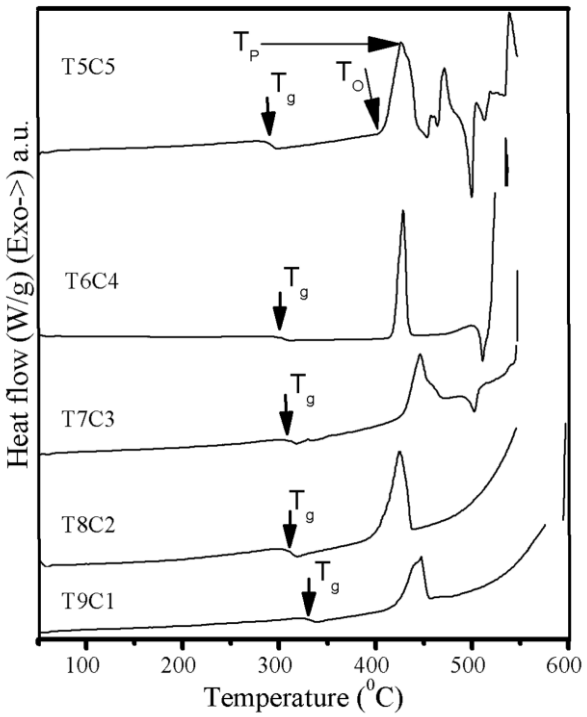

Fig 3.3.1.1 DSC thermograms of glass samples in the series (100-x)TeO_2 – xCuO

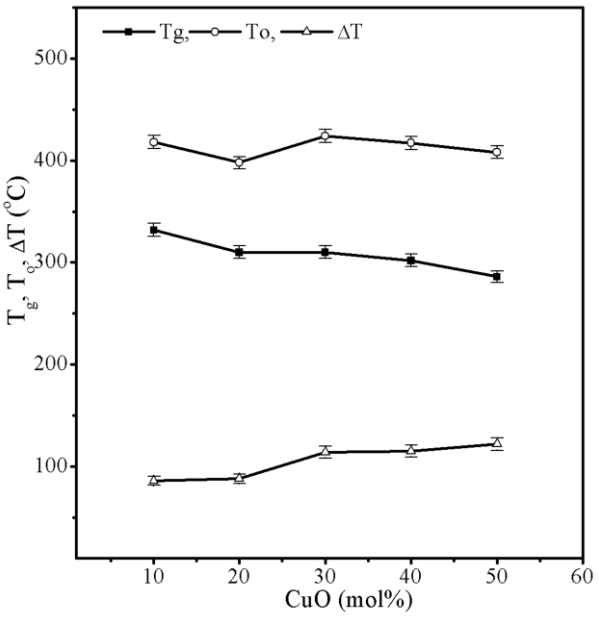

Fig 3.3.1.2 CuO composition variation of thermal parameters of glass samples

Table 3.3.1.1 Thermal parameters for various glass compositions (100-x)TeO_2 – xCuO

Sample	Composition x	T_g ($\pm 2^0$C)	T_o ($\pm 2^0$C)	T_p ($\pm 1^0$C)	ΔT ($\pm 2^0$C)
T9C1	10	332	418	442	86
T8C2	20	310	398	426	88
T7C3	30	310	424	446	114
T6C4	40	302	417	428	115
T5C5	50	286	408	427	122

The crystallization kinetics is studied for some of the synthesized glasses and data is analyzed in view of Kissinger and Matusita and Sakka models. According to the Kissinger's method [28, 29], the kinetics of such reaction can be conveniently studied by varying the heating rate and observing the peak temperatures with all other experimental conditions fixed. An amount of energy, called the glass transition activation energy E_c, must be given to groups of atoms in the glassy region so that a jump to a metastable state of more stability takes place. The evaluation of E_c has been widely carried out using Kissinger's equation

$$\ln\left[\frac{\alpha}{T_p^2}\right] = -\frac{E_c}{R}\left[\frac{1}{T_p}\right] + const. \qquad (3.3.1)$$

where T_p is the crystallization peak temperature, $\alpha = (dT/dt)$ the heating rate, E_c is the glass transition activation energy and R is the gas constant. If a plot of $\ln(\alpha / T_p^2)$ vs. $1/T_p$ gives a straight line, then its slope will yield E_c. Figure 3.3.1.3 shows Kissinger plots for various glass samples. The estimated E_c for various glasses are listed in Table 3.3.1.2.

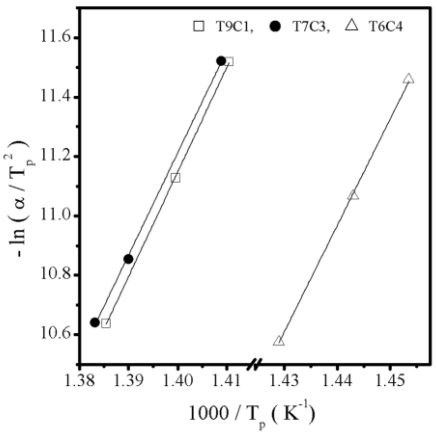

Fig 3.3.1.3 Kissinger plots for some glass samples

Matusita and Sakka [30, 31] proposed a method for analyzing the non-isothermal crystallization kinetics on the basis of nucleation and growth process and emphasized the crystallization mechanism such as bulk crystallization or surface crystallization. The authors proposed the methods for determining the activation energy for crystal growth in glass from DSC curves by analyzing the peak height on the basis of the nucleation and growth equations.

$$\ln \alpha = -1.052 \frac{m}{n} \frac{E_c}{RT} - \frac{1}{n} \ln\left[-\ln(1-x)\right] + const. \qquad (3.3.2)$$

where m is dimension of crystallization, n is avrami constant, T is absolute temperature and x is crystal volume fraction. The plot of ln [-ln (1-x)] vs 1/T, where T is the temperature at which the crystal volume fraction reaches a specific value, gives a straight line and slope gives the value 1.052(m/n)E. Here, n=m+1 for a quenched glass containing no nuclei, and n=m for a glass containing a sufficiently large number of nuclei.

Also, m=3 for three-dimensional growth of crystal particles,

m=2 for two-dimensional growth, eg: in a thin film glass,

m=1 for one-dimensional growth, eg: in a fibre glass or surface crystallization.

The n value can be obtained from the plot of ln [-ln (1-x)] vs ln α at a specific temperature. Theoretically, the maximum value of n is 4 and minimum value is 1. To evaluate E_c, m, and n in the crystallization mechanism, the results were analyzed using the Matusita model.

The rate of increase of variation of crystal volume fraction reaches its maximum at a temperature T_p, which gives us

$$\ln\left[\frac{\alpha^n}{T_p^2}\right] = -1.052m\frac{E_c}{R}\left[\frac{1}{T_p}\right] + const. \qquad (3.3.3)$$

This is very similar to the so-called Kissinger equation (1) when n=m=1, so we call this a modified Kissinger-type equation. Usually, the change of ln T_p^2 with α is negligibly small compared with the change of ln α^n, and, therefore, the modified Kissinger-type equation (3.3.3) is essentially the same as the Matusita equation (3.3.2).

As per equation (3.3.2), n is obtained as the slope of the resulting straight line fit of ln [-ln (1-x)] vs ln α plot at any fixed temperature. Figure 3.3.1.4 shows ln [-ln (1-x)] vs ln α plots. The value of n evaluated for various samples are listed in table 3.3.1. 2. The plot of ln [-ln (1-x)] vs 1/T, where T is the temperature at which the crystal volume fraction reaches a specific value, gives a straight line and the slope (1.052m/ E_c) gives the value of E_c. It is observed that the plots are linear over most of the temperature range as shown in figures 3.3.1.5, 3.3.1.6 and 3.3.1.7 for different samples. At high temperature or in the region of large crystallized reactions, a deviation from linearity or a lowering of the initial slope is seen for all the heating rates. Generally, this break in slope is attributed to the saturation of nucleation sites in the final stages of crystallization or to the restriction of crystal growth by the small size of the particles. In all these cases where there is a change in slope, the analysis is confined to the linear region. From the slope of the ln [-ln (1-x)] vs. 1000/T, mE_c values were calculated for all the heating rates. An average value of mE_c calculated by considering all the heating rates is listed in table 3.3.1.2. The estimated E_c values are listed in table 3.3.1.2. The value of E_c evaluated by using the estimated m and n values along with the (m/n) E_c value obtained from the ln α/T_p^2 vs 1000/ T_p plots are also listed in table 3.3.1.2. The values of E_c obtained from two models are in fair agreement for samples T9C1 and T7C3. However, there is a large difference in the value of E_c for sample T6C4 estimated using the two models. The crystallization peak for this sample is sharp. The value of n is 5.6 which is more than the maximum value predicted for three dimensional crystal growth according to Matusita model. The glasses containing high CuO content show the formation of Cu- clusters [20]. These clusters may act as nucleating centers for crystal growth and may lead to faster growth of crystallites

than predicted by Matusita model. Further work on different glass systems is required to understand this aspect.

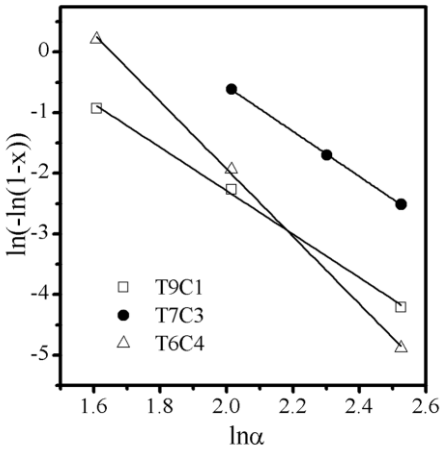

Fig 3.3.1.4 Plots of ln(-ln(1-x)) Vs. ln α for glass samples

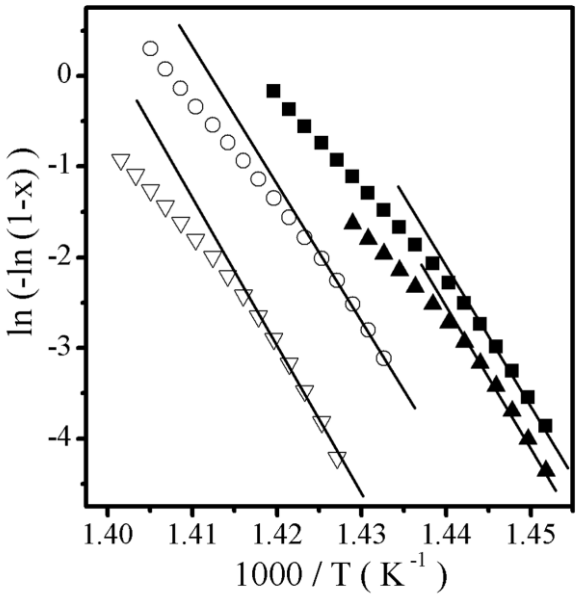

Fig 3.3.1.5 Plot of ln(-ln(1-x)) vs. 1000/T for the sample T9C1 at heating rates of (■) 5^{0}C/min, (○) 7.5 ^{0}C/min, (▲) 10^{0}C/min, (Δ) 12.5^{0}C/min

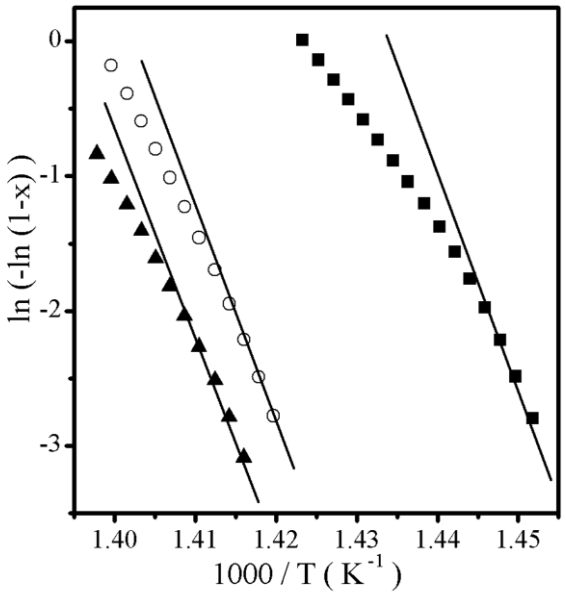

Fig 3.3.1.6 Plot of ln(-ln(1-x)) vs. 1000/T for the sample T7C3 at heating rates of (■) 5^{0}C/min, (○) 10 ^{0}C/min, (▲) 12.5^{0}C/min

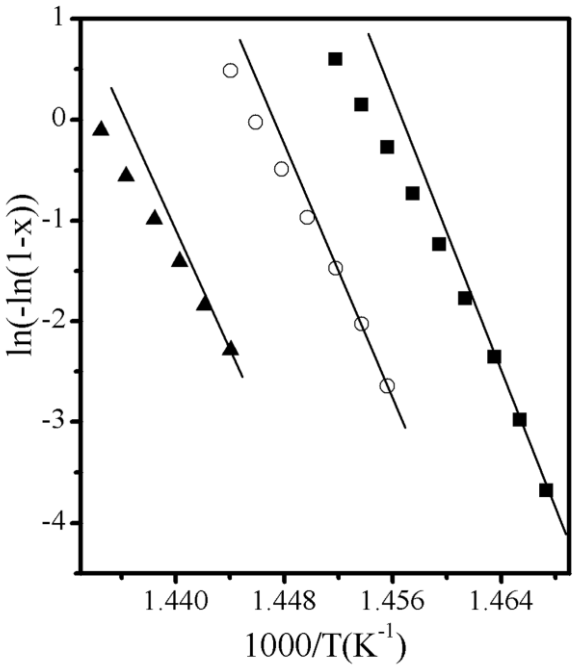

Fig 3.3.1.7 Plot of ln(-ln(1-x)) vs. 1000/T for sample T6C4 at heating rates of (■) 5^{0}C/min, (○) 7 ^{0}C/min, (▲) 12.5^{0}C/min

Table 3.3.1.2 The dimensional parameters and activation energies from Matusita and Kissinger plots.

Glass Sample	Heating Rate (^{0}C/min)	Matusita plots					Kissinger plots	
		ln (-ln (1-x)) vs. ln α		ln(-ln(1-x)) vs. 1000/T			-ln(α /T_p^2) vs. 1000/T_p	
		n	m	mE_c (kJ/mol)	E_c (kJ/mol)	Average E_c (±3kJ/mol)	(m/n)E_c (kJ/mol)	E_c (±3kJ/mol)
T9C1	5	3.6	2.6	1058	407	410	292	404
	7.5			1072	413			
	10			1073	413			
	12.5			1057	406			
T7C3	5	3.7	2.7	1056	391	389	286	395
	10			1038	385			
	12.5			1054	390			
T6C4	5	5.6	4.6	1831	398	401	298	363
	7.5			1946	423			
	12.5			1759	382			

Discussion:

There is a sudden change in structural units of the glass samples taking place when x mol% of CuO is increasing from 10 to 20. With the increase of CuO content, from 10 to 20 mol%, the basic structural units of TeO_2 glasses is changing from TeO_4 to TeO_{3+1} and hence TeO_3. The isolation of structure is changing from 10 mol% CuO to formation of clusters with increase in CuO content. And with further increase in CuO content leads to Cu-O-Cu to the direct Cu-Cu bonds and hence the formation of ferromagnetic clusters in the glasses is taking place. We can observe this drastic change from DSC. From DSC studies, the T_g value is suddenly decreasing from 332 to 310K with increase in CuO content from 10 to 20 mol%. It is because of change in the entire network of tellurite glasses. With 10 mol% of CuO, the basic structural unit is TeO_4, and with increase of CuO, the placement of Cu causes the change in glass network from TeO_4 to TeO_4-TeO_3 and TeO_3 units. This part we can observe from IR studies also. With further increase in CuO content, i.e., from 20 to 50 mol% of CuO there is a slow change

in structure and because of high Cu content, clustering is taking place. We can also say that at this particular high concentration of CuO, it can lead to a deficiency of oxygen and hence Cu^{+} content is increasing.

These results show that the thermal properties undergo significant changes when the modifier content changes in the range of 20 -30 %. The glasses with low modifier content consist of a continuous random network constructed by sharing corners of TeO_4 trigonal bipyramids and TeO_{3+1}. For the glasses with modifier content in the range 20–30 mol %, TeO_3 trigonal pyramids having non bridging oxygen spread to the whole network giving rise to high thermal stability to the glass network. Further increase of modifier content results in isolated structural units such as Te_2O_{5+2+2} which coexists in the continuous network. Above 30 mol% of modifier oxide, the glass network consists of TeO_{3+1} polyhedra and TeO_3 trigonal pyramids along with isolated structural units such as Te_2O_{5+2+2} and TeO_{3+2+2}. The TM ions are known to form magnetic clusters. At higher content of TM oxide these magnetic clusters may also act as nucleating centres for crystallization and thus increase the thermal stability of glass network and saturate the glass transition temperature. TeO_2-rich glasses are characterized by TeO_4 building units. Both Te-O_{ax} axial bonds in theTeO_4 polyhedra are strongly dynamic and easily attacked by the modifier. When a modifier oxide is introduced in the glass matrix, one of the Te-O_{ax} bonds in TeO_4 polyhedra undergoes elongation. The introduction of a modifier in the binary glass leads to a $TeO_4 \rightarrow TeO_{3+1}$ transition. The number of TeO_{3+1} units is limited by modifier addition. With increase in modifier content the TeO_{3+1} units transform into TeO_3 and TeO_2 units.

3.3.2. (20-x)ZnO-80TeO_2-xFe_2O_3 glass system:

The thermograms for various samples recorded at heating rate of $10\ ^{0}$ C/min are shown in figure 3.3.2.1. Most of the samples show well-defined DSC crystallization peaks indicating a uniform amorphous phase in the samples. Table 3.3.2.1 lists thermal parameters T_g, T_o, T_p and ($\Delta T = T_o - T_g$). Both T_g and ΔT increase with the increase in Fe_2O_3 content.

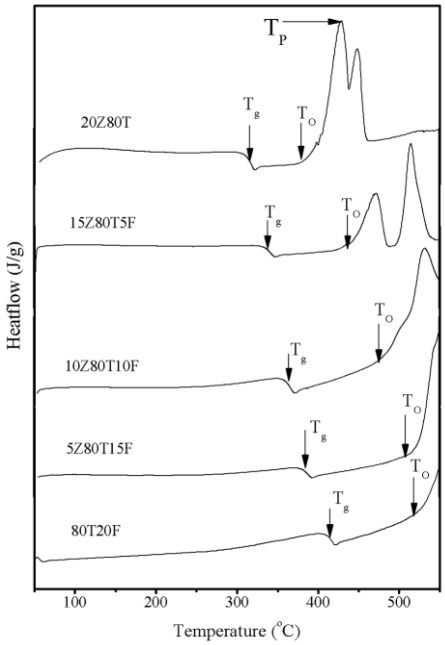

Fig3.3.2.1 DSC thermograms for glass samples at 10^0C/min

Table 3.3.2.1 Thermal parameters for various compositions of glass system (20-x)ZnO-80TeO_2-xFe_2O_3

Sample	Composition (x)	T_g ($\pm2^0$C)	T_o ($\pm2^0$C)	T_{p1} ($\pm1^0$C)	T_{p2} ($\pm1^0$C)	ΔT ($\pm2^0$C)
20Z80T	0	311	382	429	449	71
15Z80T5F	5	335	425	473	515	90
10Z80T10F	10	359	458	500	530	99
5Z80T15F	15	380	515	543	---	135
80T20F	20	407	542	---	---	135

Figure 3.3.2.2 shows the Fe_2O_3 composition variation of thermal parameters T_g, T_o and ΔT in the glass system. All the three parameters are varying linearly representing the glass system as the formation of a solid solution. Glass transition temperature is increasing at the rate of 4.8^oC per unit mol., where as thermal stability is increasing at the rate of 2 ^oC per unit mol. in the present glass system. In the case of samples 20Z80T and 15Z80T5F T_g, is followed by more than one exothermic peak corresponding to several crystallization temperatures, T_p. This shows different stages of crystallization.

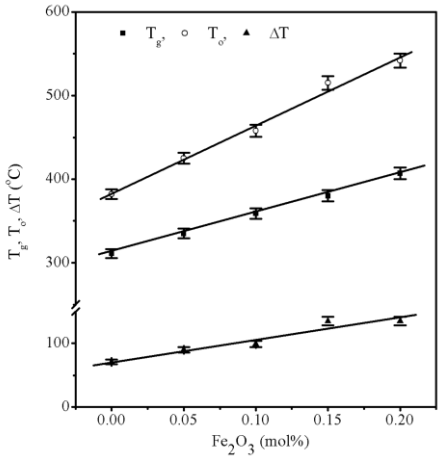

Fig 3.3.2.2 Fe_2O_3 composition variation of thermal parameters

3.3.3. 20ZnO-(80-x)TeO_2-xFe_2O_3 glass system:

The thermograms for various samples recorded at heating rate of 10 ^{0} C/min are shown in figure 3.3.3.1. Most of the samples show well-defined DSC crystallization peaks indicating a uniform amorphous phase in the samples. Table3.3.3.1 lists thermal parameters T_g, T_o, T_p and ΔT. Both T_g and ΔT increase with the increase in Fe_2O_3 content.

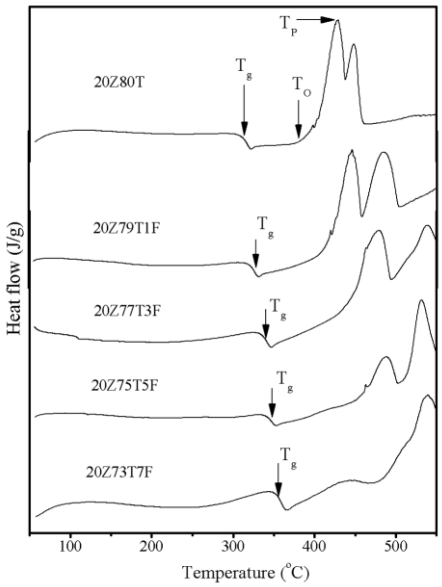

Fig 3.3.3.1 DSC thermograms for glass samples at 10^0C/min

Table 3.3.3.1 Thermal parameters for various compositions of 20ZnO-(80-x) TeO_2-xFe_2O_3 glasses

Sample	Composition (x)	T_g ($\pm2^0$C)	T_o ($\pm2^0$C)	T_{p1} ($\pm1^0$C)	T_{p2} ($\pm1^0$C)	ΔT ($\pm2^0$C)
20Z80T	0	311	395	429	449	84
20Z79T1F	1	321	415	446	461	94
20Z77T3F	3	335	439	477	537	104
20Z75T5F	5	342	461	487	531	119
20Z73T7F	7	353	474	538	---	121

Figure 3.3.3.2 shows the Fe_2O_3 composition variation of thermal parameters T_g, T_o and ΔT in the glass system. All the three parameters are varying linearly representing the glass system as the formation of a solid solution. Glass transition temperature is increasing at the rate of 6^oC per unit mol., where as thermal stability is increasing at the rate of $5.3\ ^oC$ per unit mol. in the present glass system. In the present glass system, for all the samples T_g, is followed by more than one exothermic peak corresponding to several crystallization temperatures, T_p, represents multi crystallization.

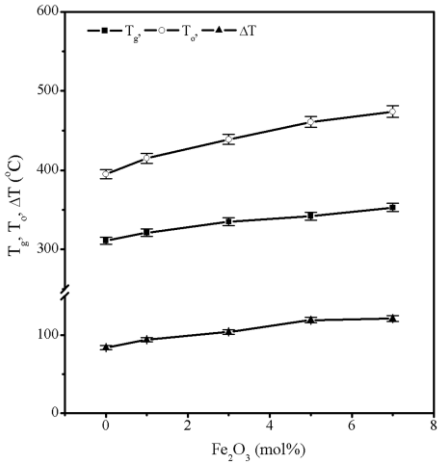

Fig 3.3.3.2 Fe_2O_3 composition variation of thermal parameters

3.3.4. $10Fe_2O_3 – (90\text{-}x)\ TeO_2 – x\ Bi_2O_3$ glass system:

The DSC thermograms for various samples recorded at heating rate of 10^0C/min are shown in figure 3.3.4.1. Most of the samples show a well-defined sharp DSC crystallization peak indicating a uniform amorphous phase in the samples. Table 3.3.4.1 represents the various crystallization parameters like T_g , T_o, T_p and ΔT of various glass compositions. Variation of these thermal parameters with the composition of Bi_2O_3 is shown in figure 3.3.4.2. In the present system, T_g increases with the increase in Bi_2O_3 content. ΔT is maximum for 10 mol% of Bi_2O_3. In the case of samples 10F90T, 10F75T15Bi and 10F70T20Bi the glass transition characterized by the temperature, T_g, is followed by more than one exothermic peak T_p, represents multi crystallization.

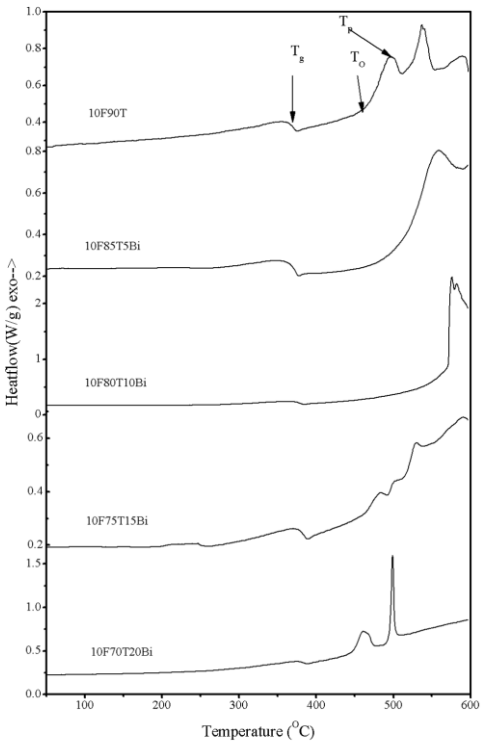

Fig 3.3.4.1 DSC thermograms of glass samples in the series $10Fe_2O_3 – (90\text{-}x)\ TeO_2 – x\ Bi_2O_3$

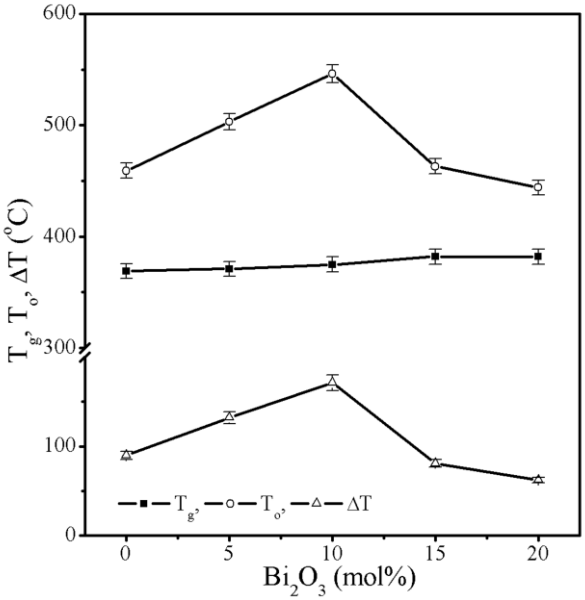

Fig 3.3.4.2 Bi_2O_3 composition variation of thermal parameters of glass samples

Table 3.3.4.1 Thermal parameters for various glass compositions

Sample	Bi_2O_3 mol%	T_g ($\pm2^0$C)	T_o ($\pm2^0$C)	T_p ($\pm1^0$C)	ΔT ($\pm2^0$C)
10F90T	0	369	459	496	90
10F85T5Bi	5	371	503	559	132
10F80T10Bi	10	375	546	576	171
10F75T15Bi	15	382	463	483	81
10F70T20Bi	20	382	444	462	62

The crystallization kinetics is studied for 10F90T and 10F70T20Bi samples and data is analyzed in view of Kissinger and Matusita and Sakka models. Figure 3.3.4.3 shows Kissinger plots for various glass samples. The estimated E_c for various glasses are listed in Table 3.3.4.2.

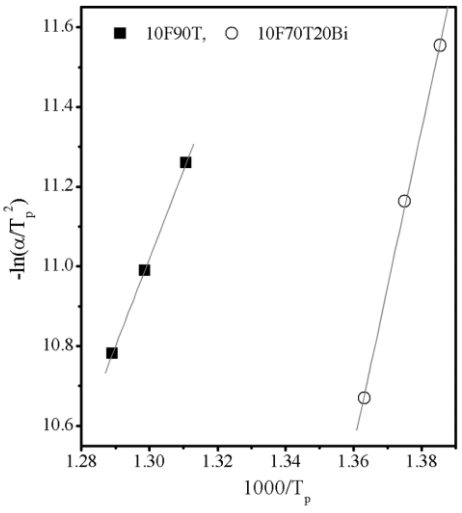

Fig 3.3.4.3 Kissinger plots for glass samples

Figure 3.3.4.4 shows ln [-ln (1-x)] vs ln α plots. The value of n evaluated for various samples are listed in table 3.3.4. 2. The plot of ln [-ln (1-x)] vs 1/T, where T is the temperature at which the crystal volume fraction reaches a specific value, gives a straight line and the slope (1.052m/ E_c) gives the value of E_c. It is observed that the plots are linear over most of the temperature range as shown in figures 3.3.4.5 and 3.3.4.6 for the two samples 10F90T and 10F70T20Bi respectively. At high temperature or in the

region of large crystallized reactions, a deviation from linearity or a lowering of the initial slope is seen for all the heating rates. Generally, this break in slope is attributed to the saturation of nucleation sites in the final stages of crystallization or to restriction of crystal growth by the small size of the particles. In all these cases where there is a change in slope, the analysis is confined to the linear region. From the slope of the ln [-ln (1-x)] vs. 1000/T, mE_c values were calculated for all the heating rates. An average value of mE_c calculated by considering all the heating rates is listed in table 3.3.4.2. The estimated E_c values are listed in table 3.3.4.2. The value of E_c evaluated by using the estimated m and n values along with the (m/n) E_c value obtained from the ln $\alpha/T_p^{\ 2}$ vs 1000/ T_p plots are also listed in table 3.3.4.2. The values of E_c obtained from two models are in fair agreement for the two samples 10F90T and 10F70T20Bi.

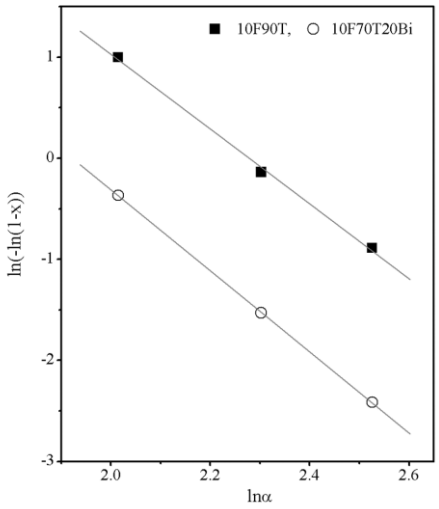

Fig 3.3.4.4 Plots of ln(-ln(1-x)) Vs. ln α for glass samples

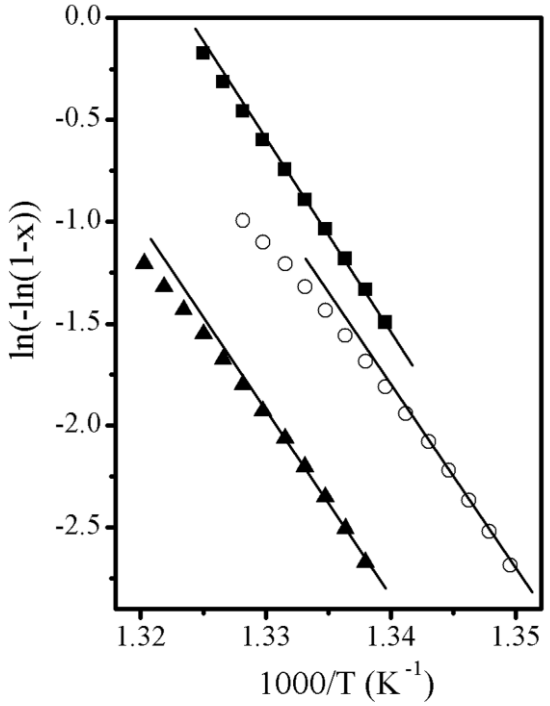

Fig 3.3.4.5 Plot of ln(-ln(1-x)) vs. 1000/T for the sample 10F90T at heating rates of (■) 7.5^{0}C/min, (○) 10^{0}C/min, (▲) 12.50^{0}C/min

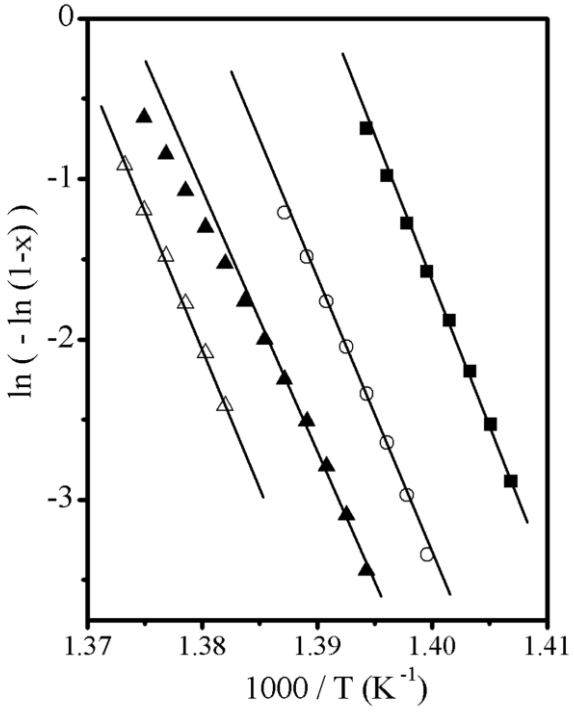

Fig 3.3.4.6 Plot of ln(-ln(1-x)) vs. 1000/T for the sample 10F70T20Bi at heating rates of (■) 5^{0}C/min, (○) 7.5^{0}C/min, (▲) 10^{0}C/min, (Δ) 12.5^{0}C/min

Table 3.3.4.2 The dimensional parameters and activation energies from Matusita and Kissinger plots

Sample	Heating Rate (^{0}C/min)	Matusita plots					Kissinger plots	
		ln (-ln (1-x)) vs. ln α		ln(-ln(1-x)) vs. 1000/T			-ln(α /T_p^2) vs. 1000/T_p	
		n	m	mE_c (kJ/mol)	E_c (kJ/mol)	Average E_c (±3kJ/mol)	(m/n)E_c (kJ/mol)	E_c (±3kJ/mol)
10F90T	7.5	3.7	2.7	706	264	260	184	252
	10			691	256			
	12.5			701	260			
10F70T20Bi	5	4	3	1353	451	449	329	440
	7.5			1349	450			
	10			1343	448			
	12.5			1348	449			

Discussion:

The glass transition characterized by the temperature, T_g, is followed by more than one exothermic peak, corresponding to several crystallization peaks. This shows different stages of crystallization. TeO_2 is known to crystallize in two main modifications [32]: Orthorombic β-TeO2 (tellurite) and tetragonal α-TeO2 (paratellurite) [33]. In both forms, the basic coordination polyhedron is a slightly distorted trigonal bipyramid with one equatorial position occupied by a lone electron pair.

For TeO_2 rich glasses the first exothermic peak may be attributed to nucleation and formation of a crystalline TeO_2 phase. The peaks at higher temperatures can be attributed to the formation of more relaxed crystalline phases of different compositions. However, detailed XRD studies are required to ascertain the phase formation at different exothermic peaks. In the present glass system, small increase in T_g and substantial increase in ΔT is observed with increase in Bi_2O_3 content from 0 to 10 %. With further

increase in Bi_2O_3 content there is marginal increase in T_g and very large decrease in thermal stability. Thermal stability shows a maximum value at 10 % Bi_2O_3 content.

The structural studies on TeO_2 - Fe_2O_3 glasses show the incorporation of Fe_2O_3 in the glass network as FeO_6 octahedra [9]. Bi_2O_3 is known to participate in the structure of glasses only as [BiO_6] groups [12]. It can be concluded from the present study that Bi_2O_3 is incorporated in the glass network up to a doping level of 10 % in the glass series $10Fe_2O_3$ – (90-x) TeO_2 –x Bi_2O_3.

These results show that the thermal properties undergo significant changes when the modifier content changes in the range of 5 -10 %. The glasses with low modifier content consist of a continuous random network constructed by sharing corners of TeO_4 trigonal bipyramids and TeO_{3+1}. For the glasses with modifier content in the range above 5-10 mol %, TeO_3 trigonal pyramids having non bridging oxygen spread to the whole network giving rise to high thermal stability to the glass network. Above 10 mol% of modifier oxide, the glass network consists of TeO_{3+1} polyhedra and TeO_3 trigonal pyramids along with isolated structural units such as Te_2O_{5+2+2} and TeO_{3+2+2}. The TM ions are known to form magnetic clusters. These magnetic clusters may also act as nucleating centres for crystallization and thus increase the thermal stability of glass network. TeO_2-rich glasses are characterized by TeO_4 building units. Both Te-O_{ax} axial bonds in theTeO_4 polyhedra are strongly dynamic and easily attacked by the modifier. When a modifier oxide is introduced in the glass matrix, one of the Te-O_{ax} bonds in TeO_4 polyhedra undergoes elongation. The introduction of a modifier in the binary glass leads to a TeO_4 $\rightarrow TeO_{3+1}$ transition. The number of TeO_{3+1} units is limited by modifier addition. With increase in modifier content the TeO_{3+1} units transform into TeO_3 and TeO_2 units.

3.3.5. $20Fe_2O_3$ - $(80-x)TeO_2$ –x Bi_2O_3 glass system:

The DSC thermograms for various samples recorded at heating rate of 10^0C/min are shown in figure 3.3.5.1. Most of the samples show a well-defined sharp DSC crystallization peak indicating a uniform amorphous phase in the samples. Table 3.3.5.1 represents the various crystallization parameters like T_g , T_o, T_p and ΔT of various glass compositions. Variation of these thermal parameters with the composition of Bi_2O_3 is shown in figure 3.3.5.2. In the present system, T_g decreases with the increase in Bi_2O_3

content. ΔT is maximum for 5 mol% of Bi_2O_3. In the case of samples 20F65T15Bi and 20F60T20Bi the glass transition characterized by the temperature, T_g, is followed by more than one exothermic peak corresponding to several crystallization temperatures, T_p , represents multi crystallization.

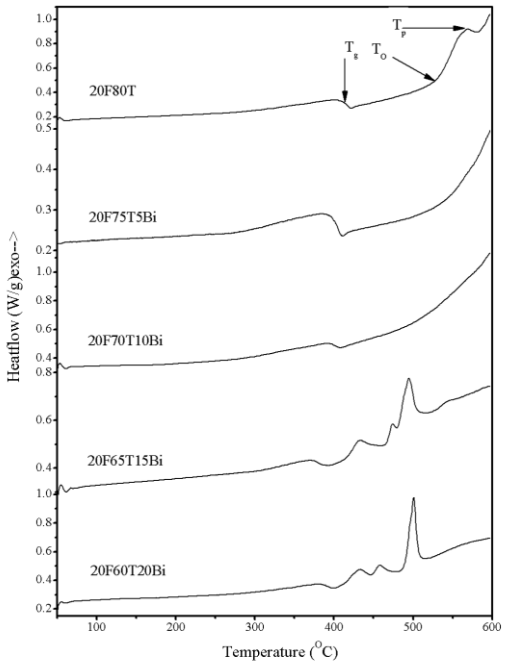

Fig 3.3.5.1 DSC thermograms of glass samples in the series $20Fe_2O_3$ – (80-x) TeO_2 –x Bi_2O_3

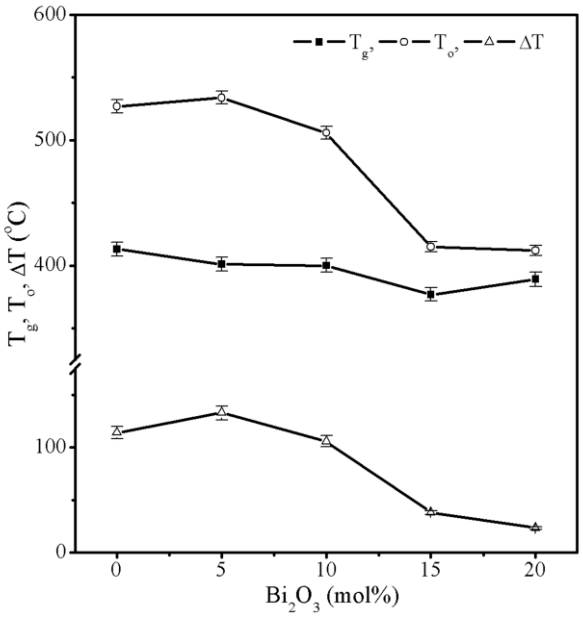

Fig 3.3.5.2 Bi_2O_3 composition variation of thermal parameters of glass samples

Table 3.3.5.1 Thermal parameters for various glass compositions

Sample	Bi_2O_3 mol%	T_g ($\pm 2^0$C)	T_o ($\pm 2^0$C)	T_p ($\pm 1^0$C)	ΔT ($\pm 2^0$C)
20F80T	0	413	527	568	114
20F75T5Bi	5	401	534	---	133
20F70T10Bi	10	400	506	---	106
20F65T15Bi	15	377	415	432	38
20F60T20Bi	20	389	412	432	23

The crystallization kinetics is studied for 20F60T20Bi sample and data is analyzed in view of Kissinger and Matusita and Sakka models. Figure 3.3.5.3 shows Kissinger plot for the glass sample. The estimated E_c for the glass sample is listed in Table 3.3.5.2.

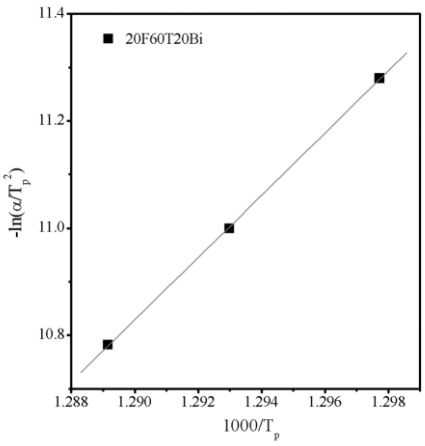

Fig 3.3.5.3 Kissinger plot for glass sample

Figure 3.3.5.4 shows ln [-ln (1-x)] vs ln α plot. The value of n evaluated for glass sample 20F60T20Bi is listed in table 3.3.5. 2. The plot of ln [-ln (1-x)] vs 1/T, where T is the temperature at which the crystal volume fraction reaches a specific value, gives a straight line and the slope (1.052m/ E_c) gives the value of E_c. It is observed that the plot is linear over most of the temperature range as shown in figures 3.3.5.5 for the sample 20F60T20Bi respectively. At high temperature or in the region of large crystallized reactions, a deviation from linearity or a lowering of the initial slope is seen for all the

heating rates. Generally, this break in slope is attributed to the saturation of nucleation sites in the final stages of crystallization or to restriction of crystal growth by the small size of the particles. In all these cases where there is a change in slope, the analysis is confined to the linear region. From the slope of the ln [-ln (1-x)] vs. 1000/T, mE_c values were calculated for all the heating rates. An average value of mE_c calculated by considering all the heating rates is listed in table 3.3.5.2. The estimated E_c values are listed in table 3.3.5.2. The value of E_c evaluated by using the estimated m and n values along with the (m/n) E_c value obtained from the ln $\alpha/T_p^{\ 2}$ vs $1000/T_p$ plots are also listed in table 3.3.5.2. The values of E_c obtained from two models are in fair agreement for the sample 20F60T20Bi.

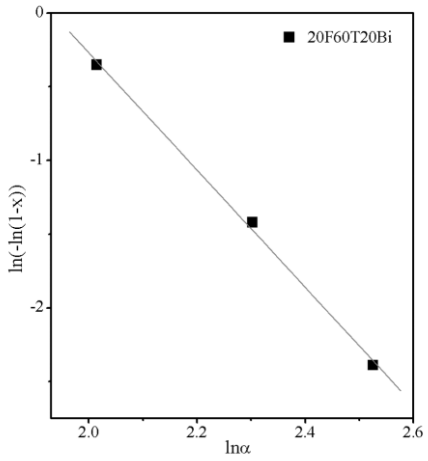

Fig 3.3.5.4 Plots of ln(-ln(1-x)) Vs. ln α for glass samples

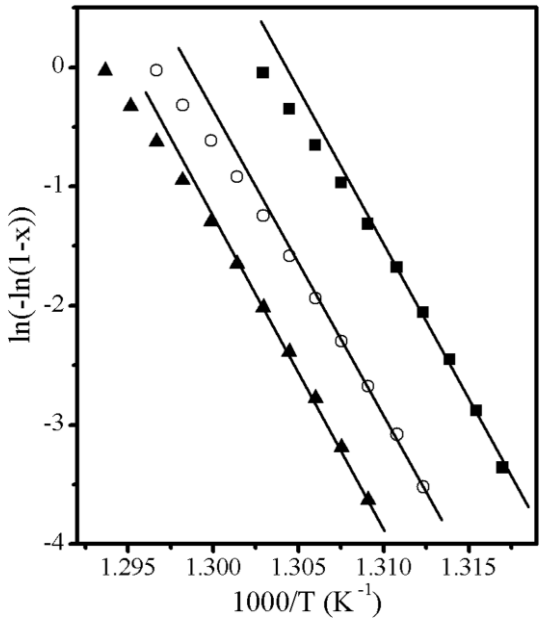

Fig 3.3.5.5. Plot of ln(-ln(1-x)) vs. 1000/T for the sample 20F60T20Bi at heating rates of (■) 7.5^{0}C/min, (○) 10^{0}C/min, (▲) 12.5^{0}C/min

Table 3.3.5.2. The dimensional parameters and activation energies from Matusita and Kissinger plots

Sample	Heating Rate (^{0}C/min)	Matusita plots					Kissinger plots	
		ln (-ln (1-x)) vs. ln α		ln(-ln(1-x)) vs. 1000/T			-ln(α /T_p^2) vs. 1000/T_p	
		n	m	mE_c (kJ/mol)	E_c (kJ/mol)	Average E_c (±3kJ/mol)	(m/n)E_c (kJ/mol)	E_c (±3kJ/mol)
20F60T20Bi	7.5 10 12.5	3.97	3	1943 1928 1948	648 643 649	647	483	640

Discussion:

For TeO_2 rich glasses the first exothermic peak may be attributed to nucleation and formation of a crystalline TeO_2 phase. The peaks at higher temperatures can be attributed to the formation of more relaxed crystalline phases of different compositions. However, detailed XRD studies are required to ascertain the phase formation at different exothermic peaks. In the present glass system, T_g decreases about 100^oC with increase in Bi_2O_3 content from 0 to 10 %. Thermal stability reaches a maximum value at 5 % Bi_2O_3.

The structural studies on TeO_2 - Fe_2O_3 glasses show the incorporation of Fe_2O_3 in the glass network as FeO_6 octahedra [9]. Bi_2O_3 is known to participate in the structure of glasses only as [BiO_6] groups [12]. It can be concluded from the present study that Bi_2O_3 is incorporated in the glass network up to a doping level of 5 % in the glass series $20Fe_2O_3 – (80\text{-}x)\ TeO_2 – x\ Bi_2O_3$.

These results show that the thermal properties undergo significant changes when the modifier content changes in the range of 0 -10 %. The glasses with low modifier content consist of a continuous random network constructed by sharing corners of TeO_4 trigonal bipyramids and TeO_{3+1}. For the glasses with modifier content in the range 5-10 mol %, TeO_3 trigonal pyramids having non bridging oxygen spread to the whole network giving rise to high thermal stability to the glass network. Above 10 mol% of modifier oxide, the glass network consists of TeO_{3+1} polyhedra and TeO_3 trigonal pyramids along with isolated structural units such as Te_2O_{5+2+2} and TeO_{3+2+2}. The TM ions are known to form magnetic clusters. These magnetic clusters may also act as nucleating centres for crystallization and thus increase the thermal stability of glass network. TeO_2-rich glasses are characterized by TeO_4 building units. Both Te-O_{ax} axial bonds in theTeO_4 polyhedra are strongly dynamic and easily attacked by the modifier. When a modifier oxide is introduced in the glass matrix, one of the Te-O_{ax} bonds in TeO_4 polyhedra undergoes elongation. The introduction of a modifier in the binary glass leads to a $TeO_4 \rightarrow TeO_{3+1}$ transition. The number of TeO_{3+1} units is limited by modifier addition. With increase in modifier content the TeO_{3+1} units transform into TeO_3 and TeO_2 units.

3.3.6. (100-x)(70Bi_2O_3 20ZnO 10 PbO) – xFe_2O_3 glass system:

The thermograms for various samples recorded at heating rate of 10 ^{0} C/min are shown in figure 3.3.6.1. Most of the samples show well-defined DSC crystallization peaks indicating a uniform amorphous phase in the samples. Table3.3.6.1 lists glass transition temperature T_g, crystallization onset temperature T_o, crystallization peak temperature T_p and thermal stability ($\Delta T = T_o - T_g$). Both T_g and ΔT increase with the increase in Fe_2O_3 content. In the present glass system, for all the glass samples, the glass transition characterized by the temperature, T_g, is followed by more than one exothermic peak T_p, represents multi crystallization. Multi crystallization is indicative of phase separation occurring in the crystallized samples. The peaks at higher temperatures can be attributed to the formation of more relaxed crystalline phases of different compositions. However, detailed XRD studies are required to ascertain the phase formation at different exothermic peaks.

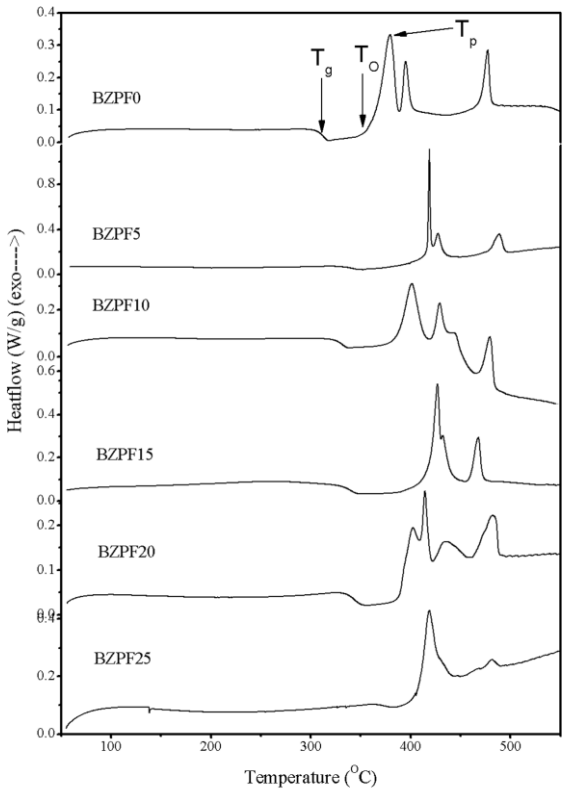

Fig 3.3.6.1 DSC thermograms for glass samples at 10^{0}C/min

Table 3.3.6.1 Thermal parameters for the glass system (100-x)(70Bi_2O_3 20ZnO 10 PbO) – xFe_2O_3

Sample	Fe_2O_3 mol%	T_g ($\pm2^0$C)	T_o ($\pm2^0$C)	T_p ($\pm1^0$C)	ΔT ($\pm2^0$C)
BZPF0	0	311	365	379	54
BZPF5	5	340	414	419	74
BZPF10	10	331	385	401	54
BZPF15	15	339	414	427	75
BZPF20	20	344	387	402	43
BZPF25	25	373	407	419	34

Figure 3.3.6.2 shows the Fe_2O_3 composition variation of thermal parameters T_g, T_o and ΔT in the glass system. All the three parameters are varying linearly representing the glass system as the formation of a solid solution. Glass transition temperature is increasing at the rate of 2.5^{o}C per unit mol., where as thermal stability is varying at the rate of 0.8 ^{o}C per unit mol. in the present glass system.

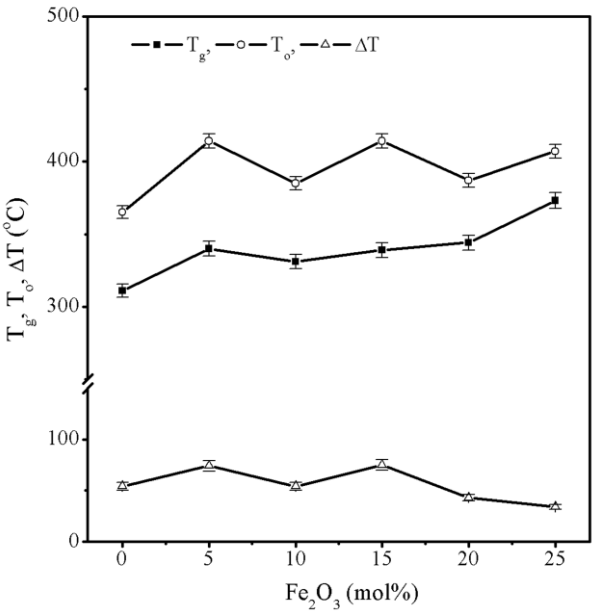

Fig 3.3.6.2 Fe_2O_3 composition variation of thermal parameters

Kissinger model is used to calculate activation energy for crystallization for some of the synthesized glasses. Figure 3.3.6.3 shows Kissinger plots for BZPF5, BZPF10 and BZPF20 glass samples. The estimated E_c values are 292 kJ/mol, 639 kJ/mol, 341 kJ/mol for BZPF5, BZPF10 and BZPF20 glasses respectively.

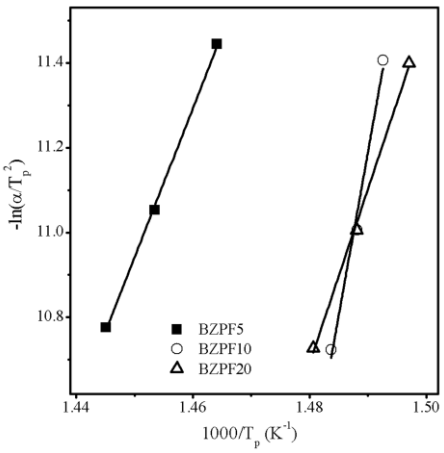

Fig 3.3.6.3 Kissinger plots for glass samples

In conclusion, most of the glass samples show well-defined DSC crystallization peaks indicating a uniform amorphous phase. The crystallization kinetics is studied for some glasses. The data is analyzed in view of Kissinger and Matusita & Sakka models. Some samples have the glass transition temperature, T_g followed by more than one exothermic peak corresponding to several crystallization temperatures, T_p. This shows different stages of crystallization, which is an indication of phase separation occurring in the crystallized samples. The dimension of crystallization is found to be 3 (three) for the tellurite glasses.

For Copper tellurite glasses, glass transition temperature (T_g) decreases and thermal stability (ΔT) increases with the increase in CuO content. The crystallization activation energy (E_c) is found to be in the range of 410-363kJ/mol for these glasses.

In the glass system (20-x)ZnO-80TeO_2-xFe_2O_3, both T_g and ΔT increase with the increase in Fe_2O_3 content. Glass transition temperature increases at the rate of 4.8^{o}C per

unit mol., where as thermal stability increases at the rate of 2^{o} C per unit mol. of Fe_2O_3 in the present glass system.

For the glass system $20ZnO\text{-}(80\text{-}x)TeO_2\text{-}xFe_2O_3$ glass transition temperature increases at the rate of 6^{o}C per unit mol., where as thermal stability increases at the rate of 5.3 ^{o}C per unit mol of Fe_2O_3. In the glass system $10Fe_2O_3 – (90\text{-}x)\ TeO_2 –x\ Bi_2O_3$, T_g increases with the increase in Bi_2O_3 content. ΔT is maximum for 10 mol% of Bi_2O_3. The activation energies for 10F90T and 10F70T20Bi are 252kJ/mol and 440kJ/mol respectively. In the glass system $20Fe_2O_3$ - $(80\text{-}x)TeO_2 –x\ Bi_2O_3$, T_g decreases with the increase in Bi_2O_3 content. ΔT is maximum for 5 mol% of Bi_2O_3. The activation energy value is 640kJ/mol for 20F60T20Bi.

For the glass system $(100\text{-}x)(70Bi_2O_3\ 20ZnO\ 10\ PbO) – xFe_2O_3$, both T_g and ΔT increase with the increase in Fe_2O_3 content. Glass transition temperature increases at the rate of 2.5^{o}C per unit mol. of Fe_2O_3, where as thermal stability increases at the rate of 0.8 ^{o} C per unit mol. Fe_2O_3 in the present glass system. The estimated E_c values are 292 kJ/mol, 639 kJ/mol, 341 kJ/mol for BZPF5, BZPF10 and BZPF20 glasses respectively.

References

[1] P. Tarte, *Spectrochim. Acta* **18,** 467 (1962).

[2] R.A. Condrat, in "*Introduction to Glass Science*", edited by L.D. Pye, H.J. Stevens and W.C. Lacourse *(Plenum Press, New York, London, 1972)* p. 101.

[3] A. A. Bahgat, I. I. Shaltout and A. M. Abu-Elazm, *Jr. of Non-Cryst. Solids* **150**, 179-184 (1992).

[4] B. V. R. Chowdari, K. L. Tan and Fang Ling, *Solid State Ionics* **113-115**, 711-721 (1998).

[5] A. K. Yakhkind, in "*Structure i fizikochimitsheskie svoistva neorganitsheskich stekol*", edited by A.G. Vlasov and V.A. Florinska *(Chimia, Leningrad, 1974)* p.67.

[6] Y. Dimitriev, V. Dimitrov and M. Arnaudov, *J. Mater. Sci.* **18** 1353-1358 (1983).

[7] Y. Dimitriev, Y. Ivanova, M. Dimitrova, E.D. Lefterova and P.V. Angelov, *J. Mater. Sci. Lett.* **19** 1513-1516 (2000).

[8] M. Arnaudov, V. dimitrov, Y. Dimitriev and L. Markova, *Mater. Res. Bull*., **17**, 159 (1982).

[9] V. Kozhukharov, S. Nikolov, M. Marinov and T. Troev, *Mater. Res. Bull*. **14** 735-741 (1979).

[10] R. A. Nyqist and R.O. Kagel, "IR spectra of Inorganic Compounds" *Academic Press, Newyork,* (1971).

[11] H. Burger, K. Kneipp, H. Hobert, W. Vogel, V. Kozhukharov and S. Neov, *J. Non-Cryst. Solids* **151** 134 (1992).

[12] Y. Dimitriev, Ch. Petkov, E. Gattev, T. Stoilova and G. Gochev, *J. Non-Cryst. Solids* **112** 120 (1989).

[13] A.H. Doweidar, Y. B. Saddeek, *J. Non-crys. Solids* **355** 348 (2009).

[14] M. Bosca, L. Pop, G. Borodi, P. Pascuta, E. Culea, *J. Alloys Compd.* **479** 579 (2009).

[15] A. Bishay and C. Maghrabi, *Phys. Chem. Glasses* **10 (1)** 1 (1969).

[16] Hamid-Reza Bahari, Hj. A. A. Sidek, Faisal Rafiq M. Adikan, Wan M. M. Yunus and Mohamed K. Halimah, Int. *J. Mol. Sci*. **13** 8609-8614 (2012).

[17] J. C. Hurt and C.J. Phillips, *J. Am. Ceram. Soc.*, **53** 269 (1970).

[18] S.G. Motke, S. P. Yawale and S. S. Yawale, Bull. *Mater. Sci.,* **25** 75-78 (2002).

[19] R. Singh *J. Phys.D*. **20** 548-551 (1987).

[20] P. Sandhya Rani and R. Singh *J. Mater. Sci.* **45** 2868 (2010).

[21] P. Sandhya Rani and R. Singh *J Phys & Chem Solids* **74** 338-343 (2013).

[22] M. A. Hassan and C. A. Hogarth *Jr. of Mater.Science*. **23** 2500-2504 (1988).

[23] Aswini Ghosh *J. Phys: Condens. Matter* **1** 7819-7828 (1989).

[24] P. Sandhya Rani and R. Singh, *Solid State Phys (India)* **49** 356 (2004).

[25] P. Sandhya Rani and R. Singh, *Solid State Phys (India)* **51** 379 (2006).

[26] P. Sandhya Rani and R. Singh, *Solid State Phys (India)* **52** 469 (2007).

[27] P. Sandhya Rani and R. Singh, *Solid State Phys (India)* **53** 641 (2008).

[28] H. E. Kissinger: *J. Res. Nat. Bur. Stand*. **57**, 217-221 (1956).

[29] H. E. Kissinger: Anal. Chem. **29**, 1702 (1957).

[30] K. Matusita and Sumio Sakka *Jr. of Non-Cryst. Solids* **38 & 39,** 741 (1980).

[31] K. Matusita, T. Komatsu and Ryosuse Yokota: *J. Mater.Sci.* **19**, 291 (1984).

[32] Beyer H *Z. Kristallogr.* **124** 228 (1967).

[33] P. A. V. Johnson, A. C. Wright, C. A. Yarker and R. N. Sincair *J. Non-Cryst. Solids* **81** 163 (1986).

Chapter 4

Electron spin resonance studies

The use of electron spin resonance (ESR) to characterize magnetic nanostructured systems [1, 2] has increased significantly during the recent years. The experimental technique is based upon the resonant absorption of microwaves by unpaired electrons in the presence of an externally applied magnetic field. The advantage of ESR over conventional magnetization measurements is that it yields information on the spin dynamics of the system. A mixture of microscopic phases containing a ferromagnetic contribution and a paramagnetic one is not easy to discriminate in a DC magnetization measurement, while it should be clearly distinguished in an ESR experiment. The ESR of TM ions in vitreous matrices may provide useful information about the short-range ordering of the paramagnetic ions. This is due to the fact that ESR absorption spectra show distinct resonance lines for the ions involved in structural units of well-defined symmetry and those connected in clusters.

The ESR spectra of all the synthesized glass samples listed in chapter 2 were recorded on Joel X-Band ESR spectrometer in the temperature range 123 -423K. The linewidth (ΔH), peak intensity (I), resonance field (H_r), area under the curve (A), g-values, number of spins (N), curie temperature (θ_c) etc., were calculated from the ESR spectra of the glass samples. The ESR studies of various series of glass samples are discussed in the following sections.

4.1. Copper tellurite glass system:

The ESR spectra of $(100-x)TeO_2$-xCuO, where x= 10, 20, 30, 40 and 50 glasses are shown in figure 4.1.1. The ESR pattern shows a strong dependence on the copper concentration. A well defined resonance at $g \approx 2.2$ with peak to peak linewidth (ΔH) of ~ 450 G and no hyperfine structure is observed for the x = 10 sample . The (ΔH) increases and the intensity of the resonance decreases as the CuO content increases. Very weak

ESR signal is observed in sample with x = 30. No ESR signal could be observed for sample with x = 40 and 50. The symmetry of the resonance line for x = 10 indicates a large absorption due to clusters containing more than one Cu^{2+} ion superimposed on the spectrum characteristic of isolated ions. Clustering tendencies of the copper ions in the matrix [3, 4] are consequently evident.

The resonance spectra in copper containing glasses are due to the Cu^{2+} ($3d^9$) ions entering in the glass matrix as paramagnetic species. When the concentration of Cu^{2+} ions are low, the spectra consists of hyperfine structure (hfs) due to I = 3/2 Cu^{2+} ions. The hfs is resolved in both parallel and perpendicular bands of the spectra, four hyperfine components being observed in each part of the ESR spectra. As the concentration of paramagnetic Cu^{2+} ions is increased the resolution diminishes due to broadening of the individual lines. The hfs smears out, so for samples with high paramagnetic ions content the line reduces to a borad envelope containing all contributions to the EPR absorption. Hence, when the concentration of Cu^{2+} ion increases the interactions between ions becomes stronger, the axial environment of the Cu^{2+} ions is destroyed and the absorption line becomes more symmetric with a g value ~ 2. With further increase of CuO concentration, the absorption spectrum reduces to a single, slightly asymmetric line. And, the decrease in intensity for x $\geq$ 20 mol % is due to increasing contribution from Cu^{2+} ion spins coupled in antiparallel configuration by super exchange –type interactions. The increase in CuO content increases the concentration of antiferromagnetically coupled Cu^{2+} ion leading to the line broadening and disappearance of ESR signal. The decrease in ESR signal intensity at high concentration of CuO in Copper tellurite glasses is also reported by Criocas et al [5] and is attributed to the presence of Cu^{+} and Cu^{2+} ions in the system , larger spatial disorder or the magnetic coupling between the ions. Thus, for x<20 mol% the dominant part of Cu^{2+} ions may be regarded as isolated species participating at dipole-dipole interactions, but at higher concentrations the dominant part of these ions experience superexchange interactions. At high concentrations decreasing of the intensity can be attributed to the presence of both Cu^{+} and Cu^{2+} ions in these glasses, the former one is being diamagnetic[6]. The concomitant presence of monovalent and divalent copper ions was also reported in various glasses [3-9].

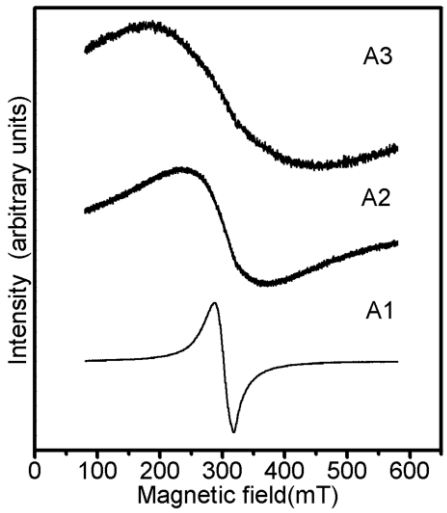

Figure 4.1.1. Room Temperature ESR spectra for (100-x)TeO_2-xCuO

Spins (N) participating in resonance

The number of spins participating in a resonance can be calculated by double integration of ESR spectra and comparison with that of a Varian standard ($CuSo_4$ in this study) of known concentration. Weil et al. [10] gave the following expression which includes the experimental parameters of both sample and standard.

$$N = \frac{A_x (Scan_x)^2 G_{std} (B_m)_{std} (g_{std})^2 [S(S+1)]_{std} (P_{std})^{1/2}}{A_{std} (Scan_{std})^2 G_x (B_m)_x (g_x)^2 [S(S+1)]_x (P_x)^{1/2}} [Std] \qquad (4.1)$$

where A is the area under the absorption curve which can be obtained by double integrating the first derivative of EPR absorption curve, scan is the magnetic field corresponding to unit length of the chart, G is the gain, B_m is the modulation field width, g is the g factor, S is the spin of the system in its ground state. P is the power of the microwave. The subscripts 'x' and 'std' represent the corresponding quantities for the glass sample and the reference ($CuSo_4$), respectively. The number of spins participating in resonance at g~2.2 has been calculated as a function of copper content by using the above Eq. (4.1). It is observed that N varies from 2.31×10^{20}, 1.92×10^{20} spins/g for 10 and 20 mol% of CuO respectively.

ESR spectra recorded in the temperature range 123 - 293K for 10 and 20mol% of CuO samples are shown in figure 4.1.2 (a) and (b) respectively. The intensity of the spectra increases with decrease in temperature and no significant change is observed in linewidth. The 1/DI vs. T plot (figure 4.1.3) for 10 mol% sample follows Curie -Weiss law with zero intercept on x – axis, represents paramagnetic nature of the glass. Whereas the 1/DI vs. T plot for 20 mol% sample shows negative intercept on the X-axis indicative of antiferromagnetic coupling between the copper ions.

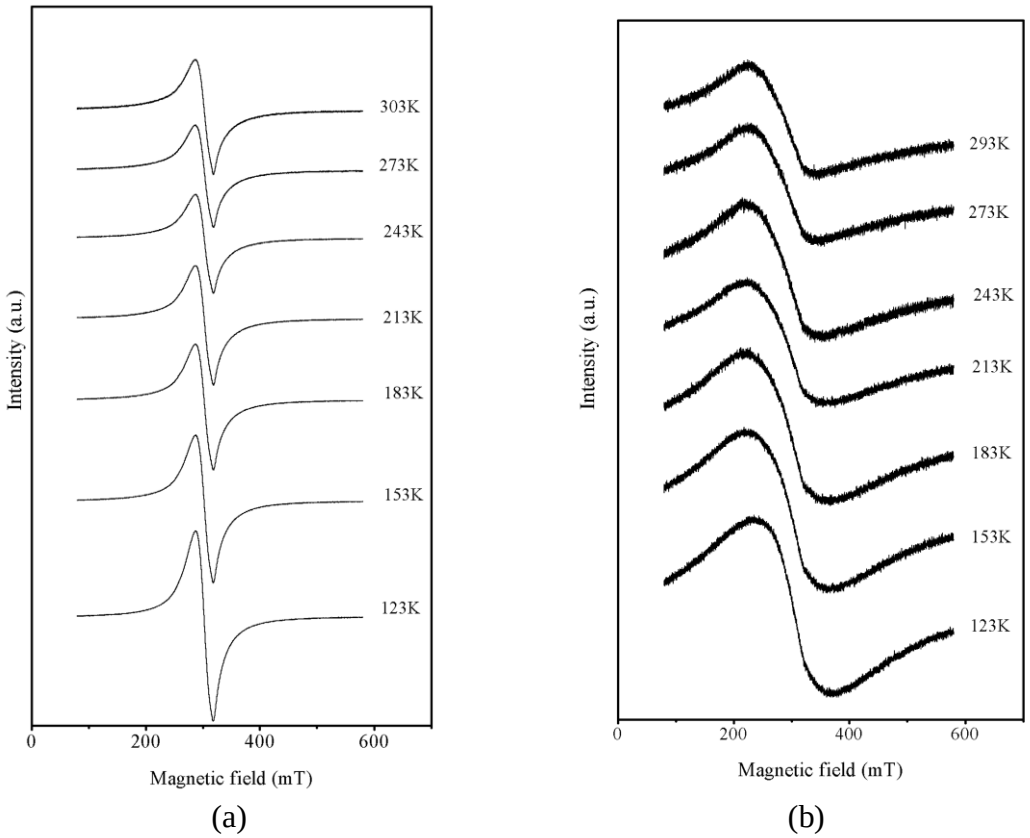

Fig 4.1.2. Temperature variation of ESR spectra for (a)10CuO-90TeO_2 and (b)20CuO-80TeO_2

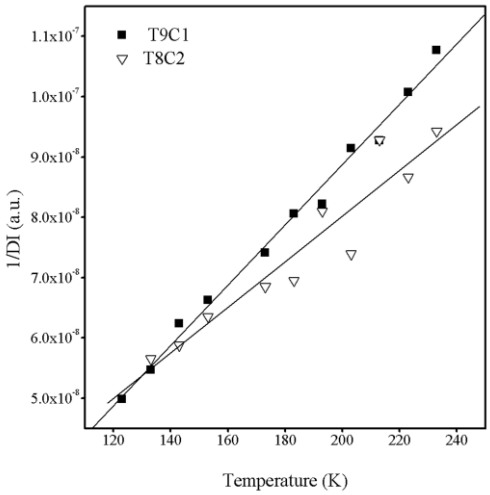

Fig 4.1.3. Temperature variation of 1/DI plots for 10 mol% and 20 mol% CuO glass samples

In brief, The ESR spectra of TeO_2-CuO glasses show a strong dependence on the copper concentration. The resonance spectra are due to the Cu^{2+} ($3d^9$) ions entering the matrix as paramagnetic species. A well defined resonance at $g \approx 2.2$ with peak to peak linewidth (ΔH) of ~ 450 G and no hyperfine structure is observed for the x = 10 sample. The ΔH increases and the intensity of the resonance decreases as the CuO content increases. Very weak ESR signal is observed in sample with x = 30. No ESR signal was observed for sample with x = 40 and 50. The symmetry of the resonance line for x = 10 indicates a large absorption due to clusters containing more than one Cu^{2+} ion superimposes the spectrum characteristic for isolated ions. With further increase of CuO concentration, the absorption spectrum reduces to a single, slightly asymmetric line. And, the decrease in intensity for $x \geq 20$ mol % is due to increasing contribution from Cu^{2+} ion spins coupled in antiparallel configuration by superexchange type interactions. The increase in CuO content increases the concentration of antiferromagnetically coupled Cu^{2+} ions leading to the line broadening and disappearance of ESR signal. From the temperature variation of electron spin resonance the double integrated intensity (DI) is estimated. The plot of 1/DI vs. T, follows Curie law, represents paramagnetic in nature of glass with 10 mol% of CuO, where as for the glass with 20 mol% CuO the negative intercept on x-axis of 1/DI vs. T plots represents the antiferromagnetic coupling between the copper ions.

4.2 The ESR spectra of Fe ion containing glasses:

ESR probe is suited not only to detect the spin transition, but also to yield valuable information on concomitant structural modifications in the matrix. The Fe ion can enter in the glass matrix as Fe^{1+}, Fe^{2+} and Fe^{3+}. Fe^{2+} ions are EPR-silent not only in their low-spin (S=0) diamagnetic state, but also in their high-spin (S=2) paramagnetic state, due to a very short spin-lattice relaxation time. Thus, in EPR study of the spin transition experienced by the Fe^{2+} ions, another paramagnetic ion presence must be exist in the matrix. The ESR can detect Fe^{3+} ions at room temperature because of existence of unpaired 3d electron. The ESR spectra of Fe^{3+} ions in oxide glasses are generally characterized by the appearance of resonance absorptions at g≈6.0, 4.27 and 2.0, their relative intensity being strongly dependent on composition [11-16]. The g≈4.27 resonance line is characteristic of isolated Fe^{3+} ions predominantly situated in rhombically distorted octahedral or tetrahedral oxygen environments. The g≈6.0 resonance line arises from axially distorted sites. According to Sperlich et al. [19] the micro vicinity of the Fe^{3+} ion is a distorted tetrahedron in the form of a roughly planar complex, the symmetry being low enough for justifying the g≈4.3 absorptions.

The g≈2.0 resonance is assigned to those ions which interact by a superexchange coupling and can be considered as distributed in clusters. According to Wickman et al.[17] in rhombic vicinities, besides the transition having a g≈4.3 isotropic value corresponding to the median Kramers doublet, there are transitions corresponding to the other two doublets characterized by g factors (9.678; 0.857; 0.607) having a pronounced anisotropy. These transitions result in a large background with effective g values from 1 to 10 as Griffith[18] pointed out.

4.2.1 $80TeO_2$-(20-x)ZnO- xFe_2O_3 glass system:

The room temperature (293K) and low temperature (123K) ESR spectra of the glass series $80TeO_2$- (20-x)ZnO-xFe_2O_3, where x = 5,10,15 and 20 are shown in figure 4.2.1 as (a) and (b) respectively. The resonance absorptions are due to Fe^{3+} ($3d^5$, $^6S_{5/2}$). All the compositions show the absorptions centred at g≈2.0 with a well evidenced shoulder around g≈4.27 for the sample 80T15Z5F. For x = 0, the initial composition $20ZnO80TeO_2$, is a diamagnetic, so no ESR data was taken for the sample.

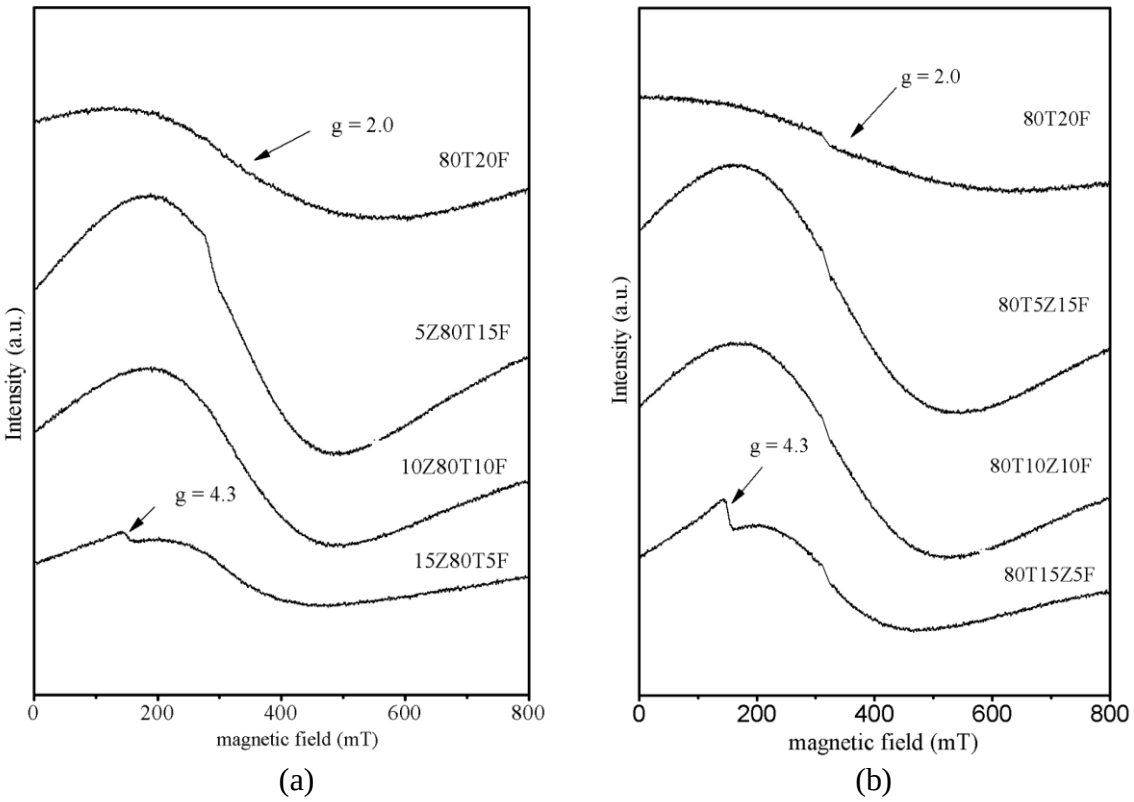

Fig 4.2.1. ESR spectra of $80TeO_2$-(20-x)ZnO- xFe_2O_3 at (a)RT and (b)133K

The other samples in the series, x=5, 10, 15 and 20 mol% of Fe_2O_3samples, the ESR spectra was recorded. From figure 4.2.1(a), at room temperature, the spectra for $80TeO_2$- (20-x)ZnO-xFe_2O_3 series show broad and symmetric signals which are characteristic of g=2.0. Similar kind of behaviour could be observed for the spectra at low temperature of 133K figure 4.2.1(b), with enhanced amplitude and well defined ESR resonance signal. This is because of the reduced thermal agitation at low temperatures.

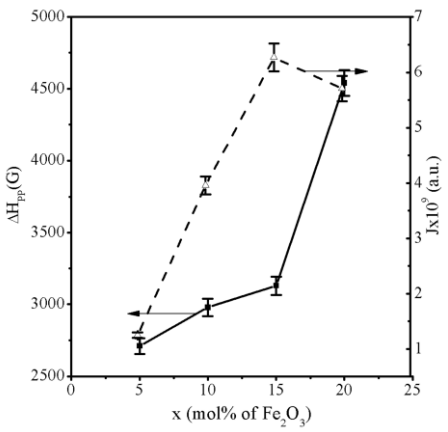

Fig 4.2.2 Fe_2O_3 Composition variation of linewidth and J of ESR absorption at room temperature

Table 4.2.Linewidth and no. of spins calculated from ESR spectra of the glass system

Sample	x (mol%)	ΔH_{pp} (±5mT)	N ($x10^{22}$ spins/kg) (±0.01)
15Z80T5F	5	271	1.14
10Z80T10F	10	298	3.1
5Z80T15F	15	313	4.46
80T20F	20	454	2.1

Figure 4.2.2 shows the composition dependence on the ESR parameters for g≈2.0 resonance, i.e. the linewidth, ΔH_{pp} and the intensity of the absorption line, $J = I(\Delta H_{pp})^2$. The ΔH_{pp} and J increases linearly as Fe_2O_3 content increases from 5 to 15mol%. Above 15 mol % of Fe2O3 a pronounced increase in ΔH_{pp} and no change in J are observed. These results results indicate that above 10 mol.% of Fe_2O_3, the iron enters in the glass matrix as Fe^{3+} as well as Fe^{2+} species. Fe^{2+} ions are not involved in the EPR absorption but their interactions with Fe^{3+} influence the characteristics of the absorption lines. The linewidth evolution of the g≈2.0 resonances may be explained having in view the clustered structure of iron giving rise to these absorptions. There are superexchange mechanisms narrowing the absorption line balanced over a certain doping degree by broadening mechanisms due to interactions between Fe^{3+} and Fe^{2+} ions.

The number of spins contributed for ESR spectra was calculated at room temperature using the equation (4.1), taking $CuSo_4$ as reference. Similar kind of behaviour was observed in some of the iron doped glasses [11, 13, 14, 21-26].

EPR spectra of various Fe_2O_3 glasses reported in the literature [12] consist of a narrow line at g ~ 4.2 ascribed to the isolated Fe^{3+} ions in sites of distorted octahedral symmetry (rhombic or tetragonal) subjected to strong crystal field effects and a broad linewidth (ΔH) ~ 1 kG at g ~ 2.0 characteristic of Fe^{3+} ions distributed in clusters such as dimmers or triads. The observed spectra are due to isolated Fe^{3+} ions, dimmers or triads.

In conclusion, the ESR spectra of the glass series $80TeO_2$- (20-x)ZnO-xFe_2O_3, where x = 5,10,15 and 20 is due to Fe^{3+} ($3d^5$, $^6S_{5/2}$) resonance absorptions. All the compositions show the absorptions centred at g ≈2.0, one remarks a well evidenced shoulder around g≈4.27 for the sample 80T15Z5F. The ESR spectra at room temperature show broad and symmetric signals at g ~ 2.0. The g≈2.0 absorption linewidth increases nonlinearly with Fe_2O_3 content. Fe ions enter the matrix besides Fe^{3+} as Fe^{2+} species too. Fe^{2+} ions are not involved in the EPR absorption but their interactions with Fe^{3+} influence the characteristics of the absorption lines. The line-width evolution of the g≈2.0 resonances may be explained having in view of the clustered structure of iron ion giving rise to these absorptions. There are superexchange mechanisms narrowing the absorption line balanced over a certain doping degree by broadening mechanisms due to interactions between Fe^{3+} and Fe^{2+} ions.

4.3. 20ZnO- (80-x) TeO_2- xFe_2O_3 glass system:

The room temperature (293K) and low temperature (123K) ESR spectra of the glass series20ZnO- (80-x) TeO_2- xFe_2O_3, where x = 0, 1, 3, 5 and 7 are shown in figures 4.3.1 (a) and (b) respectively. The resonance absorptions are due to Fe^{3+} ($3d^5$, $^6S_{5/2}$). In addition to the absorptions centred at g≈4.3 and g≈2.0 with a well evidenced shoulder around g≈9.79 for the sample 20Z79T1F. The existence of the g≈9.79 resonance accompanying the g≈4.3 resonance observed in the ESR spectra of 1 mol% Fe_2O_3 glass (figure 4.3.1 (a) and (b)) indicates a predominant rhombic character of the structural units involving the Fe^{3+} ions. With increase in Fe_2O_3 content, the intensity of g≈4.3 resonance suddenly decreases, becoming favoured by the absorptions at g≈2.0. The intensity of g≈2.0 absorption constantly increases as x increases from 1 to 7 mol%. The g≈4.3 resonances removal during the impurifying process is mainly due to destroying of the neighbours configuration in the iron ions vicinity. Although randomly distorted these vicinities are similar to each other having at the origin the same local order of oxides involved in preparing the vitreous matrix and the same ability of Fe^{3+} in ordering the surrounding. These structural units are the microagregates which assure the independence of the paramagnetic ions and their specificity of isolated ones. The gradual increasing of the paramagnetic ions density destroys the microstructural ordering in their

neighbourhood and these structural units as characteristic entities become less represented.

This restricted capacity of the matrix in accepting Fe^{3+} ions in structural units of well defined configuration and symmetry is typical for tellurite glasses due to the particularities of their structure [19, 20]. According to Sperlich et al. [19] the micro vicinity of the Fe^{3+} ion is a distorted tetrahedron in the form of a roughly planar complex, the symmetry being low enough for justifying the g≈4.3 absorptions.

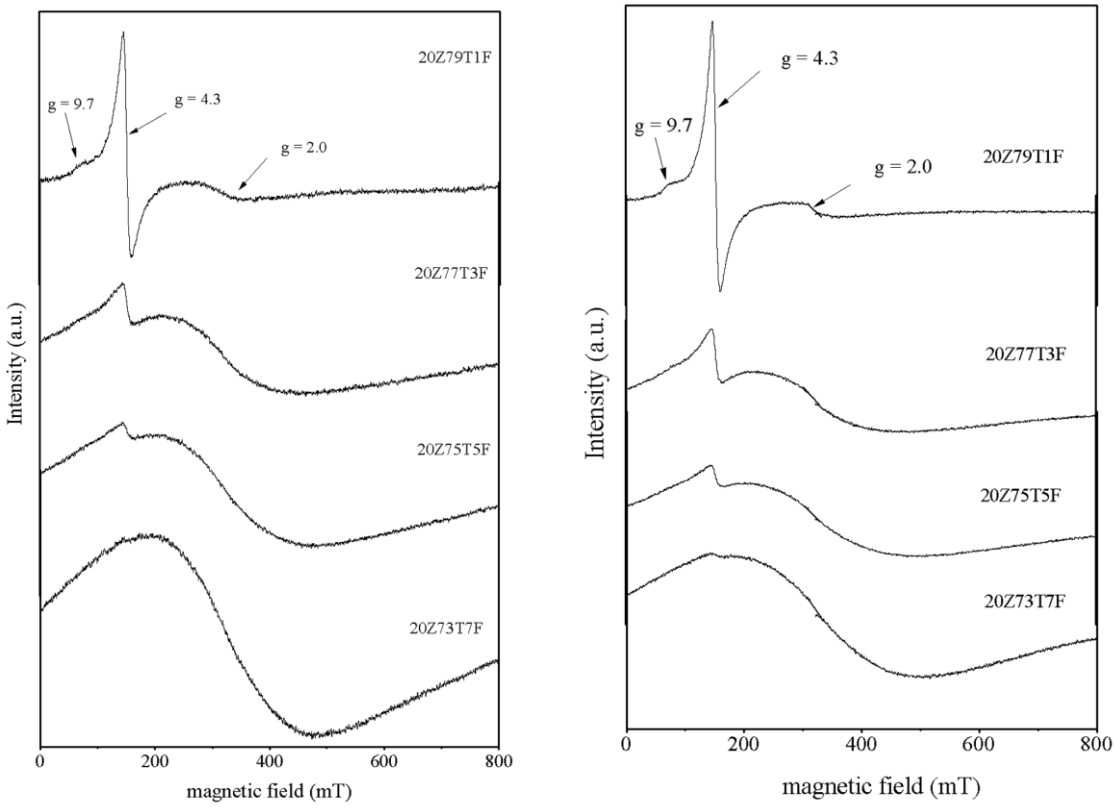

Fig 4.3.1 ESR spectra for 20ZnO(80-x)TeO_2xFe_2O_3 at (a)RT and (b) 123K

The base composition 20ZnO80TeO_2, is diamagnetic, so no ESR data could be taken for this sample. The ESR spectra were recorded the samples with x=1, 3, 5 and 7 mol% of Fe_2O_3. and are shown in figure 4.3.1(a), at room temperature. The spectra for 20Z79T1F shows a well-defined, symmetric signal with linewidth 15mT, H_r= 154.88mT with g= 4.2. A weak signal at Hr_2=314.54mT (g=2.1) and a small shoulder resonance towards lower field side of the major peak at g=4.2 were observed in the spectra. For the samples with x= 3, 5, and 7% of Fe_2O_3, a broad resonance signal at g= 2.1 is observed.

For 3F and 5F samples, a weak resonance at g= 4.2 is also observed alongwith a broad resonance centered at g ~ 2. Similar kind of behaviour could be observed from the figure 4.3.1 (b) with enhanced amplitude and more well defined resonance peak positions in spectra recorded at low temperature of 133K because of reduced thermal agitations.

Figure 4.3.2 shows the composition dependence on the EPR parameters, i.e. the line-width, ΔH_{pp} and the intensity of the absorption line, J, approximated as $J = I(\Delta H_{pp})^2$. The concentration dependence of these parameters is plotted in figure 4.3.2 for the absorption centred at g≈2.0. The composition dependence of the g≈2.0 absorptions linewidth is increasing which does not follow linearly the Fe_2O_3 content. From 3 mol.% Fe_2O_3 for the studied glasses, over which the iron enters in the matrix besides Fe^{3+} as Fe^{2+} species too. Fe^{2+} ions are not involved in the EPR absorption but their interactions with Fe^{3+} influence the characteristics of the absorption lines. The linewidth evolution of the g≈2.0 resonances may be explained having in view the clustered structure of iron giving rise to these absorptions. There are superexchange mechanisms narrowing the absorption line balanced over a certain doping degree by broadening mechanisms due to interactions between Fe^{3+} and Fe^{2+} ions.

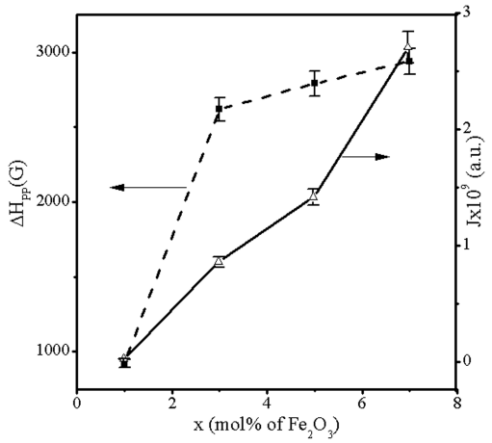

Fig 4.3.2 Fe_2O_3 composition dependence of linewidth and J for g=2.0 resonance

Table.4.3. Linewidth and no. of spins calculated from ESR spectra for $20ZnO(80-x)TeO_2xFe_2O_3$ glass system

Sample	x (mol%)	ΔH_{pp} (±5mT)	N ($x10^{21}$ spins/kg) (±0.01)
20Z79T1F	1	92	1.38
20Z77T3F	3	262	9.73
20Z75T5F	5	279	13.15
20Z73T7F	7	294	21.8

Fig 4.3.3 shows the temperature variation of the ESR spectra for 20Z79T1F sample in the temperature range 133-323K. There is no significant change in ΔH_{pp} of g=4.2 resonance. However, its intensity increases as the temperature decreases. The number of spins estimated using equation (4.1), taking $CuSo_4$ as reference. Similar kind of behaviour has been reported in some other iron doped glasses [11, 13, 14, 21-26].

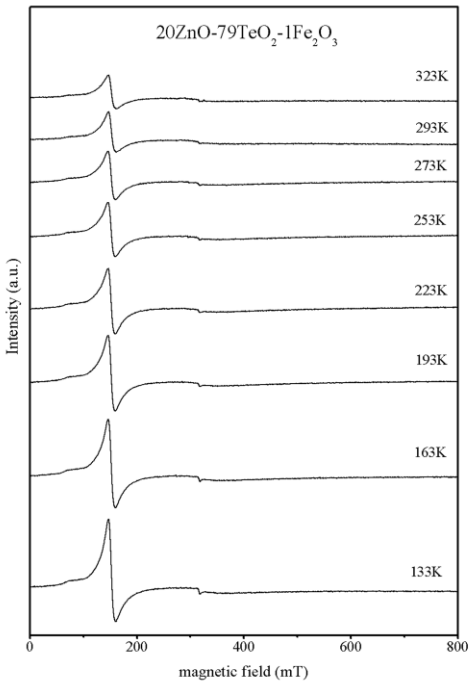

Fig 4.3.3 Temperature variation of ESR spectra for 20Z79T1F

In conclusion, the ESR spectra of the glass series 20ZnO- (80-x) TeO_2- xFe_2O_3, where x = 0, 1, 3, 5 and 7 are from the resonance absorptions which are due to Fe^{3+} ($3d^5$, $^6S_{5/2}$) [11]. In addition to the absorptions centred at g≈4.3 and g≈2.0, a well evidenced shoulder around g≈9.79 is observed for the sample 20Z79T1F indicating a predominant rhombic character of the structural units involving the Fe^{3+} ions. With increase in Fe_2O_3 content, the intensity of g≈4.3 resonance suddenly decreases and gives rise to absorptions at g≈2.0. The intensity of g≈2.0 absorption increases as Fe ion concentration increases at the expense of g≈4.3 resonance. The disappearance of g ≈ 4.3 resonances is mainly due to destruction of the neighbours configuration in the iron ions vicinity. These structural units are the microagregates which assure the independence of the paramagnetic ions and their specificity of isolated ones. The gradual increasing of the paramagnetic ions density destroys the microstructural ordering in their neighbourhood and these structural units as characteristic entities become less represented.

4.4. 10 Fe_2O_3-(90-x)TeO_2-xBi_2O_3 glass system:

The room temperature(293K) and low temperature (133K) ESR spectra of the glass series 10Fe_2O_3-(90-x)TeO_2-x Bi_2O_3, where x = 0,5,10,15 and 20 are shown in figure 4.4.1(a) and (b) respectively. All the compositions show broad resonance centred at

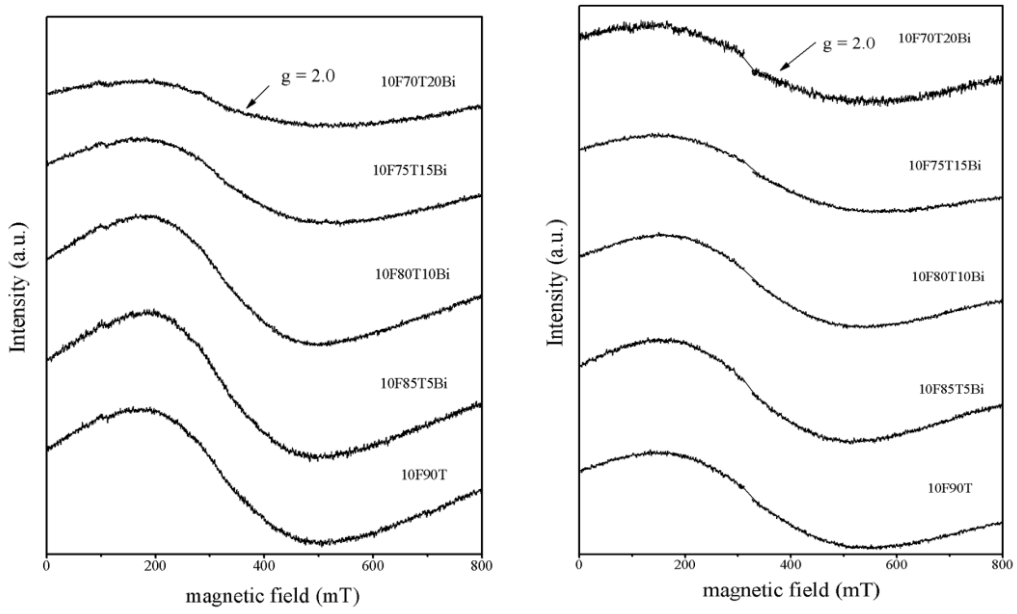

Fig 4.4.1. ESR spectra of 10Fe_2O_3-(90-x)TeO_2-x Bi_2O_3 at (a) RT and (b) 133K

g≈2.0 with resonance field ΔH_{pp} = 325 ± 25 mT. Similar kind of behaviour could be observed from the figure 4.4.1 (b) at 133 K. The J value decreases with increase in Bi_2O_3 content. With addition of Bi_2O_3, the oxidation state of Fe ions will vary and more number of Fe^{3+} ions will be converted into Fe^{2+} ions. The antiferromagnetic interaction between Fe^{3+} and Fe^{2+} will increase leading to decreasing trend in intensity of ESR absorption with increase in Bi_2O_3 content.

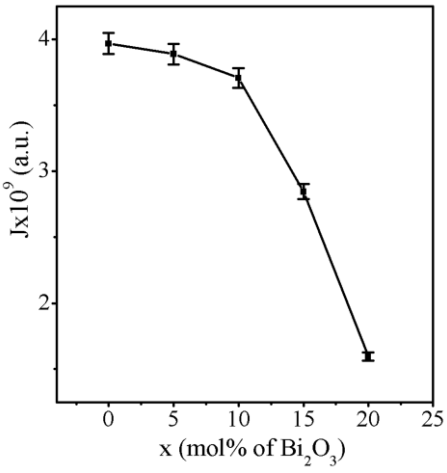

Fig 4.4.2 Bi_2O_3 composition variation of intensity J of ESR absorption curve for the glass system at room temperature

4.5. 20 Fe_2O_3-(80-x)TeO_2-x Bi_2O_3 glass system:

The room temperature(293K) and low temperature (133K) ESR spectra of the glass series $20Fe_2O_3$-(80-x)TeO_2-x Bi_2O_3, where x = 0,5,10,15 and 20 are shown in figure 4.5.1 (a) and (b) respectively. All the compositions show the absorptions centred at g≈2.0 with ΔH_{pp} = 360 ± 25 mT.

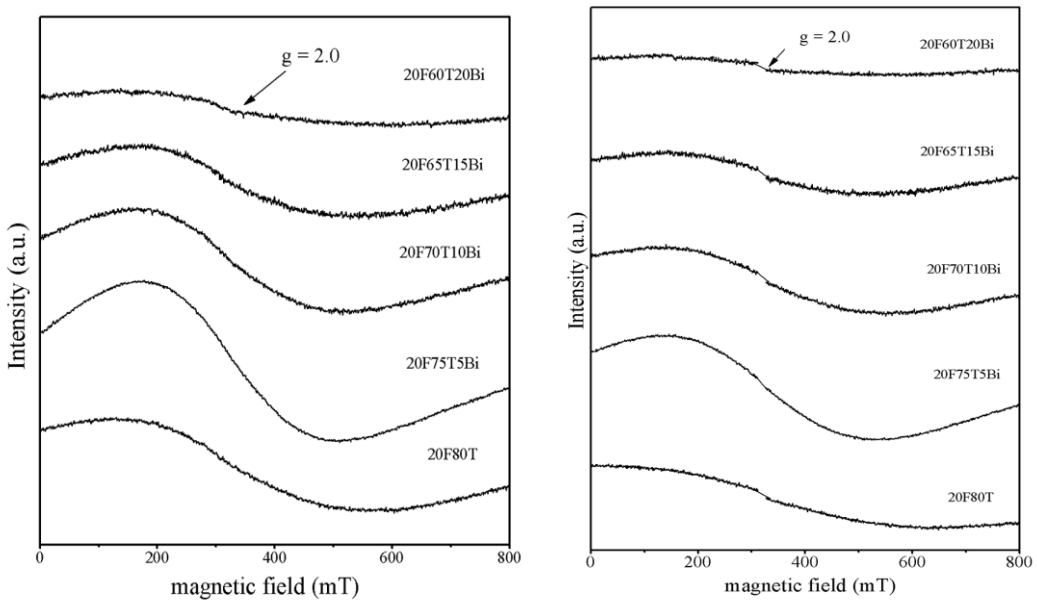

Fig 4.5.1. ESR spectra of 20 Fe_2O_3-(80-x)TeO_2-x Bi_2O_3 at (a) RT and (b) 133K

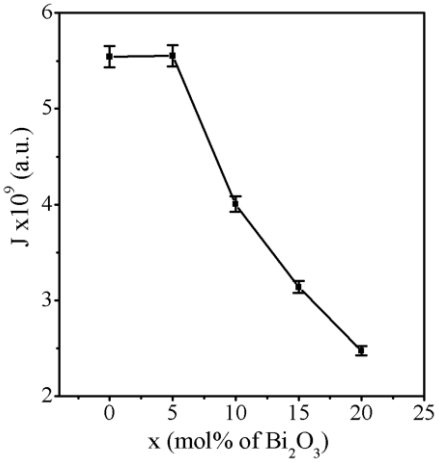

Fig 4.5.3. Bi_2O_3 composition variation of intensity J of ESR absorption curve for the glass system at room temperature

The intensity of the absorption line, J is higher for this series compared to the earlier series because of higher Fe_2O_3 content. With the addition of Bi_2O_3, the Fe^{3+} ions convert into Fe^{2+} ions leading to increased antiferromagnetic interaction and decrease in J value. In iron- tellurite glasses the isolated Fe ions are not detected. All Fe ions are coupled antiferromagnetically in the form of clusters (dimmer or triads). The addition of Bi_2O_3 does not change the cluster formation and create isolated Fe ions.

4.6. (100-x)(70 Bi_2O_3 20 ZnO 10 PbO) - xFe_2O_3 glass system:

The room temperature ESR spectra of the series (100-x)(70 Bi_2O_3 20 ZnO 10 PbO) - xFe_2O_3 , where x= 5,10,15,20 and 25 coded as BZPF5, BZPF10, BZPF15, BZPF20 and BZPF25 are shown in figure 4.6.1. The samples BZPF5 and BZPF10 show a single resonance peak at g ~2, with linewidth (ΔH) ~ 29 mT and 34 mT respectively. Whereas the ESR spectra of BZPF15, BZPF20 and BZPF25 consists of a resonance at g ~2 accompanied by another peak towards lower field side with the total linewidth (ΔH) ~ 81mT, 98 mT and 148 mT respectively. The ΔH is estimated as the total peak to peak separation between minima and maxima of the resonance line as shown in the relevant figures.

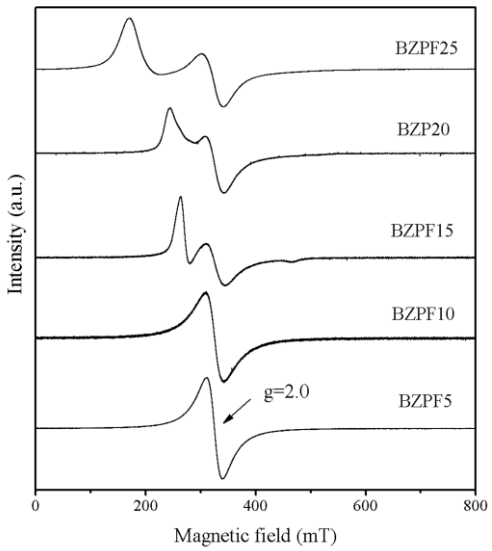

Fig.4.6.1. ESR spectra of (100-x)(70 Bi_2O_3 20 ZnO 10 PbO) - xFe_2O_3 at RT

The extensive temperature dependent ESR studies are carried out in the temperature range 123 – 473 K to understand the underlying magnetic interactions and spin dynamics for all the compositions in this series of glass samples.

Figures 4.6.2 and 4.6.3 show temperature dependent ESR spectra for BZPF5 and BZPF10 respectively. The variation of ΔH and 1/DI with temperature for these samples are shown in figures 4.6.4 and 4.6.5.

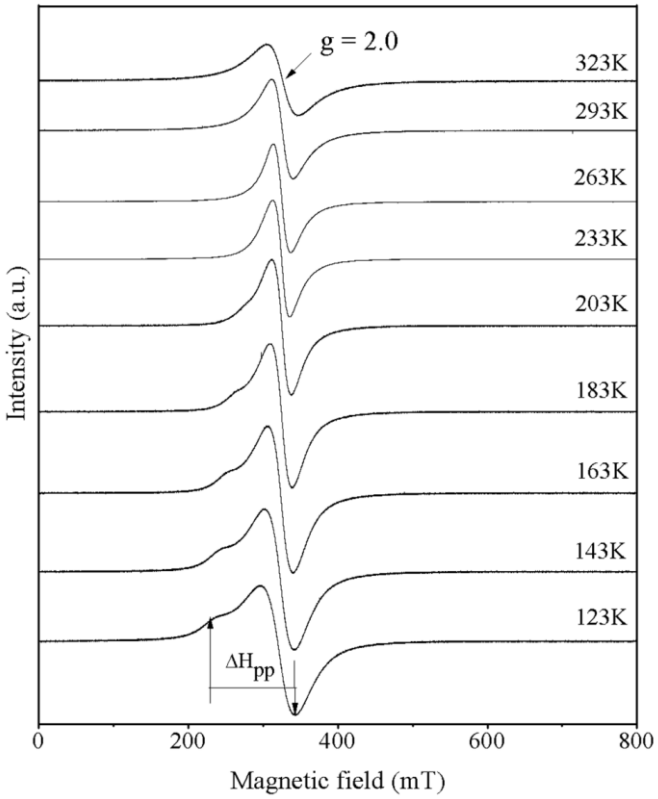

Fig 4.6.2. Temperature variation of ESR spectra for BZPF5

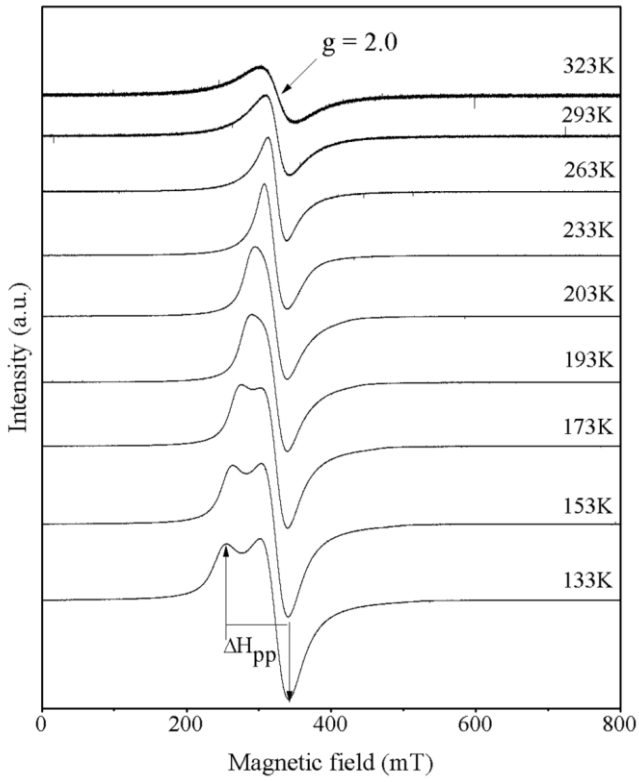

Fig 4.6.3. Temperature variation of ESR spectra for BZPF10

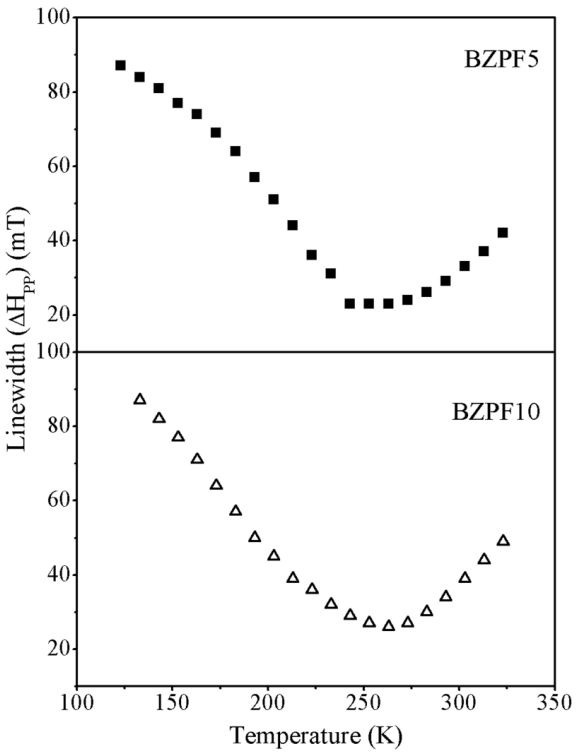

Fig 4.6.4. ΔH_{PP} vs. T plots for BZPF5 and BZPF10

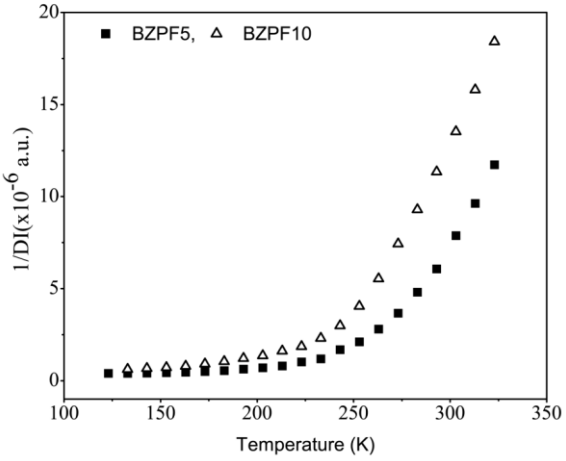

Fig 4.6.5. 1/DI vs. T plots for BZPF5 and BZPF10

For both the samples the ESR spectra consist of a narrow resonance at g ~ 2 at high temperature. A second resonance appears and progressively shifts towards lower field (high g value) as the temperature decreases. The ΔH decreases with decrease in temperature, reaches a minimum value and increases with further decrease in temperature. The ΔH value is minimum at 203K and 263K for BZPF5 and BZPF10 samples respectively. The 1/DI vs T is linear in the high temperature region, 213-323K and exhibits saturation at low temperature indicative of ferromagnetic phase ordering.

The intercept on the temperature axis of linear fits of 1/DI vs. T plots gives the Curie temperature of 216K and 209K for BZPF5 and BZPF10 samples respectively. These values are close to the temperature where the shoulder resonance peak in the ESR spectra of these samples emerges.

The temperature dependent ESR spectra for the samples BZPF15, BZPF20, BZPF25 in the temperature range between 123 -473K are shown in figures 4.6.6, 4.6.7 and 4.6.8 respectively. The variation of ΔH and 1/DI with temperature are shown in figures 4.6.9 and 4.6.10

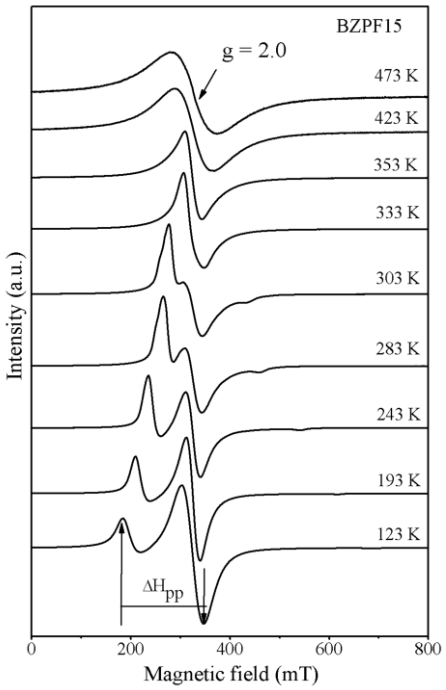

Fig 4.6.6. Temperature variation of ESR spectra for BZPF15

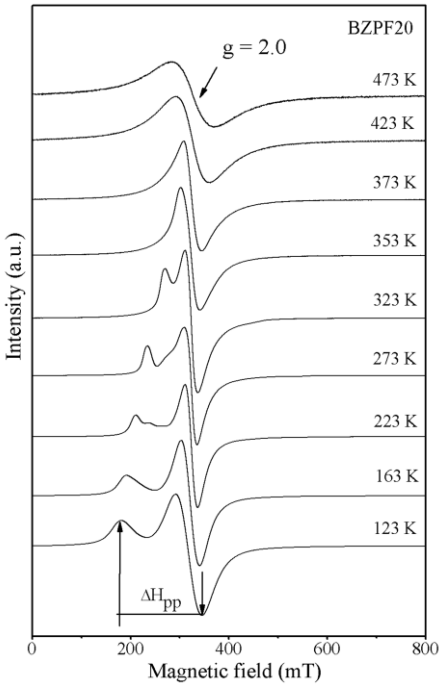

Fig 4.6.7. Temperature variation of ESR spectra for BZPF20

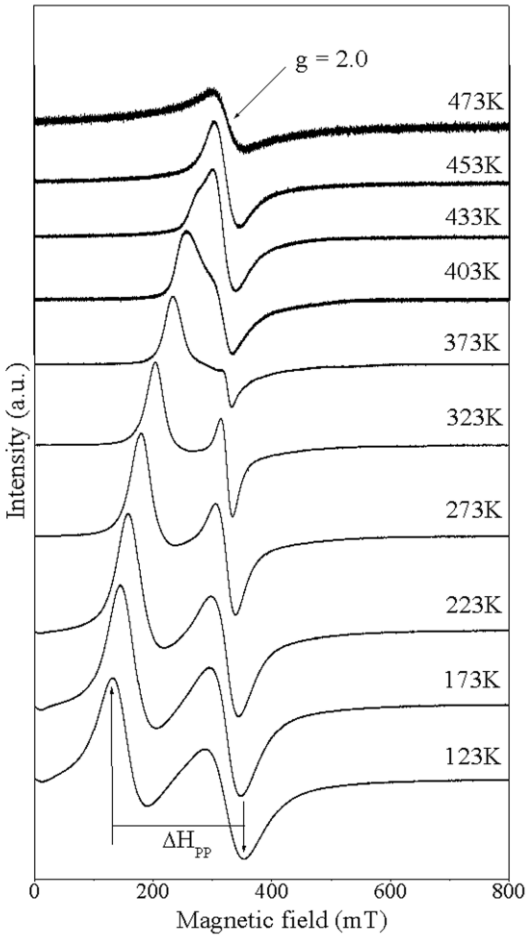

Fig 4.6.8. Temperature variation of ESR spectra for BZPF25

.

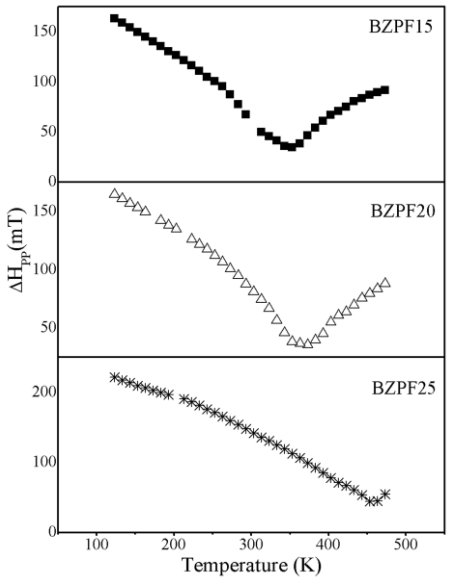

Fig 4.6.9. ΔH_{PP} vs. T plots for BZPF15, BZPF20 and BZPF25

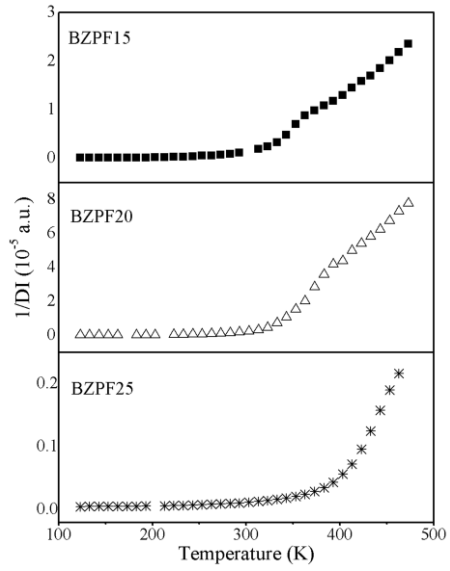

Fig 4.6.10. 1/DI vs. T plots for BZPF15, BZPF20 and BZPF25

As evident from figures 4.6.6-4.6.8, the ESR spectra consists of a resonance at g ~ 2. As the temperature decreases, the single resonance splits and a second resonance emerges at ~ 333K, ~353K and ~ 443K for the samples BZPF15, BZPF20 and BZPF25 respectively. The ΔH first decreases with temperature, reaches a minimum value and then increases with further decrease in temperature reaching a value of ~87mT, 92mT, 170mT, 172mT and 221mT at 123K for BZPF5, BZPF10, BZPF15, BZPF20 and BZPF25

samples respectively. The ΔH value is minimum at 343K, 363K and 453K for BZPF15, BZPF20 and BZPF25 samples. The 1/DI vs. T are linear in the high temperature with a Curie temperature of 252K, 254K and 381K for the samples BZPF15, BZPF20 and BZPF25 respectively.

Discussion:

For all the samples, the spectra at high temperatures consist of a narrow resonance at g ~ 2. As the temperature decreases, the single narrow peak splits at a temperature, T_f. As the temperature decreases further, the second peak shifts to lower field side. The total linewidth increases with decreasing temperature. The variation of 1/DI vs. T plot is linear in the high temperature region, but at lower temperatures it exhibits curvature and saturation indicating the presence of ferromagnetic magnetic clusters. From the linear portion of 1/DI vs. T, the high positive value of intercept (Curie temperature) on the temperature axis is obtained.

The EPR spectra of various Fe_2O_3 glasses reported in the literature [12] consist of a narrow line at g ~ 4.0 ascribed to the isolated Fe^{3+} ions in sites of distorted octahedral symmetry (rhombic or tetragonal) subjected to strong crystal field effects and a broad line with (ΔH) ~ 1 kG at g ~ 2.0 characteristic of Fe^{3+} ions distributed in clusters such as dimmers or triads. The observed spectra cannot be due to isolated Fe^{3+} ions, dimmers or triads but it is a typical signature of superparamagnetic nanoparticles embedded in the glass matrix and has been recently observed in a number of systems e.g. [31, 33, 35, 36]. In the as cast glass sample the clusters of nanoparticles exist and they align in one direction giving rise to ferromagnetic (FM) phase formation with decrease in temperature as reflected in the appearance of resonance at g > 2 and its progressive shift towards lower field (higher g value) with decrease in temperature. The cluster size and shape plays a role in the shape of the ESR spectra. The observed spectra are a typical signature of superparamagnetic nanoparticles embedded in the glass matrix. The observed ESR spectra have been analysed in view of the theoretical models developed for systems containing magnetic clusters.

Raikher and stepanov [37] in their 'independent-superparamagnetic grain' model for solid ferro-composites has predicted peculiar two-peak FMR structure. The main features of this model are

- The theory of FMR in a dilute suspension of magnetically anisotropic particles subjected to the action of strong constant and weak oscillating fields is developed in the framework of the effective-field approximation. The particles are assumed to be ultrafine (several nanometers in size), hence single-domain and considerably influenced by superparamagnetism.
- Under these circumstances the shape of the FMR absorption line is determined as an interplay of two main mechanisms: thermofluctuational motion of the particle magnetic moment (homogeneous broadening) and orientational spreadout of the particle anisotropy axes (inhomogeneous broadening).

The model predicts, a two-maxima absorption curve for which the conventional FMR characteristics —linewidth and resonance field—must become double valued.

In the customary FMR technique the spectrometer frequency is fixed (or switched stepwise by a very few constant values), and the dynamic susceptibility is recorded as a function of the strength and direction of the quasistatically varied external field H. In solid samples the change of H usually does not affect the intrinsic distribution of H_a (strength of anisotropy field). But magnetic suspensions (magnetic fiuids) make an exception. There, due to the fact that, being afloat in the liquid matrix the grains retain their orientational mobility, the angular distribution of the anisotropy axes reacts to the change of the external field. Apparently, the effect is the more pronounced the stronger is the magnetic anisotropy of the particles.

The variation of the anisotropy axis distribution in response to the applied external field is considered to predict FMR in suspensions of magnetically anisotropic single domain particles. The basic assumptions are.

(i) The anisotropy field $H_a \sim K/I_s$, of the particle (here K is the magnetic anisotropy energy density, I_s, is the magnetization of the particle substance) satisfies the condition $\gamma H_a / \omega < 1$, where γ is the gyromagnetic ratio, and ω is the spectrometer frequency. Since usually $\omega/2\pi \sim 10$ GHz, the above-presented restriction holds for $H_a < 10^3$ Oe which is the

case for the majority of ferri- or ferromagnets used in preparation of magnetic suspensions.

(ii) The probing high-frequency field h (it is imposed perpendicular to the magnetizing one H) is small enough to comply with the condition $\mu h/k_BT \ll 1$, where $\mu = I_sV$ is the magnetic moment of a single-domain particle with the volume V, and k_BT is the temperature measured in energy units. Since the strength of the probing field scarcely exceeds 1 Oe, the last inequality may break down either at very low temperatures or for rather large particles. Both limits are of minor interest for the present study, because at low temperatures the suspension could hardly retain fluidity, whereas large particles cannot be really suspended (stabilized against sedimentation).

FMR ABSORPTION LINES IN A MAGNETIC SUSPENSION

The model considers three quantities, viz. , $\gamma\mathbf{H}/\omega$, ξ_0, and ε, which make a convenient set of material parameters to describe the FMR spectra. Here, $\xi_0 = \mu\omega/\gamma k_BT$, which is the field-independent parameter and $\varepsilon=\sigma/\xi_0=\gamma K/\omega I_s$, a field and temperature-invariant measure of the particle anisotropy, where $\sigma = KV/k_BT$, is anisotropy parameter. Figure 4.6.11 shows how the FMR spectra changes with decrease in temperature.

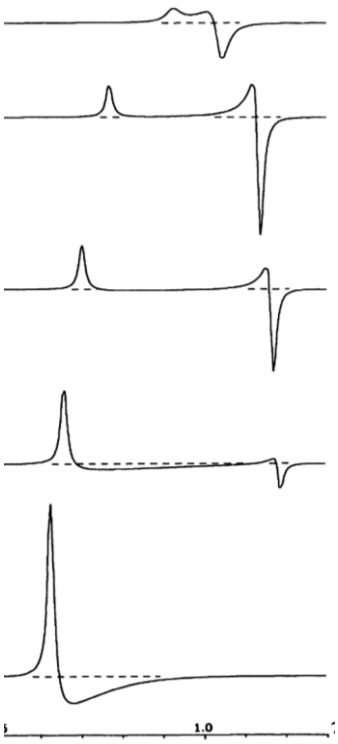

Fig. 4.6.11. predicted FMR spectra with decreasing temperature. Dashed lines mark the corresponding zero levels.

These details of the behavior of the absorption lines are reflected in the conventional characteristics of FMR, i.e., the resonance field H_r and linewidth ΔH, both of which are defined with the aid of $d\chi''/dH$ graphs. The set of curves presenting function $H_r(\xi_0)$ is shown in Fig.4.6.12.

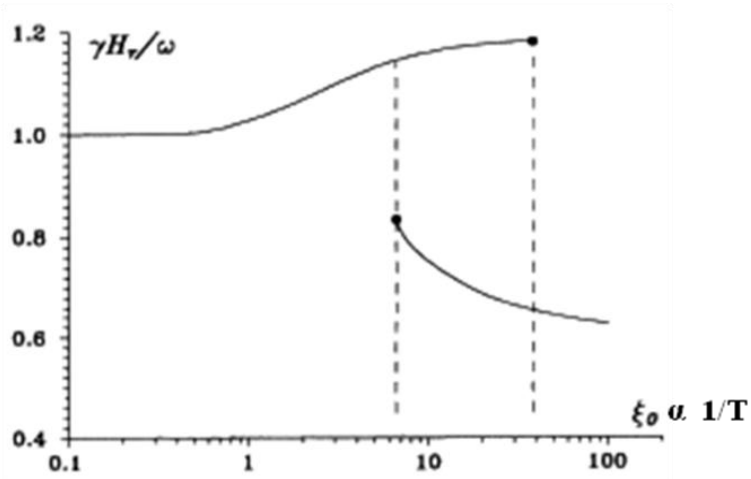

Fig. 4.6.12. Dependences of the positions of the peaks of the absorption line (resonance field H_r) on the parameter $\xi_0 \propto 1/T$

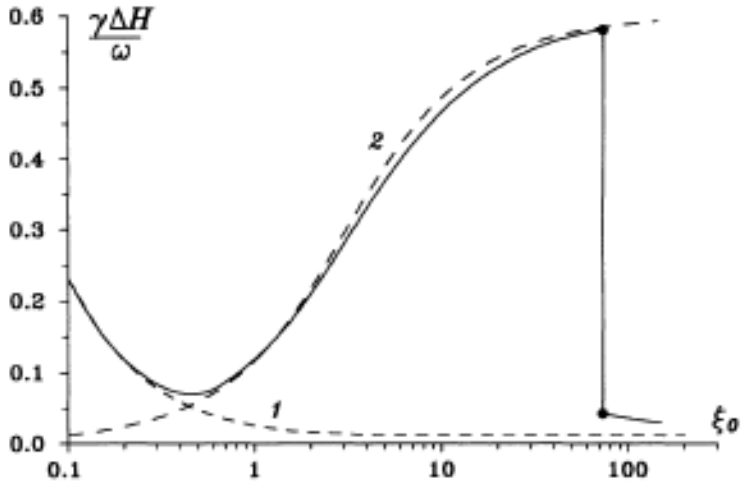

Fig. 4.6.13. ΔH variation with decreasing temperature.

The linewidth $\Delta H(\xi_0)$ is shown in Fig. 4.6.13 together with its asymptotics. Both the high- and low-temperature ones (dashed line 1) which give $\Delta H = 4\alpha\omega/\sqrt{3}\gamma\ \xi_0$ at $\xi_0 \ll 1$, and $\Delta H = 2\alpha\omega/\sqrt{3}\gamma$ for $\xi_0 \gg 1$.

Thus we see that for the absorption curves with two peaks whose heights change gradually, dominating in turn under increase-decrease of ξ_0 (inverse temperature), both ΔH and H_r lose their customary single valuedness.

Using the above model various plots of ESR data on the present glass samples are shown in the following figures 4.6.14 and 4.6.15.

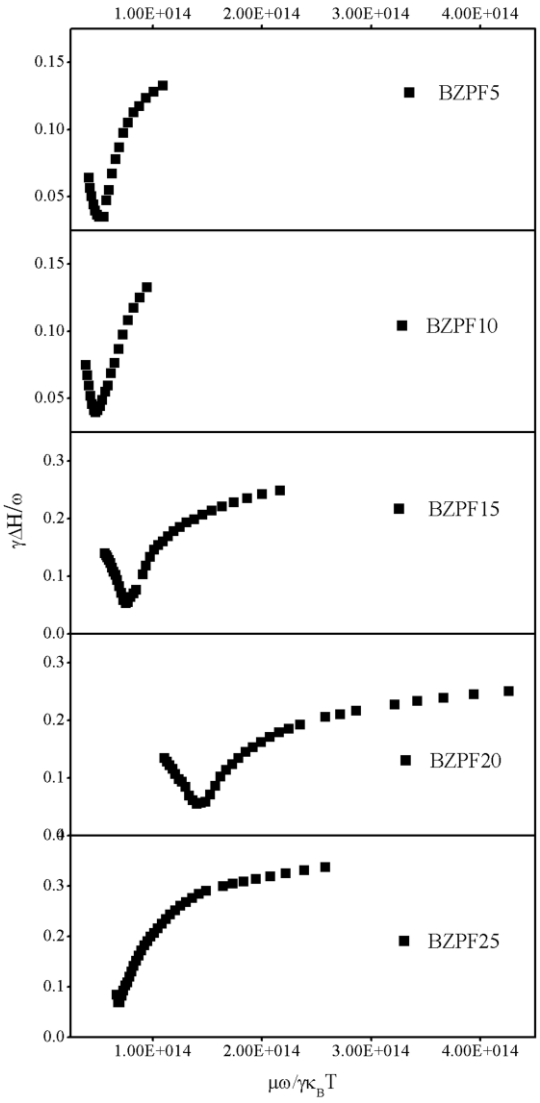

Fig.4.6.14. plots of $\gamma\Delta H/\omega$ vs. $\mu\omega/\gamma\kappa_B T$

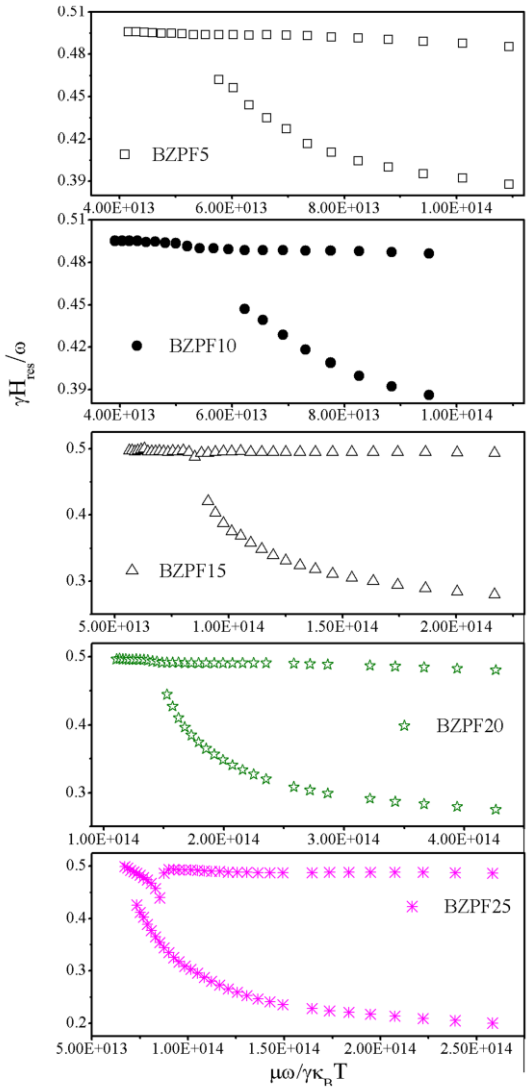

Fig.4.6.15. plots of $\gamma H_r/\omega$ vs. $\mu\omega/\gamma\kappa_B T$

The ESR data shows the formation of superparamagnetic clusters in the present glass system (100-x)(70 Bi_2O_3 20 ZnO 10 PbO) - xFe_2O_3.

The temperature at which the second resonance emerges depends on the size and shape anisotropy of the magnetic particles inside the glass network. The shape of the clusters also plays a role in the shape of ESR spectra as per the theorical model developed by de Biasi [35]. According to this model the ESR spectra in the present glass system arises from the magnetic nanoparticles having prolate ellipsoid shape.

In conclusion, for the glass system (100-x)(70 Bi_2O_3 20 ZnO 10 PbO) - xFe_2O_3, the ESR spectra is characteristic of magnetic nanoclusters embedded in the glass matrix. The

temperature at which the single narrow peak splits is dependent on size and shape of the magnetic nanoparticles. The experimental ESR spectra have been found to be in excellent agreement with theoretically computed spectra.

References:

[1] R.S. de Biasi, t.C. Devezas, *J. Appl. Phys*. **49**, 2466 (1978).

[2] R. Berger, J.C. Bissey, J. Kliava, H.Daubric and C.Estournes, *J. Mag. Mag. Mat.* **234** 535 (2001).

[3] I. Ardelean, G. Ilonca and M. Peteanu, *J. Non-Crys. Solids* **51** 389-393 (1982).

[4] I. Ardelean, O. Cozar and Gh. Ilonca, *Solid State Commun.* **50** 87 (1984).

[5] F. Criocas, S. K. Mendiratta, I. Ardelean and M. A. Valente *Eur Phys J B* **20** 235-240 (2001).

[6] P. Sandhya Rani and R. Singh, *J. Mater. Sci*. **45** 2868-2873 (2010).

[7] I. Ardelean and R. Ciceo Lucael, *Phys. Chem. Glasses*, **46(5)** 491-493 (2005).

[8] M.A. Hassan, C.A. Hogarh, and K.A.K. Lott, *J. of Mater. Sci*. **24** 1645-1647.7 (1989).

[9] I. Ardelean, M. Peteanu, E. Burzo, F.Ciorcas and S. Filip, *Solid State Communications*, **98** 351-355 (1996).

[10] J.A. Weil, J.R. Bolton, J.E. Wertz, *electron Paramagnetic Resonance – Elementary Theory and Practical Applications*, *Wiley, New York*, p. 498 (1994).

[11] P. Sandhya Rani and R. Singh *J Phys & Chem Solids* **74** 338-343 (2013).

[12] I. Ardelean, G. Salvan, M. Peteanu, V. Simon, C. Himcinschi and F. ciorcas, *Mod. Phys. Lett. B*, **13**, 801-808 (1999).

[13] I. Ardelean and S. Filip *J Optoelectronics and Advd Matrls* **5**:157-169 (2003).

[14] S. Simon, R. Pop, V.Simon and M.Coldea, *J. Non-Crys. Solids* **331**, 1-10 (2003)

[15] Rajendra Kumar Singh, G.P. Kothiyal and A. Srinivasan, *J. Non-Crys. Solids* **354**, 3166-3170 (2008).

[16] Shiv Prakash Singh, R.P.S. Chakradhar, J.L. Rao and Basudeb Karmakar, *J. Alloys Compd* **493**, 256-262 (2010).

[17] H. H. Wickman, M. P. Klein and D. A. Sirley *J. Chem. Phys*., **42**, 2113 (1965).

[18] J.S. Griffith, *Molec. Phys.*, **8**, 213 (1964).

[19] G.Sperlich and P. Urban *Phys. Status Solidi (B)* **61**, 475 (1974).

[20] E. J. Friebele, N.C. Koon, L.K. Wilson and D.L. Kinser., J. Amer. Ceram. Soc., **57**, 237 (1974).

[21] I. Ardelean, M. Peteanu, S.Filip, V. Simon and G.Gyorffy, *Solid State Communications*, **102**, 341-346 (1997).

[22] I. Ardelean, Hong-Hua Qiu and H. Sakata, *Materials Letters*, **32**, 335-338 (1997).

[23] E. Burzo and I Ardelean, *Phys. Stat. Sol. (B)* **87** K137 (1978).

[24] R. Stefan and S. Simon, *Modern Physics Letters B*, **15** 111-117 (2001).

[25] R. Singh, *J. Phys. D: appl. Phys.*, **17 L** 163-L167 (1984).

[26] K. Tanaka, K. Kamiya and T. Yoko, S. Tanabe, K. Hirao and N. Soga, *Phys. and Chem. Glasses* **32** 16 (1991).

[27] P. Sandhya Rani and R. Singh, *AIP Conf. Proc*. **1447** 553 (2012).

[28] P. Sandhya Rani and R. Singh, *Solid State Phys (India)* **54**, 493 (2009).

[29] Katsuhisa Tanaka, Hirofumi Akamatsu, Seisuke Nakashima and Koji fujita, *J. Non-Crys.Solids* **354**, 1346 (2008).

[30] I.S. Edelman, T.V. Zarubina, S.A. Stepanov and T.A. Kim, *J. Mag. Mag. Mat.* **110,** 99-102 (1992).

[31] Rene Berger, Jean-Claude Bissey, Janis Klaiva and Benoit Soulard, *J. Mag. Mag. Mat.* **167,** 129-135 (1997).

[32] R.S. de Biasi and T.C. Devezas, *J. Appl. Phys*. **49**, 2466 (1978).

[33] R. Berger, J.C. Bissey, J. Kliava, H.Daubric and C.Estournes, *J. Mag. Mag. Mat*. **234** 535 (2001).

[34] J. Smit and H.G. Beljers, *Phillips Res. Rept*. **10**, 113 (1955).

[35] E. de Biasi, C.A. Ramos and R.D. Zysler, *J. Mag. Mag. Mat*. **262**, 235-241 (2003).

[36] Yu.A. Koksharov, S.P. Gubin, I.D. Kosobudsky, G.Yu. Yurkov, D.A. Pankratov, L.A. Ponomarenko, M.G. Mikheev, M. Beltran, Y. Khodorkovsky and A.M. Tishin, *Physical Review B*, **63**, 012407 (2000).

[37] Yuri L. Raikher and Victor I. Stepanov *Phy. Rev. B* **50**, 6250 (1994).

Chapter 5

Magnetization studies

Magnetic measurements are very useful for determining structural distribution of transition metal ions, their valence states and the type of interactions between them in the glass matrix. The magnetic susceptibility of oxide glasses containing transition metal (TM) ions provide information about magnetic interactions of TM ions related to the glass network structure. An indication of the magnetic character of a material can be obtained from the measurements of the linear magnetic susceptibility,χ as a function of temperature, T, according to the Curie-Weiss equation [1]

$$\chi = \frac{M}{H} = \frac{C}{T - \theta_p}, \tag{5.1}$$

where M is the magnetization at a given field, H, C is the Curie constant and θ_p is the Curie temperature. A negative value of θ_p indicates antiferromagnetic interactions, while a positive value implies ferromagnetic and zero indicates the material is paramagnetic in nature. The magnetization studies were carried out on the synthesized series of glass samples listed in chapter 2. Magnetic moment, Curie temperature, Curie constant, effective magnetic moment etc., were estimated from the magnetization studies of the glass samples.

The magnetization studies were done using Lake Shore Cryotronics Magnetometer model 7400 in the temperature range 80-300K in a filed of 10 kOe. The samples were initially cooled in zero external field and magnetization per unit gram values were measured at H = 10 kOe as the samples were warmed up to room temperature.

5.1. Copper tellurite glass system:

M vs. T plots for various glass samples are shown in fig.5.1.1. Magnetic moment decreases with increase in temperature and increases with increase in CuO content in the glass composition. Inverse of susceptibility (χ^{-1}) versus temperature plots for various

glass compositions are shown in fig.5.1.2. The paramagnetic susceptibility of the glass increases with increase in CuO content.

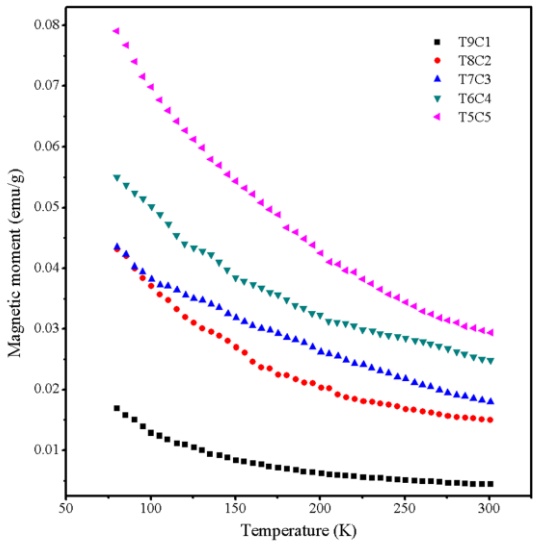

Fig 5.1.1. M vs. T for (100-x)TeO_2-xCuO glass system, where x = 10, 20, 30, 40 and 50

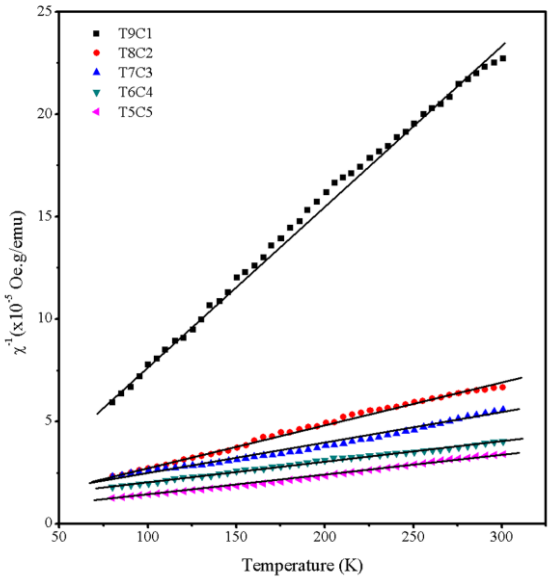

Fig 5.1.2. H/M vs. T for (100-x)TeO_2-xCuO glass system, where x = 10, 20, 30, 40 and 50

Temperature dependence of the reciprocal magnetic susceptibility of paramagnetic materials shows Curie-Weiss type behaviour as per eq. (5.1). The solid lines in fig.5.1.2 represent the least square fit to eq. (5.1). The negative paramagnetic Curie temperature obtained for the glasses indicate superexchange magnetic interactions between the copper ions in the glass which are predominantly anti-ferromagnetically coupled. The vitreous

oxide structure imposes the short-range character of magnetic interaction and enhances the structural image of clusters. Analysis of the present data show that the copper ions in the present glass matrix behave magnetically similar to copper ions in other glasses reported in ref. [2-5].

The magnetization per unit field, molar curie constant, C_M and the effective magnetic moments, μ_{eff}, are calculated and listed in table 5.1. The μ_{eff} values are estimated using the relation $\mu_{eff} = 2.828(C_M/x)^{1/2}$ assuming that all copper ions introduced in the sample contribute to the magnetic moment of glass. The μ_{eff} values obtained for all samples are lower than the magnetic moment of the free ion ($\mu_{Cu}^{2+} = 1.73\mu_B$) indicating the presence of both Cu^{2+} and Cu^{+} ions in these glasses. Cu^{+} ion is diamagnetic in nature and does not contribute to magnetic moment. Using the relation $\mu_{Cu}^{2+} = 2.828(C_M/y)^{1/2}$, we estimated to a first approximation the molar fraction of the Cu^{2+} ions (y) that contribute to the magnetic moment and listed in table 5.1. For all compositions, the molar fraction of the Cu^{2+} is lower compared to the molar faction of CuO in the vitreous samples. The concomitant presence of monovalent and divalent copper ions is reported in copper containing tellurite glasses [2-4].

The present study shows that as CuO increases from 10 to 20 mol% there is a sudden change in the properties of glass followed by gradual variation with further increase in CuO content. These changes may be related to the structural changes in the glass matrix with increasing CuO content. The TeO_2-rich glasses are characterized by TeO_4 building units. Both Te-O_{ax} axial bonds in theTeO_4 polyhedra are strongly dynamic and easily attacked by the modifier. When a modifier oxide is introduced in the glass matrix, one of the Te-O_{ax} bonds in TeO_4 polyhedra undergoes elongation. The introduction of a modifier in the binary glass leads to a $TeO_4 \rightarrow TeO_{3+1}$ transition. The number of TeO_{3+1} units is limited by modifier addition. With increase in modifier content the TeO_{3+1} units transform into TeO_3 and TeO_2 units. The glasses with low modifier content consist of a continuous random network constructed by sharing corners of TeO_4 trigonal bipyramids and TeO_{3+1}. The IR study by Dimitriev et al. [6] shows that in tellurite glasses, both the 3- and 4-coordinated tellurite polyhedra are simultaneously formed. The IR studies of the present glass discussed in chapter 3 shows the transformation of 4-coordinated polyhedra into 3-coordinated ones with the increase of

CuO modifier. The formation of Te-O-Cu and Cu-O-Cu bonds also takes place as CuO content increases. The Cu-O-Cu bonds are responsible for antiferromagnetically (AFM) and ferromagnetically (FM) coupled clusters in the glass matrix. Increase in CuO content increases the concentration of Cu-O-Cu bonds leading to formation of CuO rich regions in the glass matrix as reported by Criocas et al [7].

Table 5.1 Magnetic parameters for the glasses (100-x)TeO_2-xCuO (x = 10, 20, 30, 40 and 50 mol%)

Sample	x (mol%)	M/H (emu/mol/Oe) x 10^{-4} (±0.01)	C_M (emu/mol) X 10^{-2} (±0.01)	θ_p (K)	μ_{eff} μ_B (±0.01)	y (mol%)
T9C1	10	0.67	2	0	1.26	5
T8C2	20	2.15	7.13	-31	1.69	19
T7C3	30	2.44	9.03	-7	1.55	24
T6C4	40	3.17	12.89	-106	1.61	34
T5C5	50	3.52	11.89	-38	1.38	32

Figure 5.1.3 shows the M-H plots for the glass samples at 300K. The magnetization increases with the increase in CuO content. Figure 5.1.4 shows M versus H plots for various samples recorded in the low-field region. A small hysteresis loop in the low-field region is observed for all samples, indicating the existence of ferromagnetic cluster formation in the glass matrix. This also indicates increase in magnetic clusters with increase in CuO content.

Figure 5.1.5 shows the M-H plots for the glass samples at 80K. A small hysteresis loop in the low-field region observed for all the samples, indicating the existence of ferromagnetic cluster formation in the glass matrix and their persistence at low temperatures.

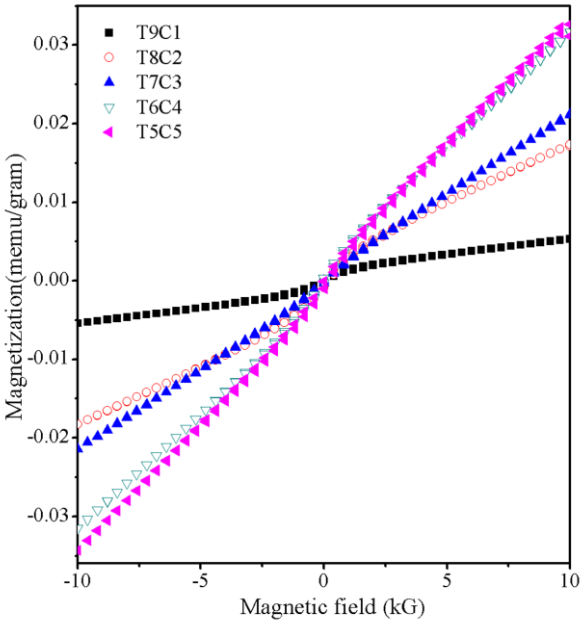

Fig 5.1.3. Magnetization vs. Field for x = 10, 20, 30, 40 and 50 mol% glass samples at 300K

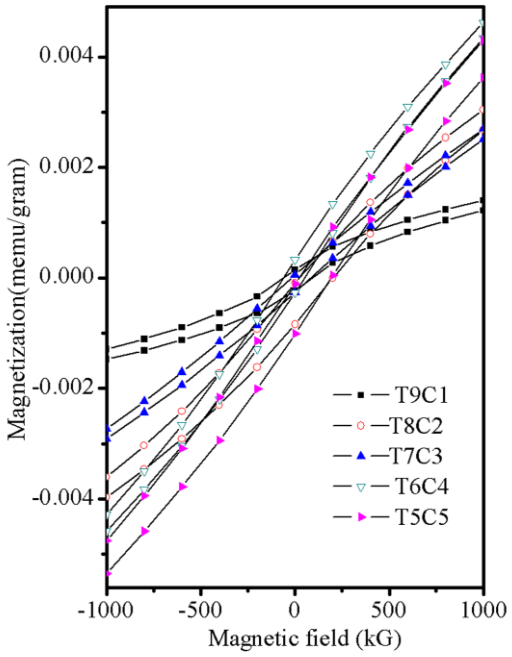

Fig 5.1.4. M versus H in low-field region for various glass samples at 300K

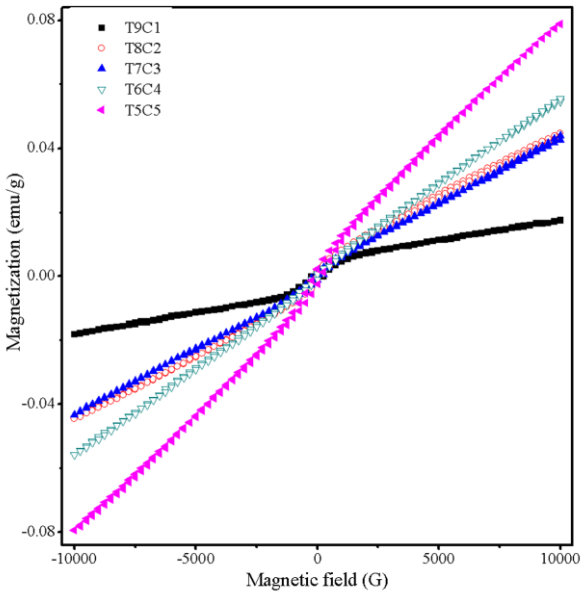

Fig 5.1.5. Magnetization vs. Field for x = 10, 20, 30, 40 and 50 mol% glass samples at 80K

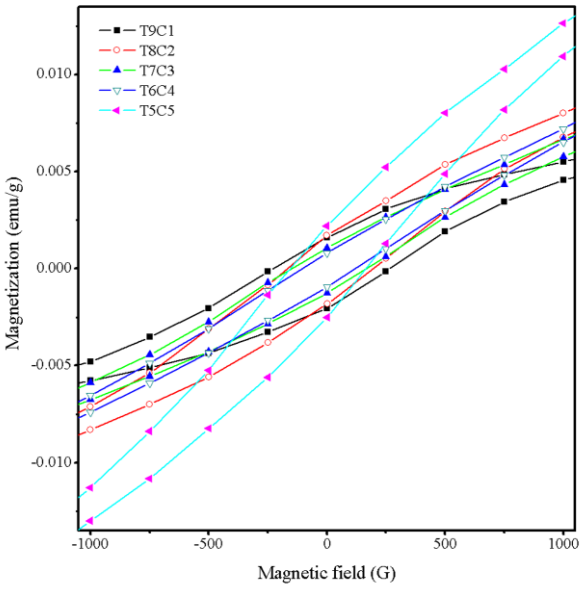

Fig 5.1.6. M versus H in low-field region for various glass samples at 80K

In conclusion, for Copper tellurite glasses, the temperature dependence of the reciprocal magnetic susceptibility of paramagnetic materials shows Curie-Weiss type behaviour. The paramagnetic susceptibility of the glasses increases as a function of x. The negative paramagnetic Curie temperature calculated for the glasses indicates superexchange magnetic interactions between the copper ions in the glass which are

predominantly anti-ferromagnetically coupled. The vitreous oxide structure imposes the short-range character of magnetic interaction and enhances the structural image of clusters. The μ_{eff} values obtained for all samples are lower than the magnetic moment of the free ion ($\mu_{Cu}^{2+} = 1.73\mu_B$) indicating the presence of both Cu^{2+} and Cu^{+} ions in these glasses. A small hysteresis loop in the low-field region of M-H plots observed for all samples indicates the existence of ferromagnetic cluster formation in the glass matrix.

5.2. $80TeO_2$-(20-x)ZnO-xFe_2O_3 glass system:

The M vs. T plots for various glass samples are shown in fig.5.2.1. Magnetic moment decreases with the increase in temperature and increases with the increase in Fe_2O_3 content in the glass composition. χ^{-1} vs T plots for various glass compositions are shown in fig.5.2.2. The straight lines are least square fits to the Curie-Weiss law. The paramagnetic susceptibility of the glasses increases as a function of x.

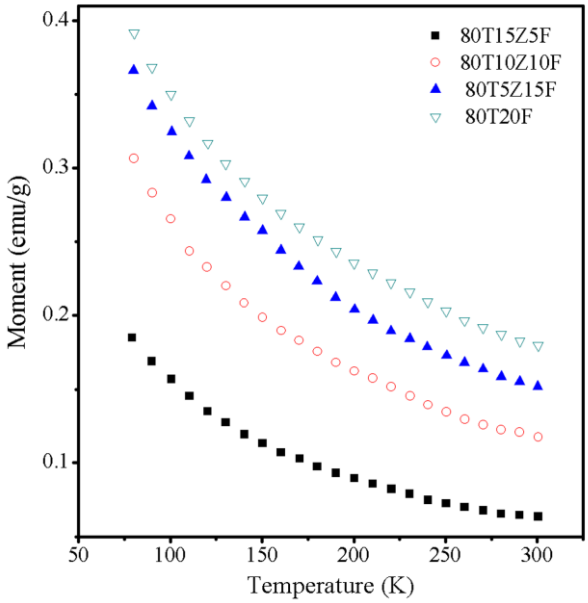

Fig 5.2.1. M vs. T for $80TeO_2$-(20-x)ZnO-xFe_2O_3, where x = 5, 10, 15 and 20 mol% glass samples

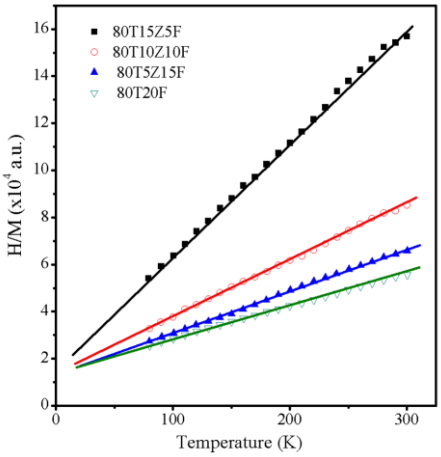

Fig 5.2.2. H/M vs. T for $80TeO_2$-(20-x)ZnO-xFe_2O_3 glass system

Temperature dependence of the reciprocal magnetic susceptibility of paramagnetic materials shows Curie-Weiss behaviour as per Eq. (5.1). The straight lines in fig.5.2.2 represent the least square fits to Eq. (5.1). The negative paramagnetic Curie temperature observed for the glasses indicates superexchange magnetic interactions between the iron ions in the glass which are predominantly anti-ferromagnetically coupled. The vitreous oxide structure imposes the short-range character of magnetic interaction and enhances the structural image of clusters. So, the magnetic behaviour of the glasses can be mictomagnetic type behaviour [8]. Analysis of the present data shows that the iron ions in the (20-x)ZnO-80TeO_2-xFe_2O_3 glass matrix behave magnetically similar to iron ions in TeO_2-B_2O_3-PbO[9], Bi_2O_3-PbO[10], B_2O_3-BaO-Fe_2O_3[11], Fe_2O_3-Sb_2O_3-TeO_2[12] and B_2O_3-SrO-Fe_2O_3[13] glasses.

The Curie temperature, curie constant and effective magnetic moments were calculated and tabulated in table 5.2. The effective magnetron number μ_{eff}, derived for each sample from the application of the simple Curie-Weiss model of paramagnetic behaviour may be compared to the published values for iron group salts [1]. The average experimental value for Fe^{2+} ions of 4.9 is closer to the measured values of the glass system. This indicates that, as expected from the chosen preparation conditions, the concentration of Fe^{2+} ions is much greater than that of Fe^{3+} ions in the glass samples. An ordering of the spins results in their cancellation due to the antiparallel arrangement [14]. Therefore, with increasing iron content, the speromagnetic spin interactions become more antiferromagnetic in nature (increasing θ_p in negative sign) and accordingly result in a lower level of magnetization and susceptibility of the material. The effective magnetic

moment values calculated using the relation $\mu_{eff} = 2.828(C_M/2x)^{1/2}$. The results are presented in table 5.2

Table5.2. Magnetic parameters for the glasses (20-x)ZnO-80TeO$_2$-xFe$_2$O$_3$ (x = 5,10,15 and 20 mol%)

Sample	X (mol%)	M/H (emu/mol/Oe) x 10^{-3} (±0.01)	C_M (emu K/mol) (±0.01)	θ_p (K)	μ_{eff} μ_B (±0.01)
15Z80T5F	5	0.94	0.31	-33	5.01
10Z80T10F	10	1.78	0.64	-58	5.05
5Z80T15F	15	2.37	0.88	-71	4.84
80T20F	20	2.87	1.18	-110	4.85

Figure 5.2.3 and 5.2.4 shows the M-H plots for the glass samples at 300K. The magnetization increases with the increase in Fe_2O_3 content. A small hysteresis loop in the low-field region observed for all samples indicates the existence of ferromagnetic cluster formation in the glass matrix. With increase in magnetic oxide content, formation of clusters is also increasing. This result is matching with the ESR result, where the increase of the intensity of g≈2.0 absorptions is observed at the expense of resonance centred at g ≈ 4.3 (from figure 4.2.1).

Figure 5.2.5 and 5.2.6 show the M-H plots for the glass samples recorded at 80K. The magnetization increases with the increase in paramagnetic oxide content. A small hysteresis loop in the low-field region observed for all samples indicates the existence of ferromagnetic cluster formation in the glass matrix and their persistence at low temperatures.

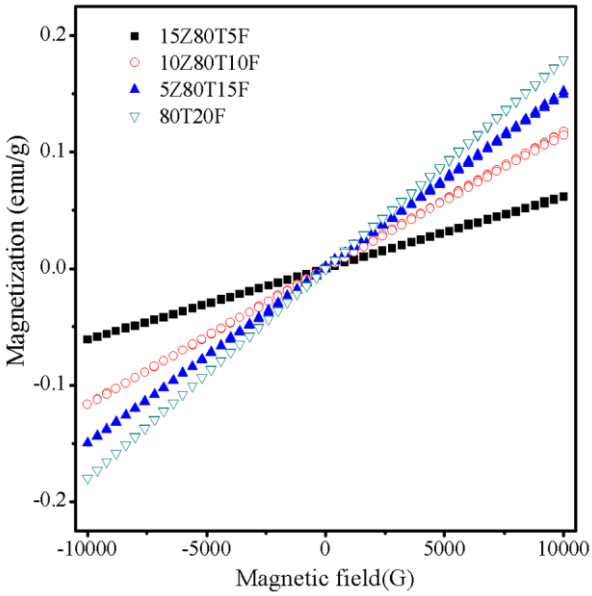

Fig 5.2.3. Magnetization vs. Field for x = 5, 10, 15 and 20 mol% glass samples at 300K

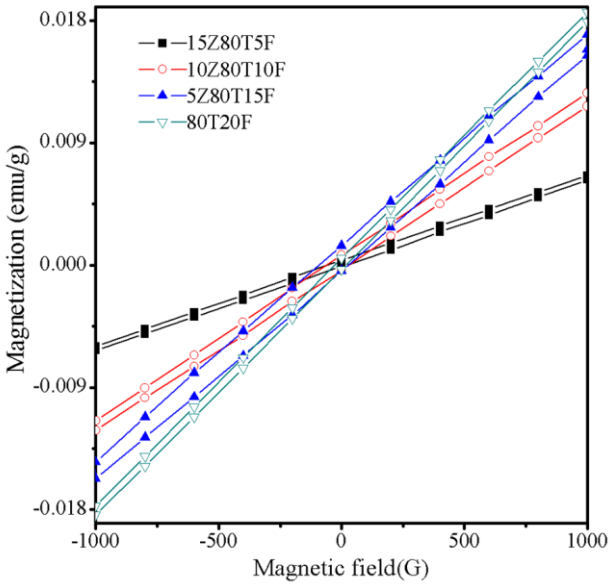

Fig 5.2.4. M versus H in low-field region for various glass samples at 300K

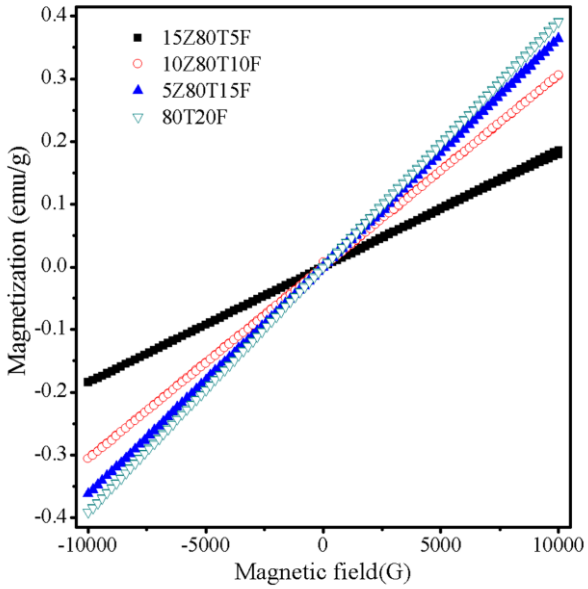

Fig 5.2.5. Magnetization vs. Field for x = 5, 10, 15 and 20 mol% glass samples at 80K

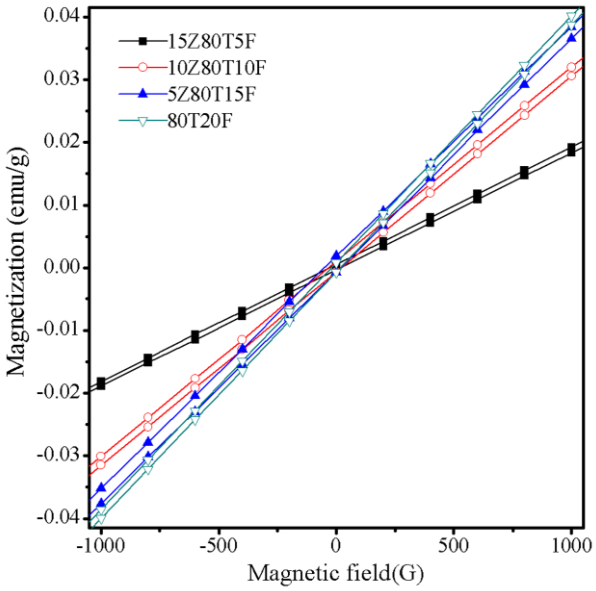

Fig 5.2.6. M versus H in low-field region for various glass samples at 80K

In conclusion, for the $80TeO_2$-(20-x)ZnO-xFe_2O_3 glass system, temperature dependence of the reciprocal magnetic susceptibility of paramagnetic materials shows a Curie-Weiss type behaviour. The negative paramagnetic Curie temperature observed for the glasses indicates superexchange magnetic interactions between the iron ions in the glass which are predominantly anti-ferromagnetically coupled. A small hysteresis loop in the low-field region of M-H plots observed for all samples indicates the existence of

ferromagnetic cluster formation in the glass matrix. This result is supported by ESR results.

5.3. $20ZnO-(80-x)TeO_2-xFe_2O_3$ glass system:

The M vs. T plots for various glass samples are shown in fig.5.3.1. Magnetic moment decreases with the increase in temperature and increases with the increase in Fe_2O_3 content in the glass composition. The χ^{-1} vs T plots for various glass compositions are shown in fig.5.3.2. The straight lines are least square fits to the Curie-Weiss law. The paramagnetic susceptibility of the glasses increases with increase in x.

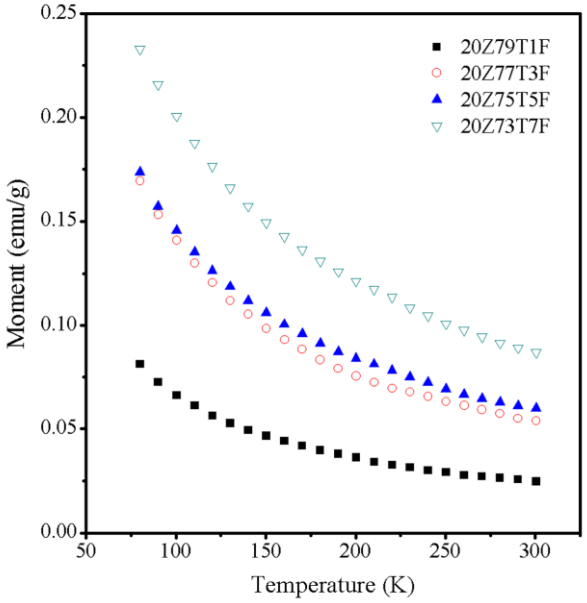

Fig 5.3.1. M vs. T for 20ZnO- (80-x)TeO_2-xFe_2O_3, where x = 5, 10, 15 and 20 mol% glass samples

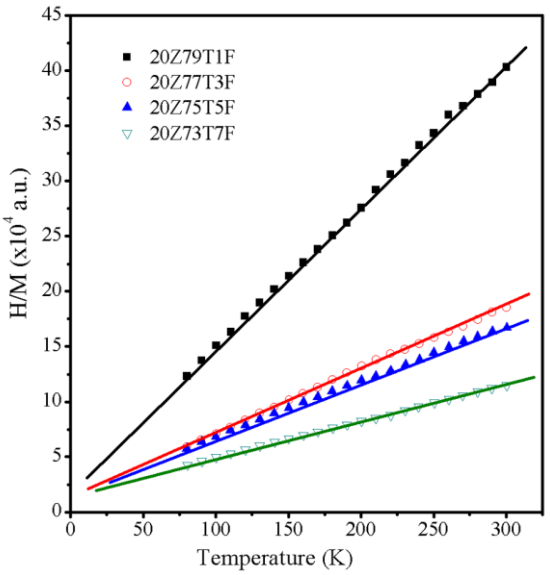

Fig 5.3.2. H/M vs. T for 20ZnO- (80-x)TeO_2-xFe_2O_3 glass system

Temperature dependence of the reciprocal magnetic susceptibility of paramagnetic materials shows Curie-Weiss behaviour as per Eq. (5.1). The straight lines in fig.5.3.2 represent the least square fit to Eq. (5.1). The negative paramagnetic Curie temperature observed for the glasses indicates superexchange magnetic interactions between the iron ions in the glass which are predominantly anti-ferromagnetically coupled. The magnetic behaviour of the glasses can be mictomagnetic type [8]. Analysis of the present data shows that the iron ions in the 20ZnO-(80-x)TeO_2-xFe_2O_3 glass matrix behave magnetically similar to iron ions in TeO_2-B_2O_3-PbO[9], Bi_2O_3-PbO[10], B_2O_3-BaO-Fe_2O_3[11], Fe_2O_3-Sb_2O_3-TeO_2[12] and B_2O_3-SrO-Fe_2O_3[13] glasses.

The Curie temperature, curie constant and effective magnetic moments were calculated and listed in table 5.3. The effective magnetron number μ_{eff}, derived for each sample from the application of the simple Curie-Weiss model of paramagnetic behaviour , may be compared to the published values for iron group salts [1]. The average experimental value for Fe^{3+} ions of 5.9 is closer to the measured values for 1 and 3 mol% Fe_2O_3 samples than the average value of 4.9 for Fe^{2+} ions. This indicates that, as expected from the chosen preparation conditions, the concentration of Fe^{3+} ions is much greater than that of Fe^{2+} ions in these two samples. An ordering of the spins results in their cancellation due to the antiparallel arrangement [14]. Therefore, with increasing iron content, the speromagnetic spin interactions become more antiferromagnetic in nature (increasing θ_p in negative sign) and accordingly result in a lower level of

magnetization and susceptibility of the material. The effective magnetic moment values were calculated using the relation $\mu_{eff} = 2.828(C_M/2x)^{½}$ and are listed in table.

Table5.3. Magnetic parameters for the glasses 20ZnO-(80-x)TeO_2-xFe_2O_3 (x = 1,3,5 and 7 mol%)

Sample	X (mol%)	M/H (emu/mol/Oe) x 10^{-4} (±0.01)	C_M (emu K/mol) (±0.01)	θ_p (K)	μ_{eff} μ_B (±0.01)
20Z79T1F	1	3.57	0.11	-18	6.74
20Z77T3F	3	7.77	0.25	-26	5.81
20Z75T5F	5	8.64	0.29	-38	4.83
20Z73T7F	7	12.5	0.44	-53	5.02

Figure 5.3.3 and 5.3.4 show the M-H plots for the glass samples at 300K. The magnetization increases with the increase in paramagnetic oxide content. A small hysteresis loop in the low-field region observed for all samples except for 20Z79T1F sample, indicates the existence of ferromagnetic cluster formation in the glass matrix. With increase in magnetic oxide content, formation of clusters also increases. This is supported by ESR data, where the increase in the intensityof g≈2.0 absorptions is observed at the expense of g≈4.3 resonance. Figure 5.3.5 and 5.3.6 shows the M-H plots for the glass samples at 80K. A small hysteresis loop in the low-field region is observed for all samples, indicating the existence of ferromagnetic cluster formation in the glass matrix.

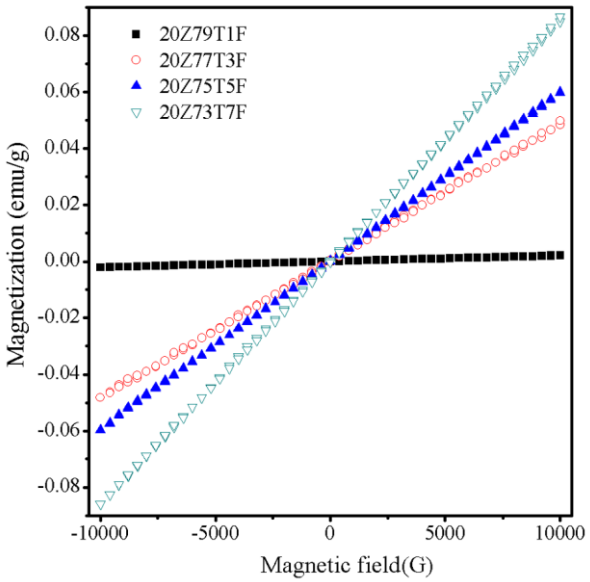

Fig 5.3.3. Magnetization vs. Field for x = 1, 3, 5 and 7 mol% glass samples at 300K

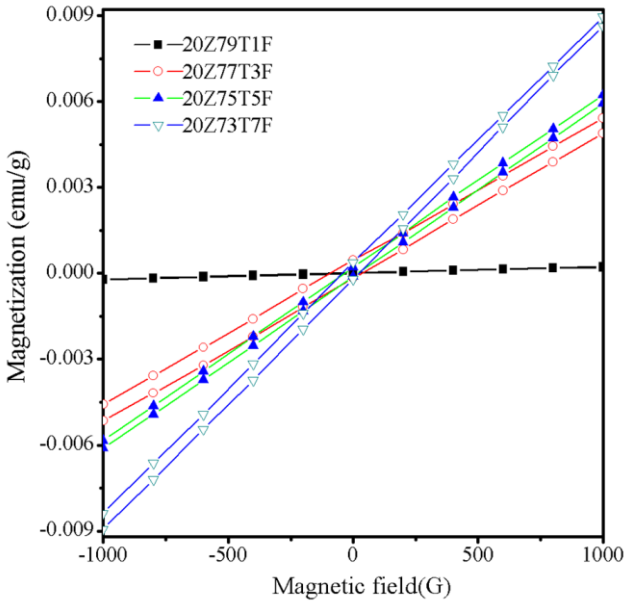

Fig 5.3.4. M versus H in low-field region for various glass samples at 300K

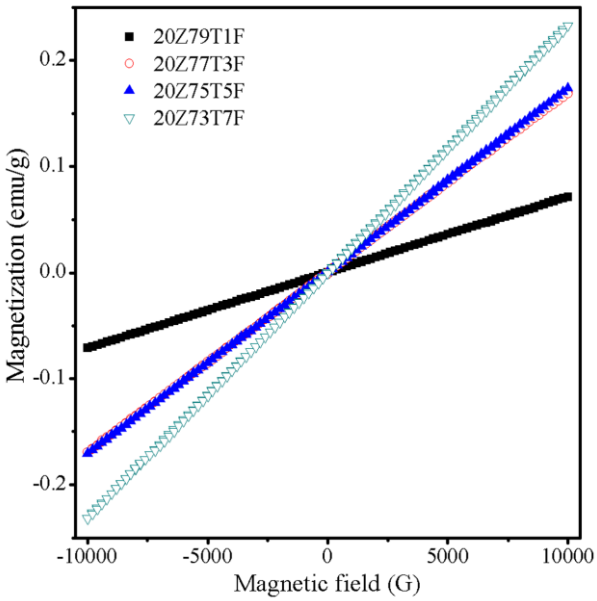

Fig 5.3.5. Magnetization vs. Field for x = 1, 3, 5 and 7 mol% glass samples at 80K

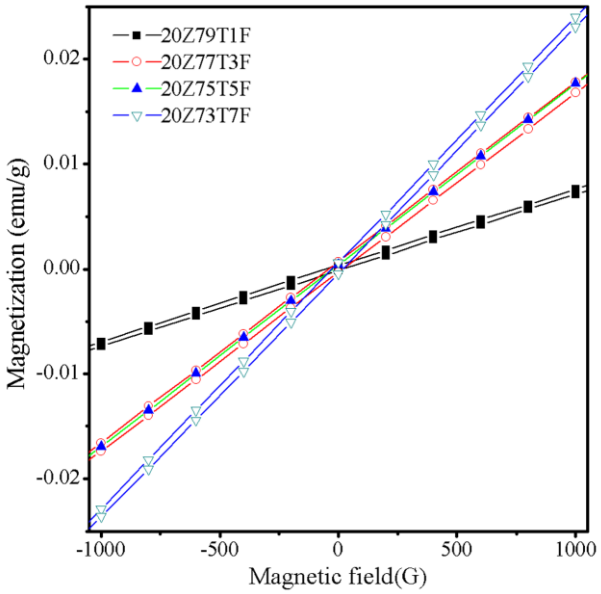

Fig 5.3.6. M versus H in low-field region for various glass samples at 80K

In brief, for 20ZnO-(80-x)TeO_2-xFe_2O_3 glass system, temperature dependence of the reciprocal magnetic susceptibility of paramagnetic materials shows Curie-Weiss behaviour. The negative paramagnetic Curie temperature calculated for the glasses indicates superexchange magnetic interactions between the iron ions in the glass which are predominantly anti-ferromagnetically coupled. A small hysteresis loop in the low-field region of M-H plots observed for all samples indicates the existence of

ferromagnetic cluster formation in the glass matrix. This result is matching with ESR result, where the presence of the g≈2.0 absorptions in all the samples, which is characteristic for cluster formation of Fe ions, is observed.

5.4. 10 Fe_2O_3-(90-x)TeO_2-x Bi_2O_3 glass system:

Magnetization versus temperature plots for various glass compositions are shown in fig. 5.4.1. The χ^{-1} versus T plots for various glass compositions are shown in fig.5.4.2. This plot is not linear throughout the temperature range. Figure 5.4.2 shows that two straight lines fit as per Curie-Weiss law with change of slope at ~ 200K for these glass samples are obtained. The M value and susceptibility decreases with the increase in Bi_2O_3 content.

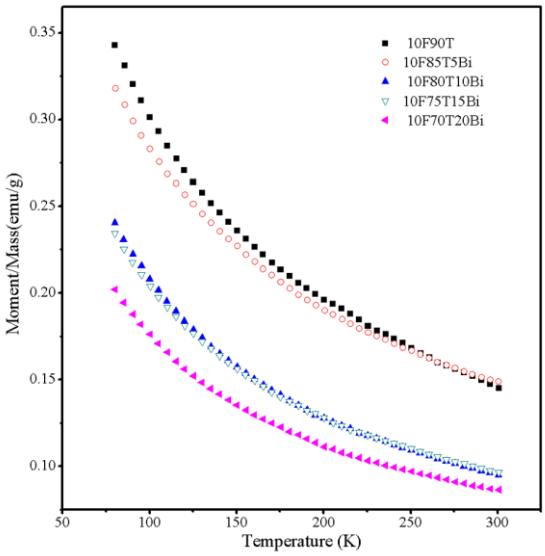

Fig 5.4.1. M vs. T for 10 Fe_2O_3-(90-x) TeO_2-x Bi_2O_3 glass system

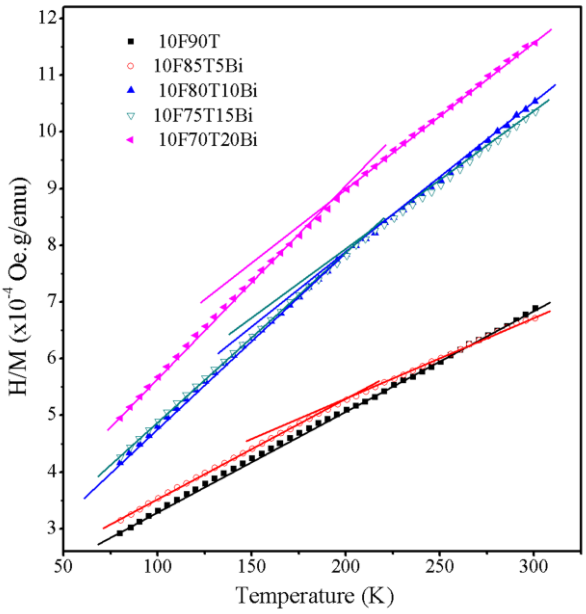

Fig 5.4.2. H/M vs. T for 10 Fe_2O_3-(90-x) TeO_2-x Bi_2O_3 glass system

Temperature dependence of the reciprocal magnetic susceptibility of paramagnetic materials shows a Curie-Weiss type behaviour at low temperature side as well as high temperature side, can be expressed as per Eq. (5.1). The straight lines in fig.5.4.2 represent the least square fit to Eq. (5.1). The negative paramagnetic Curie temperature calculated for the glasses indicates superexchange magnetic interactions between the iron ions in the glass which are predominantly anti-ferromagnetically coupled. Analysis of the present data shows that the iron ions in the 10 Fe_2O_3-(90-x) TeO_2-xBi_2O_3 glass matrix are coupled antiferromagnetically and the interaction increases with increase in Bi_2O_3 content.

The Curie temperature, curie constant and effective magnetic moments were calculated and tabulated in table 5.4. The effective magnetron number μ_{eff}, derived for each sample is compareable to the published values for other glasses containing iron. The average value for Fe^{3+} ions of 5.9 is close to the measured values for all glass samples than the average value of 4.9 for Fe^{2+} ions. This indicates that the concentration of Fe^{3+} ions is much greater than that of Fe^{2+} ions in these samples. With increase in bismuth content, the speromagnetic spin interactions become more antiferromagnetic in nature (increasing θ_p in negative sign) and accordingly result in a lower level of magnetization and susceptibility of the material. The calculated the effective magnetic moment values using the relation $\mu_{eff} = 2.828(C_M/2x)^{1/2}$ are listed in table 5.4.

Table5.4. Magnetic parameters for the glasses $10Fe_2O_3$-(90-x)TeO_2-xBi_2O_3, where (x=0,5,10,15 and 20 mol%)

Sample	x (mol%)	M/H (emu/mol/Oe) x 10^{-3} (±0.01)	C_M (emu K/mol) (±0.01)	θ_p (K)	μ_{eff} μ_B (±0.01)	C_M (emu K/mol) (±0.01)	θ_p (K)	μ_{eff} μ_B (±0.01)
			80K < T <180K			200 < T < 300K		
10F90T	0	2.32	0.9	-89	6.01	0.90	-89	6.01
10F85T5B	5	2.61	1.04	-101	6.46	1.18	-154	6.88
10F80T10B	10	1.81	0.64	-57	5.08	0.71	-91	5.31
10F75T15B	15	1.99	0.73	-66	5.39	0.82	-115	5.74
10F70T20B	20	1.91	0.71	-72	5.33	0.85	-144	5.82

Figure 5.4.4 - 5.4.7 shows the M-H plots for the glass samples at 300K and 80 K. A small hysteresis loop in the low-field region observed for all samples indicates the existence of ferromagnetic cluster formation in the glass matrix. This result is matching with ESR result, where the presence of the g≈2.0 absorptions in all the samples characteristic Fe ions clusters is observed.

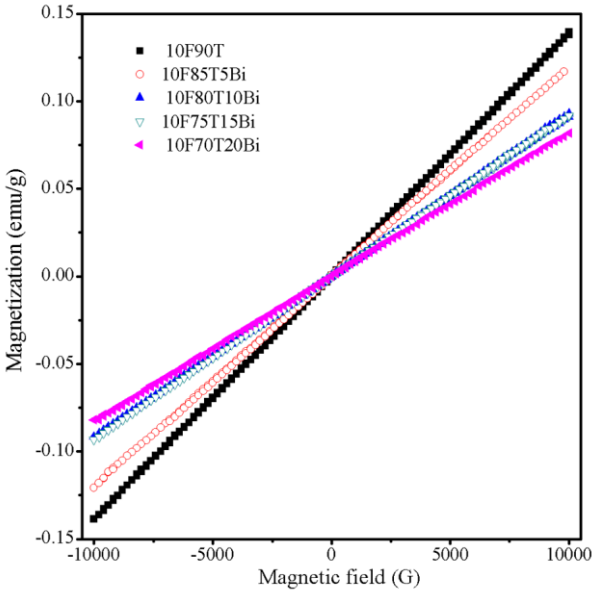

Fig 5.4.3. Magnetization vs. Field for x = 0, 5, 10, 15 and 20 mol% glass samples at 300K

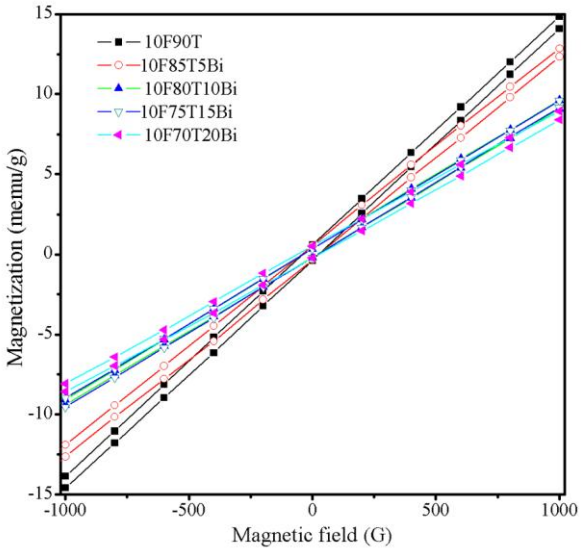

Fig 5.4.4. M versus H in low-field region for various glass samples

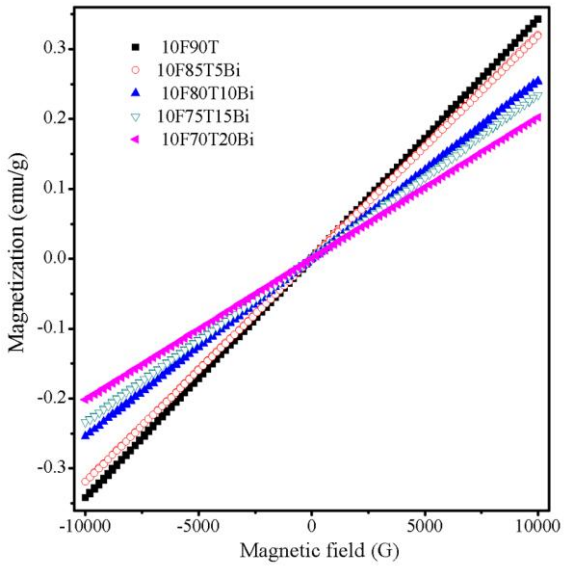

Fig 5.4.5. Magnetization vs. Field for x = 0, 5, 10, 15 and 20 mol% glass samples at 80K

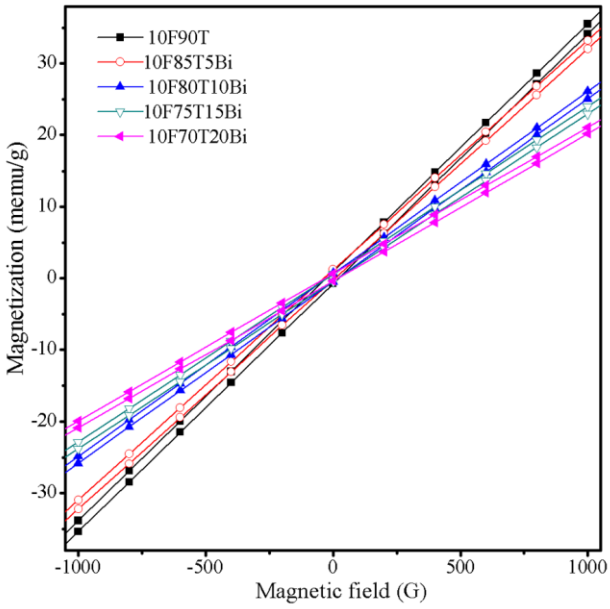

Fig 5.4.6. M versus H in low-field region for various glass samples at 80K

5.5. 20 Fe_2O_3-(80-x) TeO_2-x Bi_2O_3 glass system:

Magnetization and (χ^{-1}) versus temperature plots for various glass compositions are shown in fig. 5.5.1 and 5.5.2 respectively. χ^{-1} vs. T data can not be fitted to one single straight line throughout the temperature range. Figure 5.5.2 shows the straight lines fit as per Curie-Weiss law with a change in slope at ~ 200K. The paramagnetic susceptibility of the glasses decreases as a function of x.

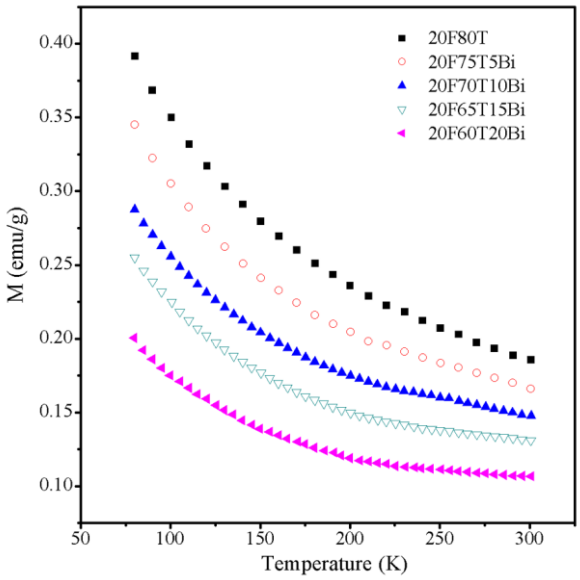

Fig 5.5.1. M vs. T for 20 Fe_2O_3-(80-x) TeO_2-x Bi_2O_3 glass system

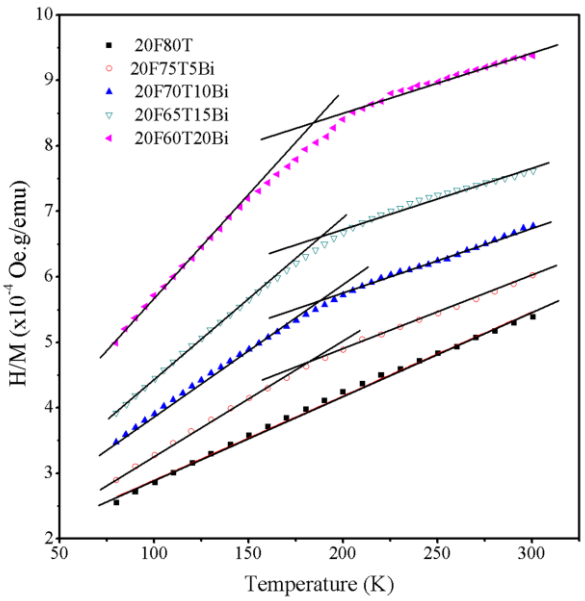

Fig 5.5.2. H/M vs. T for 20 Fe_2O_3-(80-x) TeO_2-x Bi_2O_3 glass system

The Curie temperature, curie constant and effective magnetic moments were calculated and are listed in table 5.5.

Figure 5.5.3 shows the M-H plots for the glass samples at 300K. The magnetization decreases with the increase in bismuth oxide content. Figure 5.5.4 shows the M versus H plots for various samples recorded in the low-field region. A small hysteresis loop in the low-field region is observed for all samples, indicating the existence

of ferromagnetic cluster formation in the glass matrix. This result is matching with ESR result, where the presence of the g≈2.0 absorptions in all the samples characteristic for cluster formation of Fe ions is observed. Figure 5.5.5 shows the MH plots for the glass samples at 80K. Figure 5.5.6 shows the M versus H plots for various samples recorded in the low-field region. A small hysteresis loop in the low-field region is observed for all samples, indicating the existence of ferromagnetic cluster formation in the glass matrix.

Table5.4. Magnetic parameters for the glasses 20 Fe_2O_3-(80-x) TeO_2-xBi_2O_3 (x = 0, 5, 10, 15 and 20 mol%)

Sample	x (mol%)	M/H (emu/mol/Oe) x 10^{-3} (±0.01)	C_M (emu K/mol) (±0.01)	θ_p (K)	μ_{eff} μ_B (±0.01)	C_M (emu K/mol) (±0.01)	θ_p (K)	μ_{eff} μ_B (±0.01)
			80< T <180K			200< T <300K		
20F80T	0	2.96	1.26	-126	5.02	1.26	-126	5.02
20F75T5B	5	2.91	1.14	-91	4.77	1.58	-243	5.61
20F70T10B	10	2.81	1.13	-102	4.75	1.87	-365	6.11
20F65T15B	15	2.7	1.04	-86	4.56	2.31	-555	6.79
20F60T20B	20	2.35	0.93	-96	4.31	2.37	-709	6.89

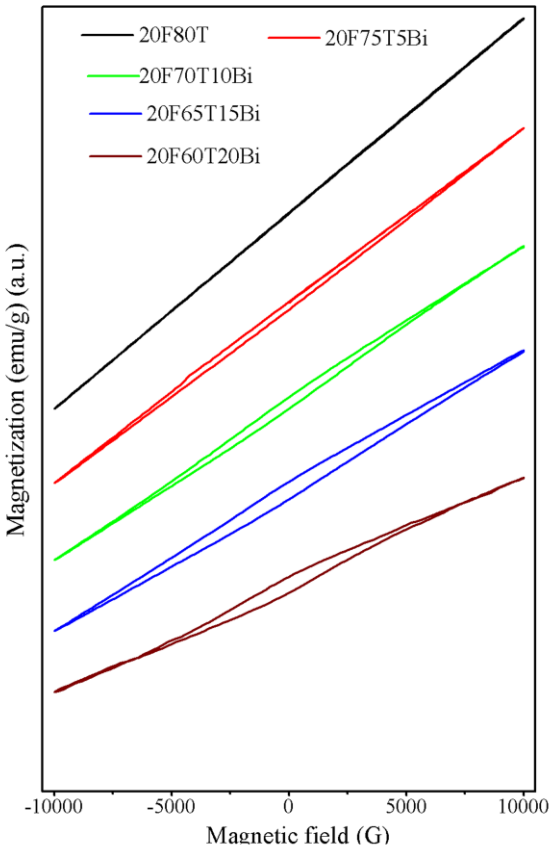

Fig 5.5.3. Magnetization vs. Field for x = 0, 5, 10, 15 and 20 mol% glass samples at 300K

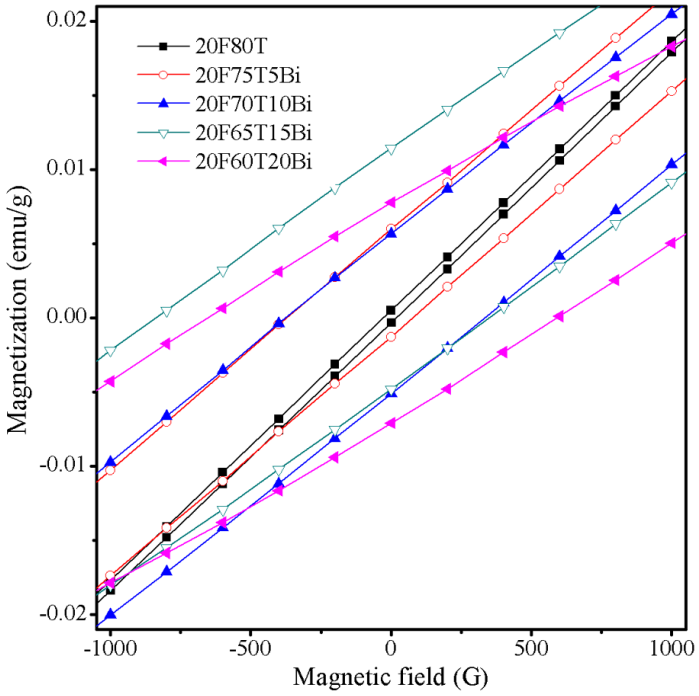

Fig 5.5.4. M versus H in low-field region for various glass samples at 300K

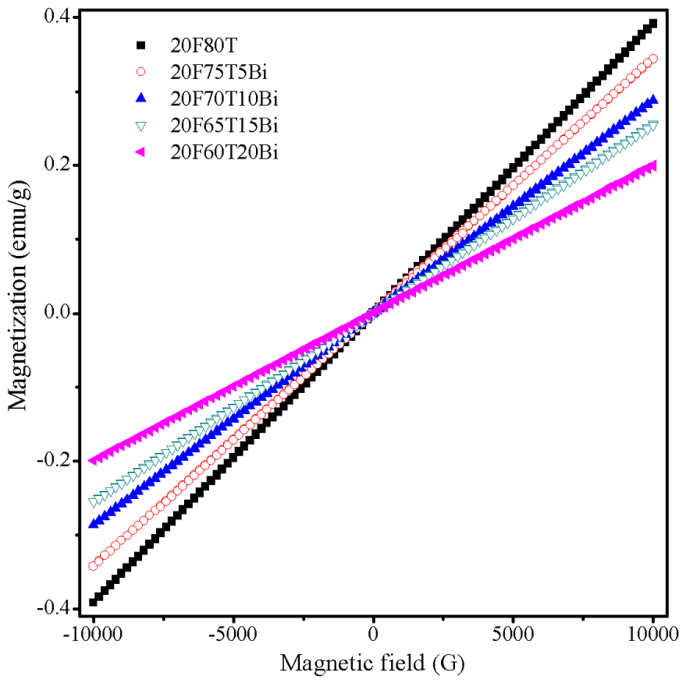

Fig 5.5.5. Magnetization vs. Field for x = 0, 5, 10, 15 and 20 mol% glass samples at 80K

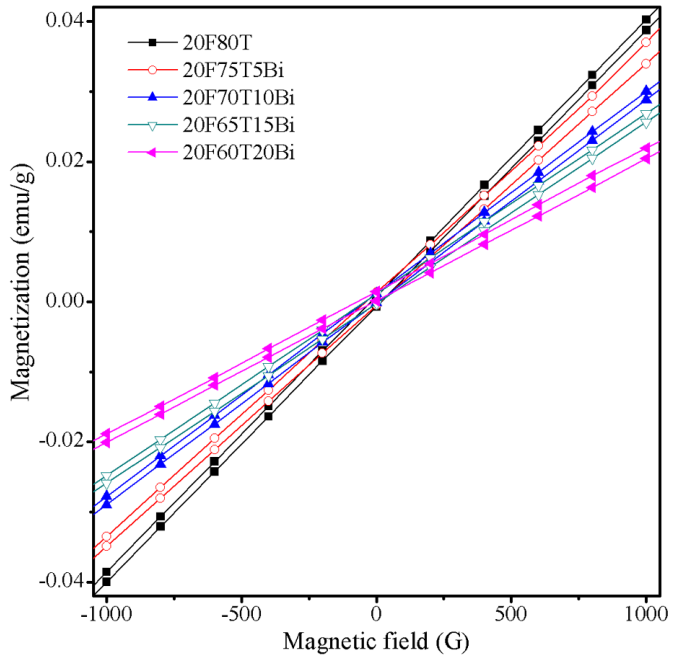

Fig 5.5.6. M versus H in low-field region for various glass samples at 80K

In conclusion, for both iron tellurite doped with Bi_2O_3 glass systems, namely 10 Fe_2O_3-(90-x)TeO_2-x Bi_2O_3, 20 Fe_2O_3-(80-x)TeO_2-x Bi_2O_3 , the (χ^{-1}) vs. T data is not linear throughout the temperature range. Two st. line fits are observed as per Curie-Weiss

law with a change in slope at ~ 200K. The magnetization and susceptibility decreases with the increase in Bi_2O_3 content.

The negative paramagnetic Curie temperature calculated for the glasses indicates antiferromagnetic (superexchange) magnetic interactions between the iron ions. With increase in Bi_2O_3 content , the magnetic spin interactions become more antiferromagnetic in nature (increasing negative θ_p value) resulting in lower magnetization and susceptibility of the material. A decrease in antiferromagnetic interaction below ~ 200K in both the series of glasses could be due the alignment of ferromagnetic clusters at low temperature.

5.6. (100-x)(70 Bi_2O_3 20 ZnO 10 PbO) - xFe_2O_3 glass system:

The magnetization studies were done for the glass system (100-x)(70 Bi_2O_3 20 ZnO 10 PbO) - xFe_2O_3 , where x= 5,10,15,20 and 25, using PPMS-VSM in the temperature range 5-300K in a field of 100 Oe. The data were collected after cooling the sample to 5K both in zero field and in a magnetic field to observe the magnetization behaviour. The M-H plots were also investigated in a field range of 2T to -2T, at a number of constant temperatures.

5.6. A.1. Magnetization as a function of temperature:

The zero-field-cooled (ZFC) and field-cooled (FC) magnetizations at low magnetic field for these glass samples exhibit the typical temperature-dependent magnetic behaviour associated with superparamagnetic relaxation phenomenon as the ZFC and FC magnetization bifurcate and the ZFC magnetization exhibits a peak or maximum at a lower temperature T_p than the bifurcation temperature T_{BF} as shown in figure 5.6.A.1. The FC magnetization is assumed to be a measure of the equilibrium magnetization over the entire temperature range while the ZFC magnetization is considered to be a non-equillibrium measurement below the bifurcation temperature where the magnetic moments of the nanoparticles with spin reorientation times greater than the measurement time (typically ~ 10^3 s for dc magnetization measurements) are frozen in random directions.

Figure 5.6.A.1 shows the Magnetization vs. temperature for glass samples at a static field 100 Oe. The samples show spin-glass behavior and the spin freezing

temperatures vary with the mol% of Fe_2O_3. The samples were initially cooled in zero external field (ZFC) and magnetization per unit gram values were measured at H = 100 Oe as the samples were warmed up to room temperature. Following this, M was measured as the sample was field-cooled (FC) in field back to 5K. Below T_{BF}, ZFC and FC curves are separated, signifying a possible superparamagnetic behavior. Both ZFC and FC data clearly indicate a broad peak in χ in the surroundings of T_p for the samples. The broad peak due to spin freezing may be attributed to the presence of clusters of varying sizes.

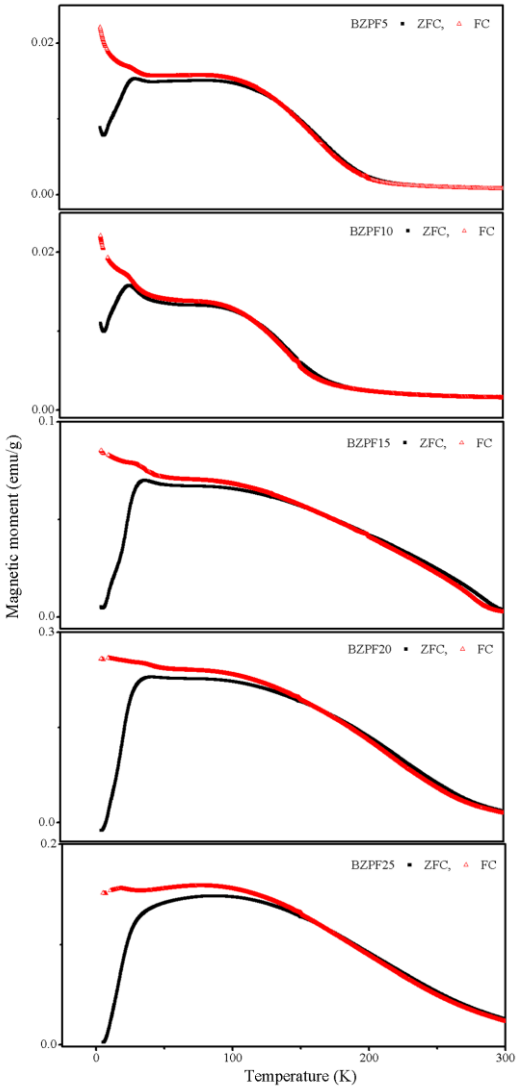

Fig 5.6.A.1 Magnetization vs. Temperature for x = 5 and 10 mol% glass samples

For x=5 and 10 mol%:

Fig 5.6.A.2 shows the temperature dependence of the reciprocal magnetic susceptibility for both the samples. The temperature dependence of the ZFC magnetization does not follow the expected Curie behaviour at higher temperatures. Instead, for glass samples 5 and 10% Fe_2O_3, the slope of H/M vs. T data has strong temperature dependence. The temperature axis intercept from the extrapolation of H/M vs. T slope is 124K and 104K [$\theta_c(T) > 0$] at high temperatures is suggestive of a ferromagnetic-like interacting system for glass samples containing 5 and 10 mol% Fe_2O_3.

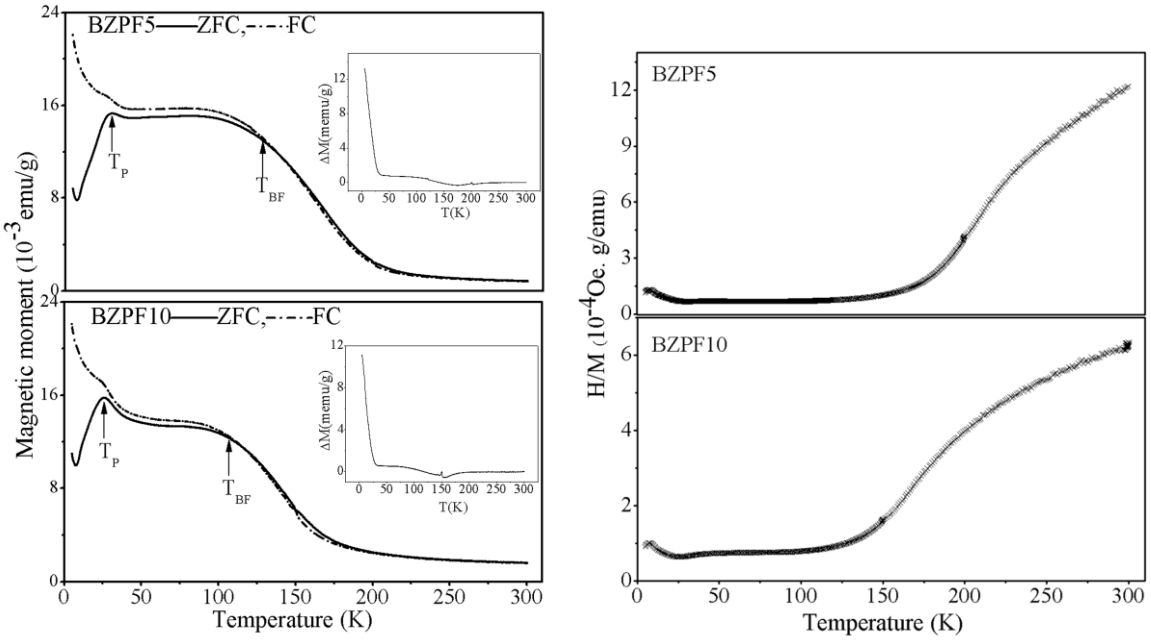

Fig 5.6.A.2 M Vs.T with ΔM and H/M vs. T for x = 5 and 10 mol% glass samples

An interesting feature of the susceptibilities at higher temperature, for the samples, is the crossover in their values, beginning at T~35K. As the temperature is increases from this point, the susceptibility for 5 mol% sample crosses the 10 mol% sample in turn to become higher in value. However the data taken to higher temperatures, the lines would continue crossing each other as the temperature rises further and the magnitudes of χ would then be in order of decreasing iron content. χ is a quantity dependent on the magnetization of a material, i.e. its ability to become magnetized, it is logical that at temperatures where the thermal agitation is too great to allow the speromagnetic ordering, the material with the largest concentration of a magnetic species

would have the greatest susceptibility. The higher concentration of magnetic species means there are a greater number of the iron clusters and that they are greater in size. Either way, the distance between them is reduced or at low temperatures the spin correlations are more easily transmitted, so enabling the system to exist in a higher degree of order. An ordering of the spins results in their cancellation due to the antiparallel arrangement [14].

For 5 and 10 mol% a positive paramagnetic curie temperature (θ_p) indicates a ferromagnetic coupling between the particles. Due to the disordered structure of glasses, magnetic ordering takes place only at short range, and in this case, the present glasses are exhibiting superparamagnetism.

For x=15, 20 and 25 mol%:

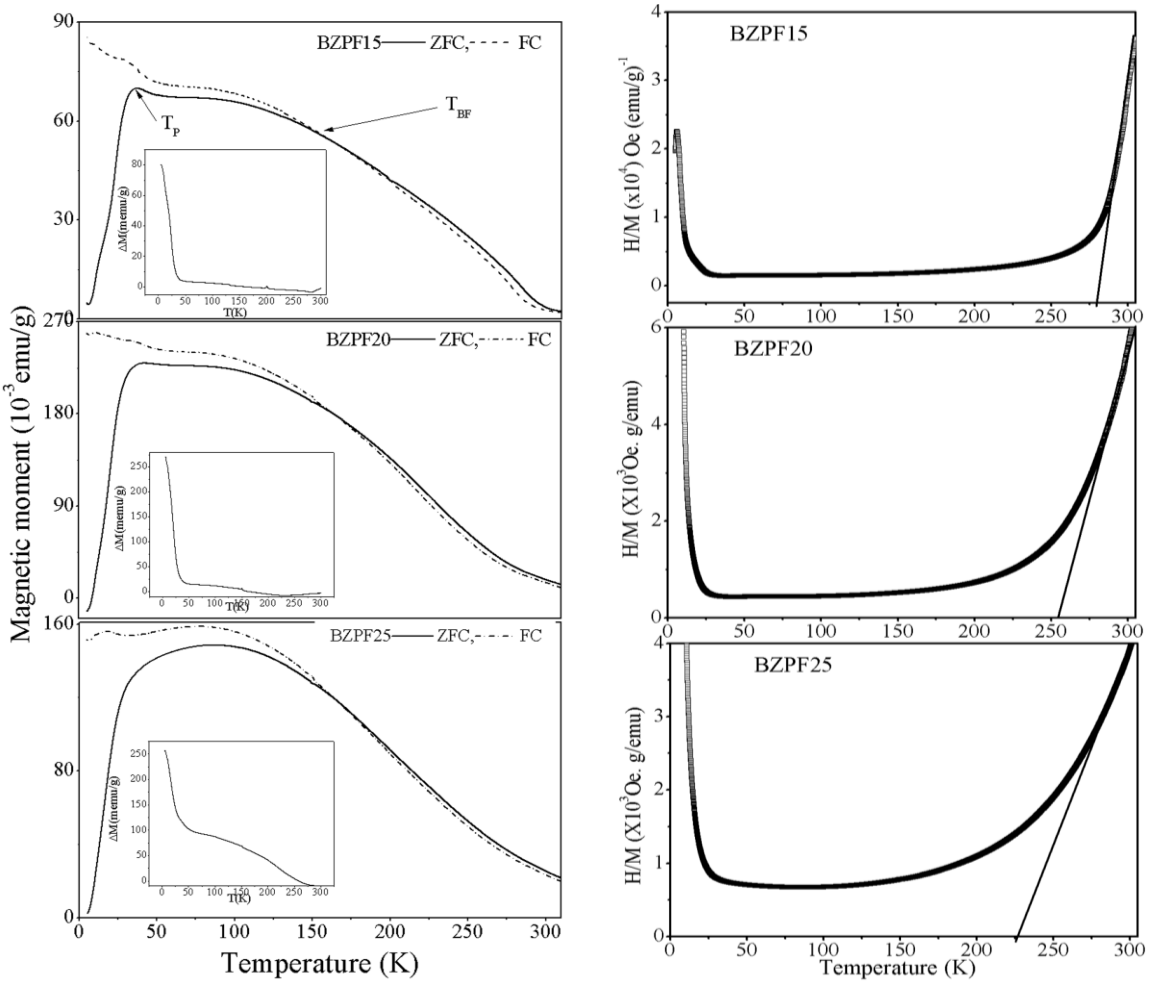

Fig 5.6.A.3 M Vs.T with ΔM and H/M vs. T for x = 15, 20 and 25 mol% glass samples

Figure 5.6.A.3 shows the temperature dependence of the magnetization and reciprocal magnetic susceptibility for the BZPF15, BZPF20 and BZPF25 samples follow Curie-Weiss behaviour in the high temperature region. From the temperature dependence of the ZFC magnetization for these samples, the slope of H/M vs. T data has a temperature axis intercept from the extrapolation of H/M vs. T slope at high temperature side are 275K, 247K and 212K [$\theta_c(T) > 0$] for BZPF15, BZPF20 and BZPF25 respectively is suggestive of a ferromagnetic-like" interacting system. χ is a quantity dependent on the magnetization of a material, i.e. its ability to become magnetized, it is logical that at temperatures where the thermal agitation is too great to allow the speromagnetic ordering, the material with the largest concentration of a magnetic species would have the greatest susceptibility. The higher concentration of magnetic species implies a greater number of the iron clusters and that they are large in size. Either way, the distance between them is reduced or at low temperatures the spin correlations are more easily transmitted, so enabling the system to exist in a higher degree of order.

For these samples, a positive paramagnetic curie temperature (θ_p) indicates a ferromagnetic coupling between the particles. Due to the disordered structure of glasses, magnetic ordering takes place only at short range, and in this case, the present glasses are exhibiting superparamagnetism. The χ values at different temperatures, spin freezing temperature, bifurcation temperature and the curie constant are presented in table 5.6.2. For all these samples, ΔM variation with T (where ΔM=FC-ZFC), is as shown in figures 5.6.A.2 and 5.6.A.3 respectively. ΔM is maximum in low temperature region and decreases with increasing temperature. In the high temperature region, both ZFC and FC are overlapping for these samples, representing minimum values to ΔM, and almost zero at room temperature.

5.6. B. Magnetization as a function of magnetic field:

The magnetization as a function of magnetic field were measured between 5 and 300K for the samples in order to assess how well the curves can be described in terms of a classical superparamagnetic behavior. The evidence of the presence of superparamagnetic clusters in the samples was obtained from the data on field dependence of the magnetization at a number of constant temperatures. For a superparamagnet one expects the presence of hysteresis and remanence in M versus H

data for $T<T_p$, and the absence of such effects above the spin freezing temperature. Data on the field dependence of M are shown in Fig 5.6.B.1 for two different temperatures, 5 and 300K, which are well below and above the spin freezing temperature respectively. The data show a definite remanence at 5K even though the hysteresis is weak. Such effects are not present at 300K, as expected for $T>T_p$ in samples containing superparamagnetic clusters.

At temperatures above T_p, the M vs. H curves show a non-hysteretic behavior with a linear field dependence as shown in fig.5.6.B.2, 5.6.B.3, 5.6.B.4, 5.6.B.5 and 5.6.B.6 for the glass samples BZPF5,BZPF10, BZPF15, BZPF20 and BZPF25 glass samples respectively. However, the M vs. H curves does not readily appear to approach a saturated magnetization by 20kOe, but instead continuously increase as a function of H at the highest fields. This high-field behavior is consistent with the presence of some paramagnetic regions [17]. In contrast, the M-H curves for temperatures below T_p exhibit a hysteretic behavior at the lowest fields and show a linear behavior at the highest field strengths. This type of temperature dependent behavior in the M vs. H curves is observed in many other superparamagnetic systems [17].

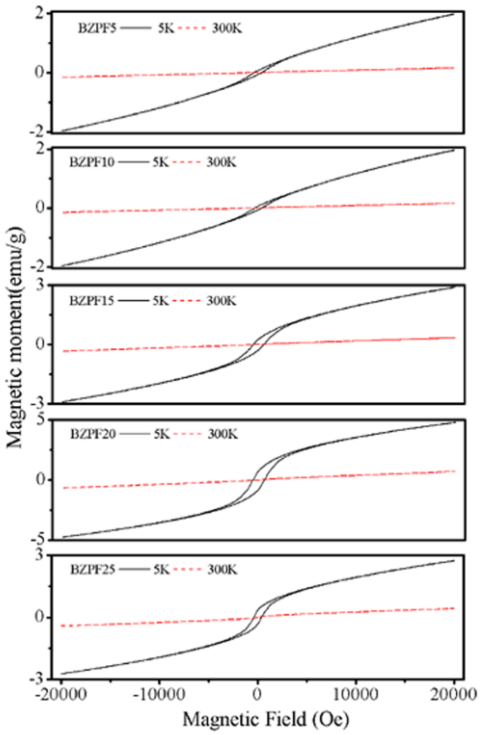

Fig 5.6.B.1. M vs. H plots for x = 5, 10, 15, 20 and 25 mol% glass samples at 5K and 300K

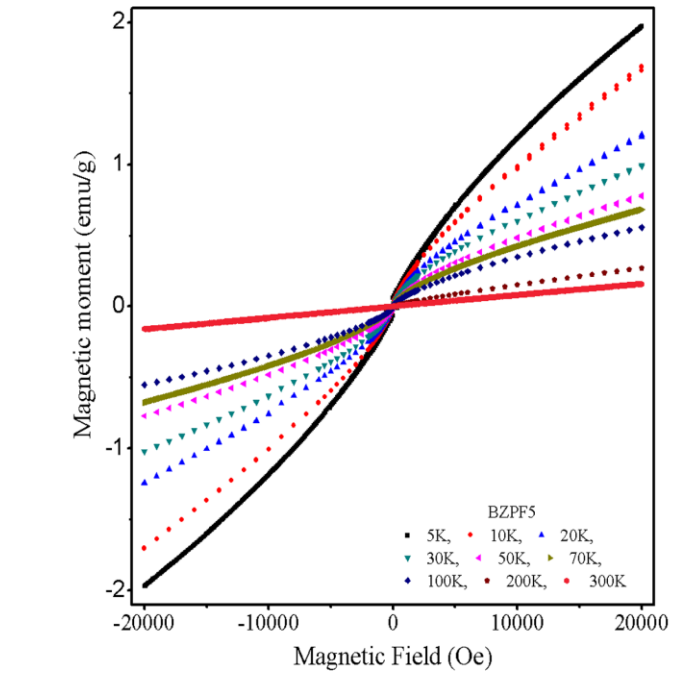

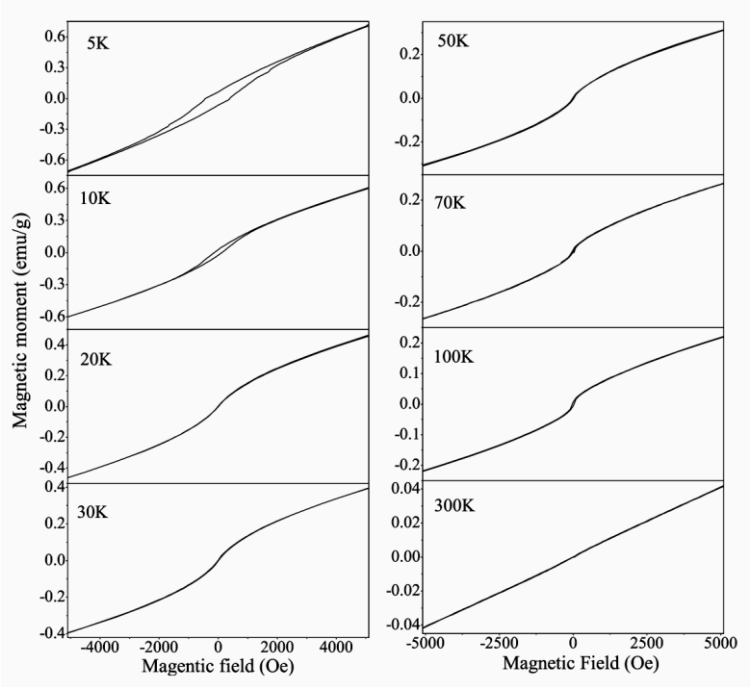

Fig 5.6.B.2 M vs. H for BZPF5 (x = 5 mol% Fe_2O_3) glass sample at different temperatures

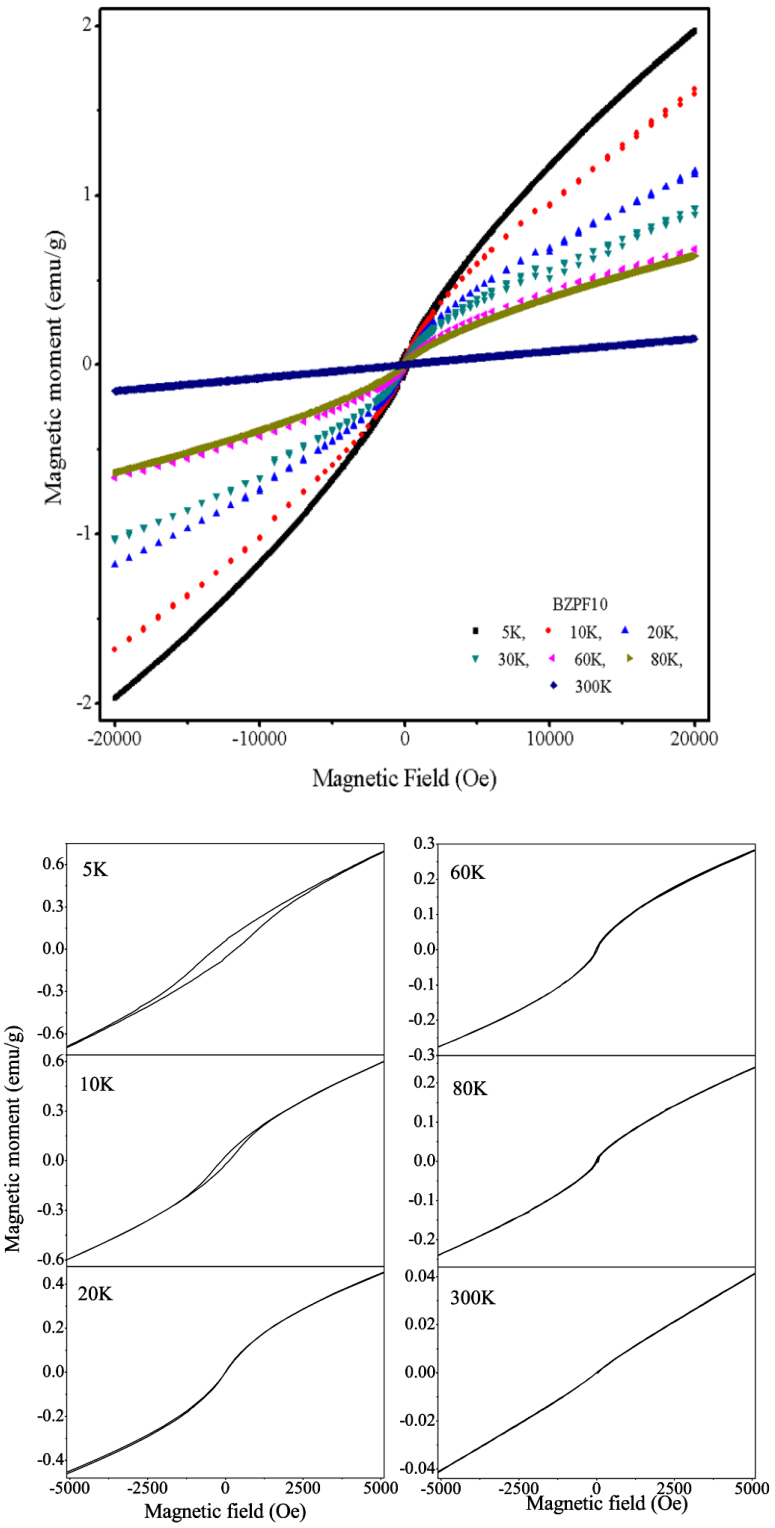

Fig 5.6.B.3 M vs. H for BZPF10 (x = 10 mol% Fe_2O_3) glass sample at different temperatures

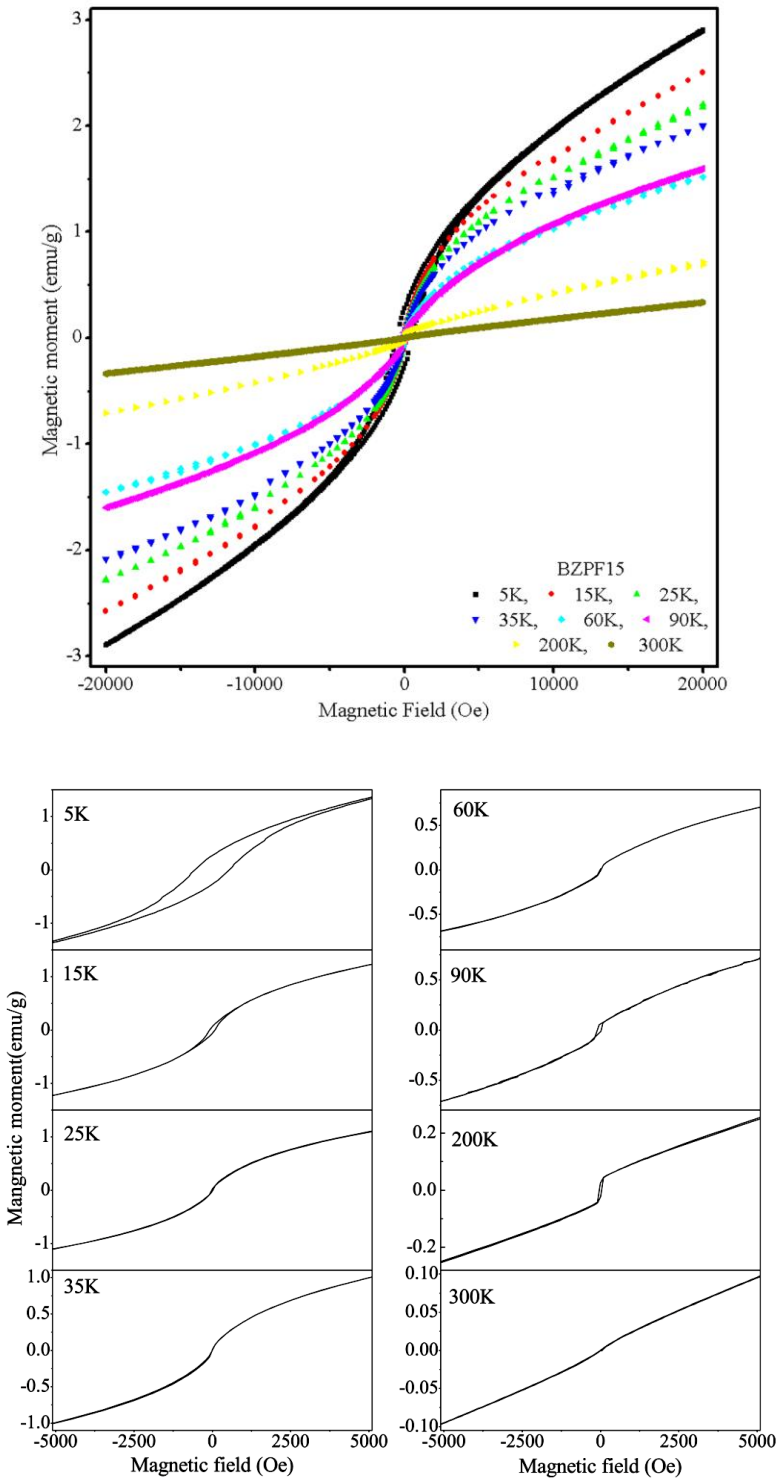

Fig 5.6.B.4 M vs. H for BZPF15 (x = 15 mol% Fe_2O_3) glass sample at different temperatures

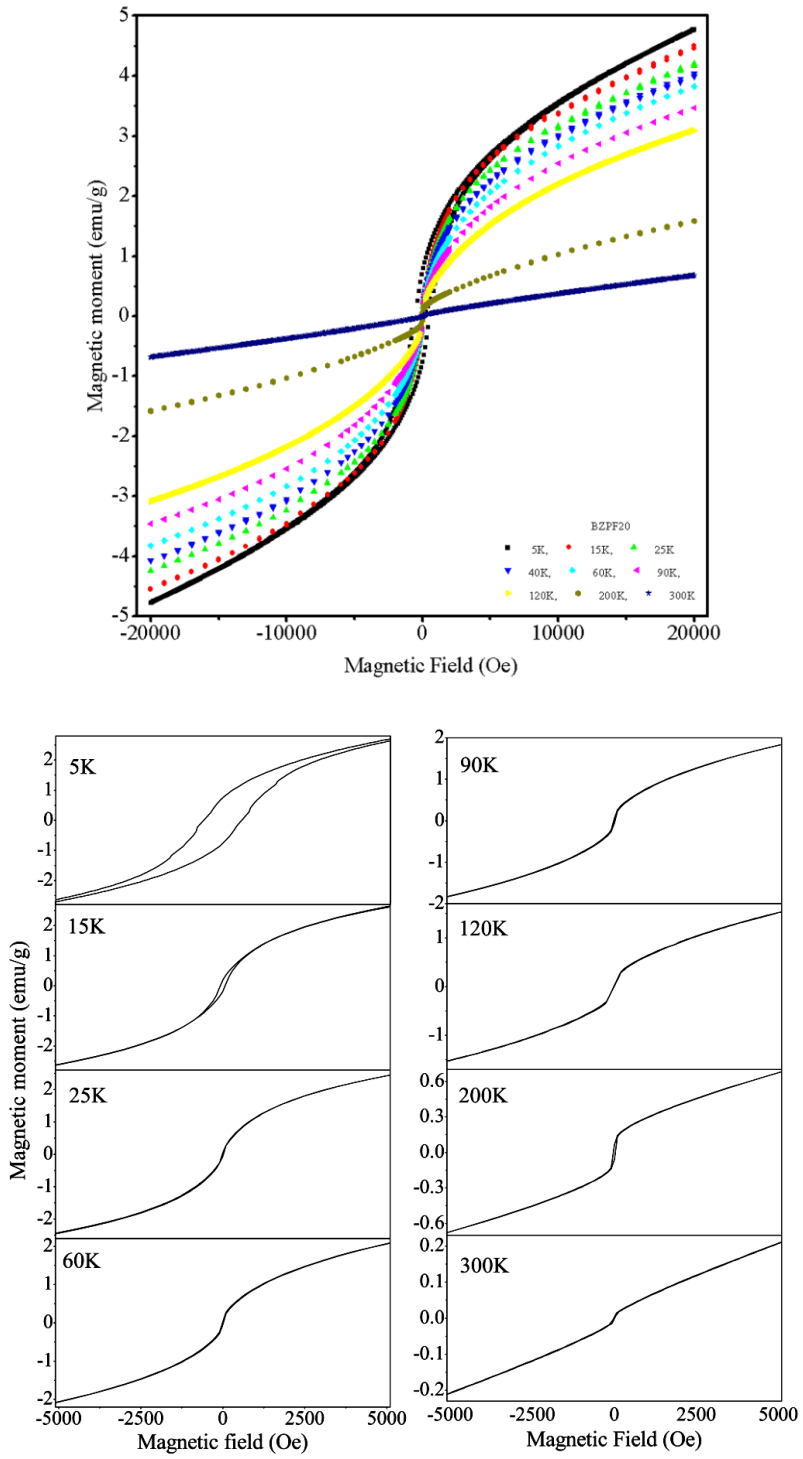

Fig 5.6.B.5 M vs. H for BZPF20 (x = 20 mol% Fe_2O_3) glass sample at different temperatures

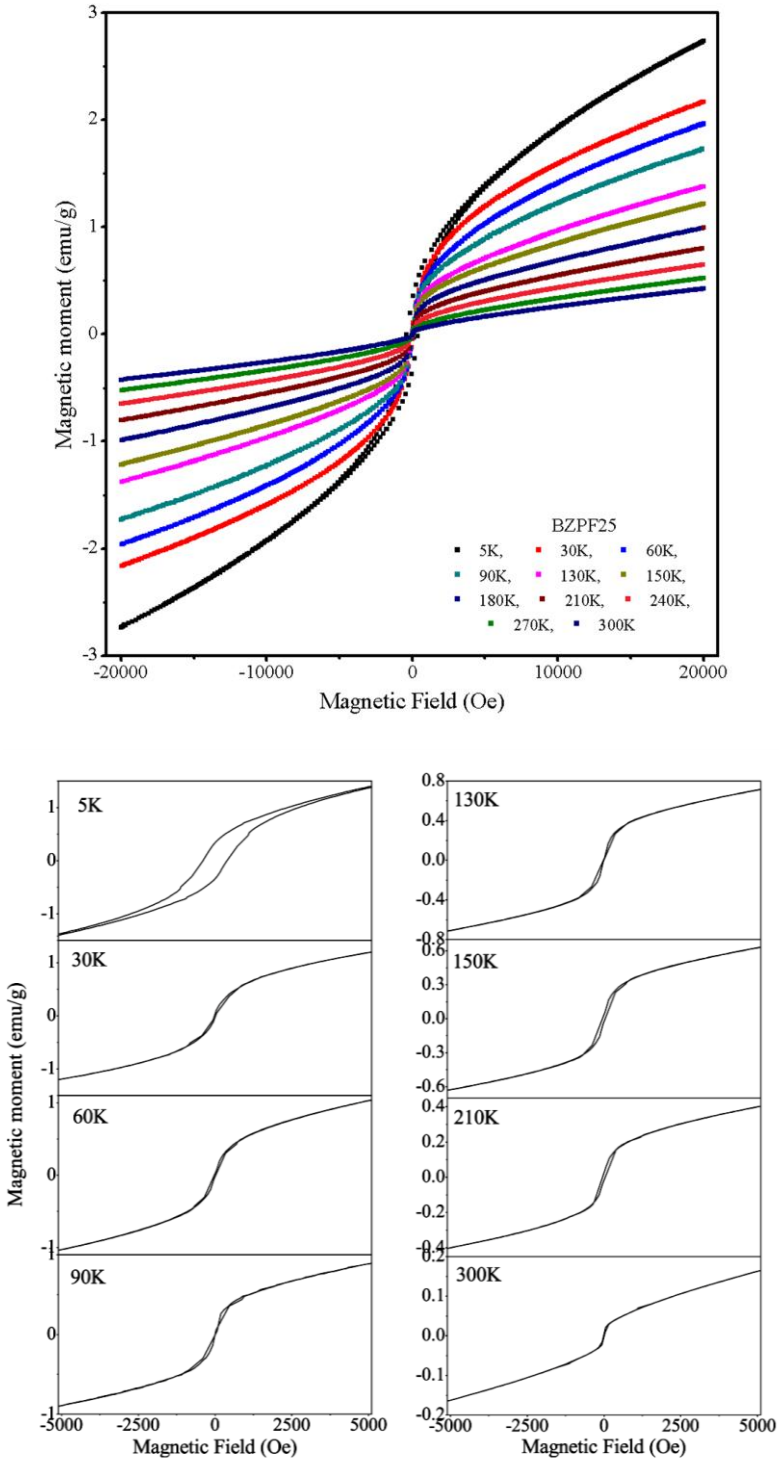

Fig 5.6.B.6 M vs. H for BZPF25 (x = 25 mol% Fe_2O_3) glass sample at different temperatures

Table 5.6.2 Magnetic parameters for the glass system $(Fe_2O_3)_x(70\ Bi_2O_3\ 20\ ZnO\ 10\ PbO)_{1-x}$ (x =5, 10, 15, 20 and 25 mol%)

SAMPLE	X (mol %)	θ_p (K)	T_P (K)	T_{Bf} (K)	χ at 5K ($x10^{-2}$ emu/ mol/Oe) (±0.01)	χ at 60K ($x10^{-2}$ emu/ mol/Oe) (±0.01)	χ at 300K ($x10^{-3}$ emu/ mol/Oe) (±0.01)	H_c at 5K (Oe) (±2)
BZPF5	0.05	124	30	134	3.5	1.29	2.82	418
BZPF10	0.1	105	25	115	3.4	1.16	2.65	331
BZPF15	0.15	275	37	150	4.84	2.54	5.59	549
BZPF20	0.2	247	41	160	7.73	6.19	10.99	579
BZPF25	0.25	212	85	160	4.29	3.08	6.66	388

In summary, the magnetization studies were done for the glass system (100-x)(70 Bi_2O_3 20 ZnO 10 PbO) - xFe_2O_3 , where x= 5,10,15,20 and 25) using PPMS-VSM in the temperature range 5K-300K. Magnetization vs. temperature measurements were taken for each composition. The data were collected after cooling the sample to 5K both in zero field and in a magnetic field of 100 Oe. The magnetization vs. applied field was also investigated over a field of -2T to 2T at a number of temperatures.

The zero-field-cooled (ZFC) and field-cooled (FC) magnetizations at low magnetic field for these glass samples exhibit the typical temperature-dependent magnetic behaviour associated with superparamagnetic relaxation (cluster glass) phenomenon i.e. ZFC magnetization exhibits a peak or maximum at a lower temperature T_{SG} below the bifurcation temperature T_{BF}. The broad peak due to spin freezing may be attributed to the presence of clusters of varying sizes. The temperature dependence of the reciprocal magnetic susceptibility shows Curie-Weiss type behaviour for all the samples in the high temperature range. A positive intercept on temperature axis for all the samples suggest existence of ferromagnetic clusters in the samples. For all the glass compositions, M-H plots show a definite remnant magnetization at 5K even though the hysteresis is weak. Such effects are not present at 300K, as expected for $T>T_p$ in samples containing superparamagnetic clusters.

References

[1] C. Kittle, *Introduction to Solid State Physics, 7th Ed., Wiley, New York*, **Chap. 14 & 15** (1996).

[2] I. Ardelean and S. Filip *J Optoelectronics and Advd Matrls* **5** 157-169 (2003).

[3] I. Ardelean and R. Ciceo Lucacel *Phys Chem Glasses* **46**: 491-493 (2005).

[4] G. D. Khattak, A. Mekki and L. E. Wenger *J of Non-Cryst Solids* **337**:174-181(2004).

[5] P. Sandhya Rani and R. Singh *J. Mater. Sci*. **45** 2868 (2010).

[6] Y. Dimitriev, V. Dimitriev and M. Arunaudov *J Mater Science* **18**:1353 (1983).

[7] F. Criocas, S. K. Mendiratta, I. Ardelean and M. A. Valente Eur Phys J B 20:235-240 (2001).

[8] C.M. Hurd, *Contemp. Phys*. **23** 469 (1982).

[9] I. Ardelean, M. Peteanu, S.Filip, V. Simon and G.Gyorffy, *Solid State Communications,* **102**, 341-346 (1997).

[10] S. Simon, R. Pop, V.Simon and M.Coldea, *J. Non-Crys. Solids* **331,** 1-10 (2003)

[11] I. Ardelean and Monica Toderas, *Modern Physics Letters*, **16**, 485-490 (2002)

[12] I. Ardelean, Hong –Hua Qiu and H. Sakata, *Materials Letters* **32**, 335-338 (1997).

[13] I. Ardelean, G. Salvan, M. Peteanu, V. Simon, C. Himcinschi and F. Ciorcas, *Mod. Phys. Lett. B,* **13** 801-808 (1999).

[14] Joanna L. Shaw, Ardian C Wright, Roger N. Sinclair, G. Kanishka Marasinghe, Diane Holland, Martin R. Lees and Charlie R. Scales, *J. Non-Crys. Solids* **345 & 346**, 245 (2004).

[15] P. Sandhya Rani and R. Singh *J Phys & Chem Solids* **74** 338-343 (2013) .

[16] P. Sandhya Rani and R. Singh, *AIP Conf. Proc*. **1447** 553 (2012).

[17] P.P. Vaishnava, U. Senaratne, E.C. Bue, R. Naik, V.M. Naik, G.M. Tsoi and L.E. Wenger, *Physical Review B*, **76**, 024413 (2007).

Summary and Conclusions

The present work was carried out with the objective of understanding a correlation between the structure and the properties of some tellurite and bismuthate glasses containing transition metal oxide. The systematic Infrared (IR), Differential Scanning Calorimetry (DSC), Electron Spin Resonance (ESR) and magnetization measurements on some tellurium rich and bismuth rich oxide glass systems containing CuO and Fe_2O_3 transition metal (TM) oxides. The parallel DSC, IR, ESR and magnetization measurements have helped in correlating the short range magnetic interactions and the structure of the glass matrix. Oxide glasses containing a large amount of magnetic ions show magnetic transitions like spin glasses or superparamagnets. In the case of multicomponent Bi_2O_3 –ZnO- PbO- Fe_2O_3 glass system, the spin dynamics and ferromagnetic phase formation has been observed.

The structural, thermal and magnetic properties of the glasses are affected by several factors like the nature and concentration of the TM ions, the concentration of TM ion in reduced valence state, the preparation conditions and the microscopic or macroscopic structure of the glass.

The Te rich and Bi rich glass samples of various compositions were synthesized by melt-quenching method. The glass systems synthesised and studied include:

1. (100-x)TeO_2 – xCuO, where x = 10, 20, 30, 40 and 50.
2. (20-x) ZnO – 80TeO_2 – xFe_2O_3, where x = 0, 5, 10, 15 and 20.
3. 20ZnO – (80-x) TeO_2 – xFe_2O_3, where x = 0, 1, 3, 5 and 7.
4. 10Fe_2O_3 – (90-x) TeO_2 – x Bi_2O_3, where x = 0, 5, 10, 15 and 20.
5. 20Fe_2O_3 – (80-x)TeO_2 – x Bi_2O_3, where x = 0, 5, 10, 15, 20 and 25.
6. (100-x) (70Bi_2O_3 20ZnO 10 PbO) – xFe_2O_3, where x = 0, 5, 10, 15, 20 and 25

The XRD studies confirmed the amorphous nature of the glass samples. The xrd studies of the multicomponent glass series at s.no.6 indicates the presence of crystalline phase.

The IR studies indicate the presence of TeO_4 tbp and TeO_3 tps in tellurite glasses. The increase in modifier content leads to conversion of TeO_4 tbps into TeO_3 and TeO_2 groups. In the case of (100-x) ($70Bi_2O_3$ 20ZnO 10 PbO) – xFe_2O_3 glass system, the Bi-O bonds are partially replaced by Fe-O bonds with the addition of Fe_2O_3.

The DSC studies have proved glass transition temperature T_g, crystallization onset temperature T_o, crystallization peak temperature T_p and thermal stability ($\Delta T = T_o - T_g$)values for all the glass samples. The activation energy for crystallization E_c , is estimated for some of the samples having well defined crystallization peak. The dimension of crystallization is 3 (three) for the tellurite glass systems. The tellurite glasses have T_g, T_p, ΔT in the range 286-413^oC, 426 -576 ^oC and 84 -171 ^oC respectively. E_c is found to be in the range 251-640kJ/mol. The Fe_2O_3 containing glasses have higher values of thermal parameters. However, addition of Bi_2O_3 has led to the enhancement of the values of these parameters in the case of Fe_2O_3 -TeO2-Bi2O3 glasses. The Bi_2O_3 rich multicomponent glass system has T_g , T_p and ΔT in the range 311-373 ^oC , 379-427 ^oC and 34-75 ^oC respectively.

The electron spin resonance (ESR) studies provide information about short range magnetic interactions in the glasses. With the increase of TMO concentration in copper tellurite and zinc tellurite glass systems, antiferromagnetic interactions increase. In zinc tellurite glass systems doped with iron oxide, the formation of dimmers or triads of Fe^{3+} ions is observed. In the case of iron tellurite glasses doped with Bi_2O_3 , antiferromagnetic interaction increases with increase in Bi_2O_3 . The extensive ESR studies on multi component bismuthate glass system (100-x)(70 Bi_2O_3 20 ZnO 10 PbO) - xFe_2O_3 have revealed the existence of magnetic clusters in these glasses. Low temperature ESR pattern consists of two maxima in absorption spectra characteristic of existence of fine magnetic clusters in these glasses. The experimental results have been explained in view of theoretical model developed for systems containing fine magnetic clusters.

Magnetization studies on tellurite glasses indicate the presence of both ferromagnetic (FM) and antiferromagnetic (AFM) interactions among TM ions. The paramagnetic susceptibility of the glasses increases with the increase in TMO content in copper tellurite and zinc tellurite glasses. The μ_{eff} values obtained for all samples are lower than the magnetic moment of the free ion ($\mu_{Cu}^{2+} = 1.73\mu_B$) indicating the presence

of both Cu^{2+} and Cu^{+} ions in these glasses. In $Fe_2O_3TeO_2Bi_2O_3$ glasses, magnetization decreases with increase in Bi_2O_3 content. The multicomponent bismuthate glasses containing Fe_2O_3 exhibits cluster glass phenomenon. From M-H plots, the estimated coercivity values are found to decrease with increase in temperature. The temperature dependence of the reciprocal magnetic susceptibility shows Curie-Weiss type behaviour for all the samples in the high temperature range. A positive intercept on temperature axis for all the samples suggest existence of ferromagnetic clusters in the samples. The broad peak due to spin freezing may be attributed to the presence of magnetic clusters of varying sizes.

Publications

Journals

1. **Electrical and Magnetic Properties of Copper Tellurite Glasses**, P. Sandhya Rani and R. Singh: *J Mater Sci* **45** 2868-2873 (2010).
2. **Electron Spin Resonance and Magnetization Studies of ZnO-TeO_2- Fe_2O_3 Glasses**, P. Sandhya Rani and R. Singh: *J Phys. & Chem. Solids* **74** 338-343 (2013).
3. **Magnetic Interactions in Iron Tellurite Glasses**, P. Sandhya Rani and R. Singh: *AIP Conf. Proc.* **1447** 553 (2012).
4. **Magnetic Properties of Bi_2O_3-ZnO-PbO-Fe_2O_3 glasses**, P. Sandhya Rani and R. Singh: *Ind J Cryogenics* (accepted).

Under preparation

1. **ESR and Magnetization Studies of Bi_2O_3-ZnO-PbO-Fe_2O_3 glasses** P. Sandhya Rani and R. Singh (to be communicated).
2. **Kinetics of glass transition of copper tellurite glasses** P. Sandhya Rani and R. Singh (to be communicated).
3. **Electron Spin Resonance and Magnetization Studies of Fe_2O_3 glasses** P. Sandhya Rani and R. Singh: (to be communicated).

Conference presentations

1. **Magnetic Clusters in Bi_2O_3 ZnO PbO Fe_2O_3 Glass System** Sandhya Rani P. and R. Singh *Solid State Phys (India)* **54** 493 (2009).
2. **Crystallization Kinetics of Glass System $10Fe_2O_3$-(90-x) TeO_2-xBi_2O_3 Glasses** Sandhya Rani P. and R. Singh *Solid State Phys (India)* **53** 641 (2008).
3. **Crystallization Kinetics of glass system $20Fe_2O_3$-(80-x)TeO_2-xBi_2O_3** Sandhya Rani P. and R. Singh *Solid State Phys (India)* **52** 469 (2007).
4. **Crystallization Kinetics of Copper Tellurite glasses** Sandhya Rani P. and R. Singh *Solid State Phys (India)* **51** 379 (2006).
5. **DSC and ESR studies of Tellurium Vanadate glasses** Sandhya Rani P. and R. Singh *Solid State Phys (India)* **49** 356 (2004).